MAX-PLANCK-INSTITUT
FÜR METEOROLOGIE

Quantifying aspects of the ocean’s energetics using eddy-resolving simulations

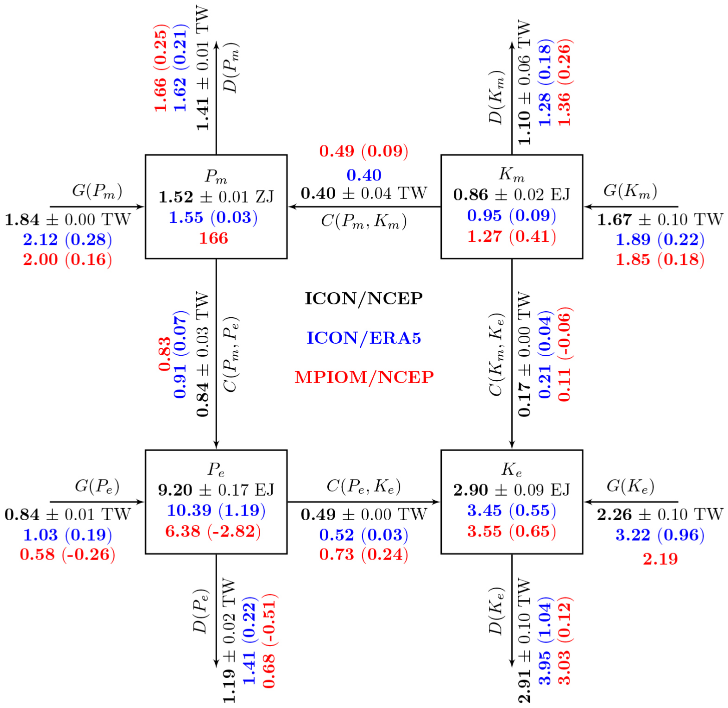

John Bosco Ssebandeke

Hamburg 2024

Berichte zur Erdsystemforschung
Reports on Earth System Science

279
2024

Hinweis

Die Berichte zur Erdsystemforschung werden vom Max-Planck-Institut für Meteorologie in Hamburg in unregelmäßiger Abfolge herausgegeben.

Sie enthalten wissenschaftliche und technische Beiträge, inklusive Dissertationen.

Die "Berichte zur Erdsystemforschung" führen die vorherigen Reihen "Reports" und "Examensarbeiten" weiter.

Notice

The Reports on Earth System Science are published by the Max Planck Institute for Meteorology in Hamburg. They appear in irregular intervals.

They contain scientific and technical contributions, including PhD theses.

The "Reports on Earth System Science" continue the former "Reports" and "Examensarbeiten" of the Max Planck Institute.

Anschrift / Address

Max-Planck-Institut für Meteorologie
Bundesstrasse 53
20146 Hamburg
Deutschland

Tel./Phone: +49 (0)40 4 11 73 - 0
Fax: +49 (0)40 4 11 73 - 298

name.surname@mpimet.mpg.de
www.mpimet.mpg.de

Layout

Bettina Diallo and Norbert P. Noreiks
Communication

Copyright

Photos below: ©MPI-M
Photos on the back from left to right:
Christian Klepp, Jochem Marotzke,
Christian Klepp, Clotilde Dubois,
Christian Klepp, Katsumasa Tanaka

Quantifying aspects of the ocean's energetics using eddy-resolving simulations

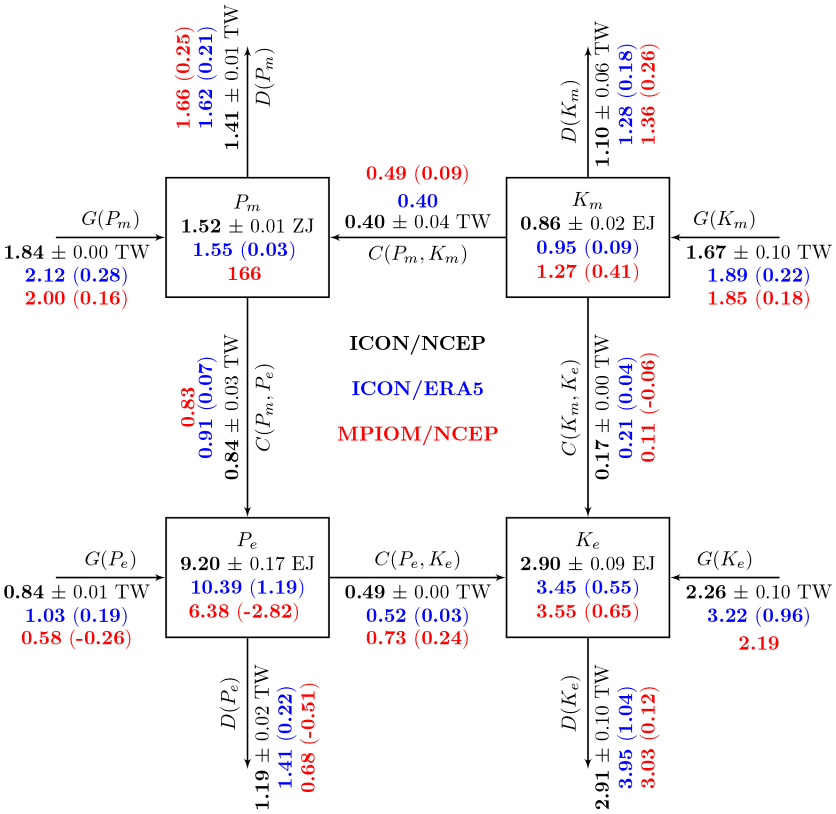

John Bosco Ssebandeke

Hamburg 2024

John Bosco Ssebandeke
aus Kampala, Uganda

Max-Planck-Institut für Meteorologie
The International Max Planck Research School on Earth System Modelling
(IMPRS-ESM)
Bundesstrasse 53
20146 Hamburg

Tag der Disputation: 8. Mai 2024

Folgende Gutachter empfehlen die Annahme der Dissertation:
Prof. Dr. Jin-Song von Storch
Dr. Nils Brüggemann

Vorsitzender des Promotionsausschusses:
Prof. Dr. Hermann Held

Dekan der MIN-Fakultät:
Prof. Dr.-Ing. Norbert Ritter

Berichte zur Erdsystemforschung / Max-Planck-Institut für Meteorologie 279/2024
Reports on Earth System Science / Max Planck Institute for Meteorology

ISSN 1614-1199 - doi: 10.17617/2.3588883

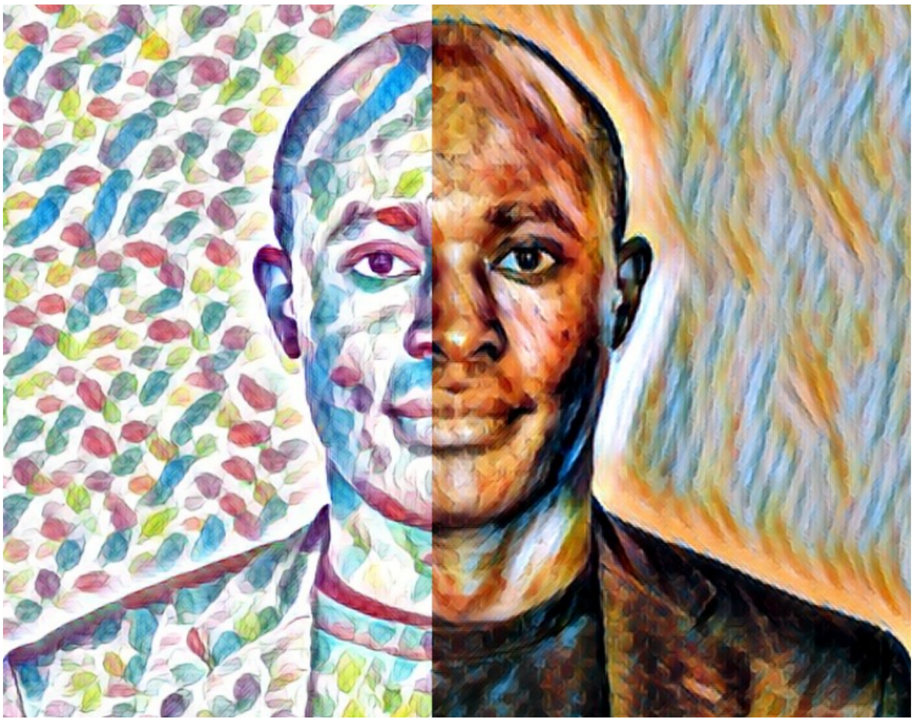

To the younger me, who dared to dream

ACKNOWLEDGMENTS

I am profoundly grateful to the IMPRS-ESM school for providing funding for my doctoral research. Special thanks to IMPRS-ESM Office — Antje Weitz, Michaela Born, and Cornelia Kampmann for their support especially during the period leading up to the start of my PhD — COVID-19 was at its peak then. I am greatly thankful to my supervisors, Jin-Song von Storch and Nils Brüggemann, for their unwavering guidance, patience and support throughout this exciting research endeavour. I am also thankful to Haak Helmuth for helping me set up ICON-O numerical simulations. Thanks to all the current and former members of the Climate Energetics research group for weekly insights and scintillating discussions. I am grateful to my family, friends, colleagues and fellow doctoral students, especially Morfa Avalos Yanmichel, Clarissa Kroll, Lara Wallberg and Luca Schmidt. I am indebted to members of the Earth System department at the ICTP — Fred Kucharski and Riccardo Farneti — and the Physics department at Makerere University — Florence M. D'ujanga and Daniel Mukiibi. Lastly, I am also indebted to the Max Planck Institute for Meteorology and DKRZ for providing the infrastructure and a conducive environment to conduct my science.

ABSTRACT

The atmosphere at the air-sea interface, supplies matter, energy and momentum to the ocean, thereby forcing the ocean. The atmospheric forcing and the resulting oceanic circulation are at large scales. Through nonlinear processes, the energy contained in the large-scale oceanic circulation is redistributed among various scales, and regions and converted from one energy form to another. The oceanic Lorenz Energy Cycle quantifies the energy pathways of energy conversion from atmospheric forcing to mean total energy, and further to eddy available potential energy, eventually to eddy kinetic energy. However, the energy cycle depicts only gross features and does not give detailed information regarding the modality of energy conversion due to the nonlocal nature of the energy conversion — nonlocality is not captured by the global Lorenz Energy Cycle. Another important aspect concerns the energy conversion between mean and eddy kinetic energy. In the atmosphere, the conversion is from eddy kinetic energy to mean kinetic energy and this is thought to represent an upscale transfer of energy. However, in the ocean, the transfer is reversed; mean kinetic energy is converted into eddy kinetic energy. Lastly, there exists only one estimate of the global oceanic Lorenz Energy Cycle, therefore, it's not clear whether the basic characteristics of the previously estimated Lorenz Energy Cycle are robust. Therefore, the extent to which the previous estimates can reliably reflect the energy transfer processes related to the Lorenz Energy Cycle in the real ocean is unclear.

In this dissertation, we present a thorough assessment of the above-mentioned aspects of ocean energetics using eddy-resolving simulations generated using the ICON-O model. The model is newly developed at the Max Planck Institute for Meteorology and replaces the firmly established MPI-OM model. To ascertain the robustness of the Lorenz Energy Cycle, we re-examined the Lorenz Energy Cycle for the global ocean by assessing its sensitivity to model and forcing differences. We established that the previous estimate is indeed robust — the Lorenz Energy Cycle is insensitive to both model and forcing differences. The insensitivity of the Lorenz Energy Cycle to forcing differences pictures the ocean as an inefficient 'windmill' that converts only a small portion of the inputted mechanical energy into the interior mean and transient circulations. Furthermore, we show that the exchange of kinetic energy is such that the mean flow loses energy in the surface layers, and most of the energy released by the mean flow is used for eddy growth, while the rest is transferred to the deeper ocean and then, together with the energy released by the eddies, it's transferred back to the mean flow. Lastly, a note is made about the sensitivity of the gross features of the eddy-mean flow interaction to topographic forcing. In contrast to what is observed in idealistic, 2 layer models, we observed that the general features of energy interaction remain unchanged in complex OGCMs.

ZUSAMMENFASSUNG

Die Atmosphäre an der Grenzfläche zwischen Luft und Meer führt dem Ozean Materie, Energie und Impuls zu, wodurch der Ozean angetrieben wird. Der atmosphärische Antrieb und die sich daraus ergebende ozeanische Zirkulation finden auf großen Skalen statt. Durch nichtlineare Prozesse wird die in der großräumigen Ozeanzirkulation enthaltene Energie Durch nichtlineare Prozesse wird die in der großräumigen Ozeanzirkulation enthaltene Energie zwischen verschiedenen Skalen und Regionen umverteilt und von einer Energieform in eine andere umgewandelt. Der ozeanische Lorenz-Energiezyklus quantifiziert die Wege der Energieumwandlung vom atmosphärischen Antrieb zur mittleren Gesamtenergie und weiter zur verfügbaren potenziellen Energie der Wirbel und schließlich zur kinetischen Energie der Wirbel. Der Energiezyklus stellt jedoch nur grobe Merkmale dar und liefert keine detaillierten Informationen über die Modalität der Energieumwandlung, da die Energieumwandlung nicht lokal erfolgt — die Nichtlokalität wird vom globalen Lorenz-Energiezyklus nicht erfasst. Ein weiterer wichtiger Aspekt betrifft die Energieumwandlung zwischen mittlerer und wirbelkinetischer Energie. In der Atmosphäre erfolgt die Umwandlung von der kinetischen Energie der Wirbel in die mittlere kinetische Energie, und man geht davon aus, dass es sich dabei um eine aufwärtsgerichtete Energieübertragung handelt. Im Ozean jedoch wird die mittlere kinetische Energie in wirbelkinetische Energie umgewandelt. Schließlich gibt es nur eine Schätzung des globalen ozeanischen Lorenz-Energiekreislaufs, so dass nicht klar ist, ob die grundlegenden Merkmale des zuvor geschätzten Lorenz-Energiekreislaufs stabil sind. Daher ist es fraglich, inwieweit die bisherigen Schätzungen den Energiekreislauf zuverlässig widerspiegeln können.

In dieser Dissertation präsentieren wir eine gründliche Bewertung der oben genannten Aspekte der Ozeanenergien anhand von wirbelauflösenden Simulationen, die mit dem ICON-O-Modell erstellt wurden. Das Modell wurde am Max-Planck-Institut für Meteorologie neu entwickelt und ersetzt das fest etablierte etablierte Modell MPI-OM. Um die Robustheit des Lorenz-Energie-Zyklus zu ermitteln, haben wir den Lorenz-Energie-Zyklus für den globalen Ozean erneut untersucht, indem wir seine Empfindlichkeit gegenüber Modell- und Antriebsunterschieden bewertet haben. Wir haben festgestellt, dass die frühere Schätzung in der Tat robust ist - der Lorenz-Energiezyklus ist unempfindlich gegenüber Modell- und Antriebsunterschieden. Die Unempfindlichkeit des Lorenz-Energiekreislaufs gegenüber Antriebsunterschieden stellt den Ozean als eine ineffiziente "Windmühle"dar, die nur einen kleinen Teil der zugeführten mechanischen Energie in die mittleren und instationären Zirkulationen im Inneren umwandelt. Darüber hinaus zeigen wir, dass der Austausch von kinetischer Energie so erfolgt, dass die mittlere Strömung in den Oberflächenschichten Energie verliert und der größte Teil der von der mittleren Strömung freigesetzten Energie für das Wirbelwachstum verwendet wird, während der Rest in den tieferen Ozean übertragen wird und dann zusammen mit der von den Wirbeln freigesetzten Energie wieder zurückgeführt wird. Wirbeln freigesetzte Energie wieder in die mittlere Strömung zurückfließt. Abschließend wird auf die Empfindlichkeit der groben Merkmale der Wechselwirkung zwischen Wirbel und mittlerer Strömung gegenüber topografischen Einflüssen hingewiesen. Im Gegensatz zu idealistischen, zweischichtigen Modellen haben wir festgestellt, dass die allgemeinen Merkmale der Energieinteraktion in komplexen OGCMs unverändert bleiben.

CONTENTS

ACRONYMS

LEC	Lorenz Energy Cycle
SRTM	Shuttle Radar Topography Mission
ECMWF	European Centre for Medium-Range Weather Forecasts
ERA5	Fifth-generation ECMWF Atmospheric Reanalysis
NCEP/NCAR	National Centers for Environmental Prediction and the National Center for Atmospheric Research

LIST OF PUBLICATIONS

Ssebandeke, J., von Storch, J. S., & Brüggemann, N. (2023). Sensitivity of the Lorenz energy cycle of the global ocean. Ocean Dynamics, 1-16.

Ssebandeke, J., von Storch, J. S., & Brüggemann, N. (2024). On the exchange of kinetic energy between the mean flow and the eddies. (In preparation)

1 INTRODUCTION

> *Everything is energy and that's all there is to it. Match the frequency of the reality you want and you cannot help but get that reality. It can be no other way. This is not philosophy. This is physics*
>
> — Albert Einstein

1.1 ENERGETICS OF A TURBULENT CLIMATE SYSTEM

The ocean and the atmosphere are fundamental components of the climate system and form a complex coupled system through the exchange of matter, momentum and energy. Understanding how the ocean and the atmosphere function is of primary importance, among other reasons, in predicting climate change and establishing strategies to mitigate its effects. Since the earliest theories of circulation (Sandström, 1908), energetics have been at the core of circulation studies. The earliest energetics work was based on cyclones (Margules, 1905) and then was extended to the large-scale circulation of the atmosphere (Peixóto and Oort, 1984; Van Mieghem, 1973; Manabe, 1971; Lorenz, 1955; Wiin-Nielsen and Chen, 1993), and afterwards to the oceanic large-scale circulation (Peixóto and Oort, 1984; Oort et al., 1994). Work-related to the oceanic large-scale circulation was delayed partly because much of the work in the early stages was based on theory and observations, however, observations in the oceanic subsurface are meagre. Furthermore, the frequency of observations is limited in both space and time, and this limits the extent of what could be learned from observations like the role of eddies cannot be assessed without sufficient temporal and spatial resolution.

The advent of high-resolution numerical simulations and new methodical additions to previous theories and observations has broadened the spectrum of what scientists can study regarding the energetics of the climate system. While work in the atmosphere has tremendously increased following advancements in numerical simulations (Li et al., 2007; Kim and Kim, 2013b; Marques et al., 2009), the progress in understanding ocean energetics was hampered because of the small-scale nature of the many essential features and processes in the ocean general circulation — the Rossby radius in the atmosphere is about $\mathcal{O}(1000\,\mathrm{km})$ compared to $\mathcal{O}(100\,\mathrm{km})$ in the ocean. Nevertheless, ocean energetics are subject to increasing evaluations — von Storch et al., 2012 comprehensively evaluated the energetics of oceanic global circulation using model simulations. Different from previous evaluations based on observations (Oort et al., 1994), von Storch et al., 2012 assessed the role of eddies in global circulations.

Eddies play a significant role in large-scale circulation — about 75% of the total kinetic energy of the ocean resides in the eddy field (von Storch et al., 2012). Figure 1.1 shows a snapshot of the total kinetic energy in the ocean derived from a coupled ICON model simulation. Small-scale, eddy structures can prominently be observed, especially in the southern ocean, equatorial region and along the western boundary currents. In the atmosphere, kinetic energy is nearly evenly split between the mean circulation and the eddies, however, the kinetic energy of the mean circulation is mostly derived from that of the eddy field (see red bold arrow in figure 1.2). Furthermore, eddies play a crucial role in the redistribution of energy (Matsuta and Masumoto, 2023), heat transport (Jayne and Marotzke, 2002) and energy conversion (von Storch et al., 2012; Aiki et al., 2016; Holland, 1978).

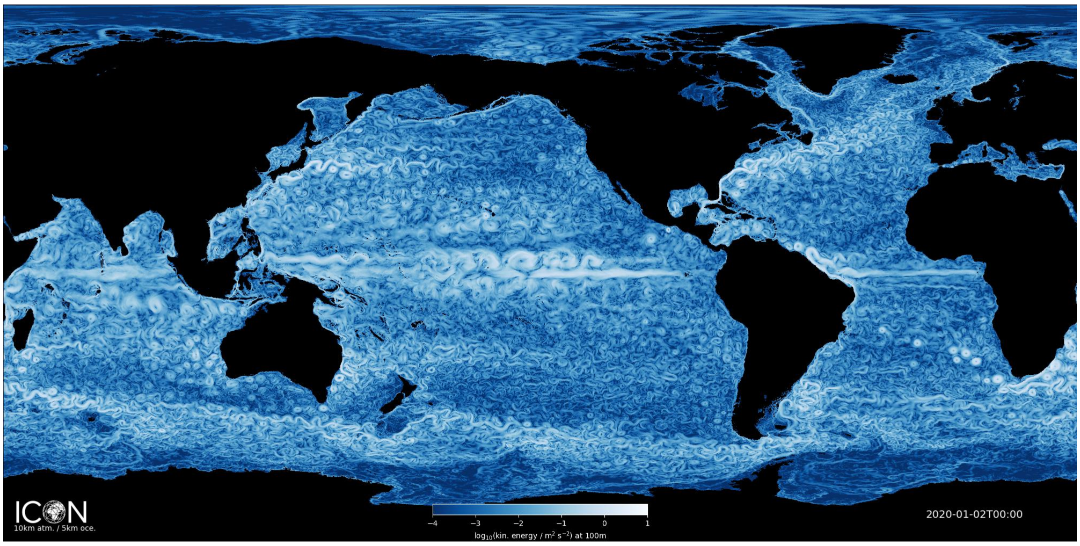

Figure 1.1: Snapshot (2020-01-02T00:00) of total kinetic energy derived from the coupled ICON model at 100 m. The resolution of the atmosphere is 10 km and 5 km for the ocean. Units: m^2/s^2 (courtesy of nextGEMS project, cycle 4).

Energetics of the large-scale circulation are mostly studied using energy cycles — an energy cycle is a quantitative framework for understanding how energy proceeds, through transformation, from generation to dissipation. There are a number of flavours of the energy cycle: the classical Lorenz Energy Cycle (LEC) framework (Lorenz, 1955), the Bleck framework (Bleck, 1985) and the energy cycle in spectral space (Augier and Lindborg, 2013). The key difference between them is in the coordinates used – The Bleck framework uses the isentropic and isopycnic coordinate system and has been used in Aiki et al., 2016; Loose et al., 2023, the Lorenz Energy Cycle uses the z-coordinates and has been studied in von Storch et al., 2012; Li et al., 2007; Kim and Kim, 2013b; Wu et al., 2017, while the latter is in spectral space and has been used in Augier and Lindborg, 2013; Read et al., 2018. The main advantage of the Lorenz Energy Cycle is that it is defined in the same coordinates in which data is stored and therefore easier to evaluate.

1.1.1 The Lorenz Energy Cycle

1.1.1.1 *Energy Forms and Compartments*

Here, energy is broadly classified into kinetic and available potential energy. Available potential energy is the portion of the total potential energy that can be converted into kinetic energy and comprises internal energy, gravitational potential energy and latent energy. For a more elaborate explanation of the components of available potential energy, see von Storch, 2019 and references therein. In this work, we follow the definition of available potential originally suggested by Lorenz, 1955 — it is calculated as the difference between the value of the total potential energy and the potential energy in the reference state. The reference state is defined as the area mean of total potential energy at every level. This definition has also been used in Oort et al., 1994; von Storch et al., 2012; Wu et al., 2017.

The general circulation comprises the time-mean large-scale mean circulation and the transients, which is dominated by mesoscale eddies in the ocean and synoptic variations in the atmosphere. Here, we use the Reynolds decomposition to decompose the time-mean circulation and the transients. For example, for a quantity x, the decomposition would be

$$x = \overline{x} \ + \ x'$$

where $\overline{x}$ is the steady time-mean (spatial average) component and x' denotes the deviations from the steady time-mean component. The deviation is calculated such that its time average equals zero ($\overline{x'} = 0$). Hereafter, the overbar represents the time mean component and the prime represents the eddy component. The eddy component is dominated by mesoscale eddies, however, there are other contributions like the seasonal cycle and inter-annual variability. Other considerations for defining eddies have also previously been used in defining eddies, like scale decomposition (Jamet et al., 2022; Buzzicotti et al., 2022).

The energy forms mentioned above can further be classified into the energy possessed by eddies and the energy contained in the mean circulation—this results in 4 compartments: available potential energy of the mean circulation, P_m and that of the eddy field, P_e, and the kinetic energy of the mean circulation, K_m and that of the eddy field, K_e. The definition of the energy compartments is given below.

$$P_m = -\int_V \frac{g}{(2n_\circ)} \overline{\rho^*}^2 \, \mathrm{d}V$$

$$P_e = -\int_V \frac{g}{(2n_\circ)} \overline{\rho'^2} \, \mathrm{d}V$$

$$K_m = \int_V \frac{\rho_\circ}{2} \left(\overline{u}^2 + \overline{v}^2 \right) \mathrm{d}V$$

$$K_e = \int_V \frac{\rho_\circ}{2} \left(\overline{u'^2} + \overline{v'^2} \right) \mathrm{d}V$$

where $\int_V \mathrm{d}V$ indicates the integral over the volume of the ocean or the atmosphere, u and v is the zonal and the meridional current speed, ρ is the density, $\rho_\circ$ is the reference density, ρ^* is the density minus the reference density defined as the area mean of density at every level. $n_\circ = \frac{\partial \langle \overline{\varrho} \rangle}{\partial z}$, ϱ is the potential density. Capital letters represent global energies obtained by integrating the respective specific energy over the entire volume of the ocean or atmosphere. Lowercase letters represent specific energy defined as energy per unit volume.

1.1.1.2 *Interaction processes and the concept of energy conversion*

The four energy compartments interact. In a special case when the energy interaction is represented by the same term but with opposite signs in two energy equations, then the interaction represents energy conversion between the two compartments. For example given an interaction term C and 2 energy forms A and B, with energy equations given by

$$\frac{\partial A}{\partial t} + \ldots = C, \qquad \frac{\partial B}{\partial t} + \ldots = -C$$

The interaction term C appears in the equation of A and B but with opposite signs and hence acts as a conversion term. Energy conversion plays a central role in global circulation and is mostly facilitated by eddies. In the real ocean, energy conversion is through physical processes like an inverse cascade, barotropic and baroclinic instability.

For a conversion term $C(X,Y)$, the convention used here is such that $C(X,Y) = -C(Y,X)$ and the direction of $C(X,Y)$ goes from X to Y. Hereafter we use capital letters to indicate globally integrated conversion terms, and lower-case letters to indicate local conversion terms. The conversion terms between the different compartments are listed below

$$\begin{aligned}
C(P_m,P_e) &= -\int_V \frac{g}{n_\circ} \overline{\mathbf{u'_H}\,\rho'} \cdot \nabla_{\mathbf{H}} \overline{\rho^*} \;\mathrm{d}V \\
C(K_e,K_m) &= \int_V \rho_\circ \left(\overline{\mathbf{u}'v'} \cdot \nabla \overline{v} + \overline{\mathbf{u}'u'} \cdot \nabla \overline{u} \right) \;\mathrm{d}V \\
C(P_m,K_m) &= -\int_V g\overline{\rho^*}\;\overline{w} \;\mathrm{d}V \\
C(P_e,K_e) &= -\int_V g\overline{\rho' w'} \;\mathrm{d}V
\end{aligned}$$

where $\int_V \mathrm{d}V$ indicates the integral over the volume of the ocean or the atmosphere, $\mathbf{u}(u,v,w)$ is the three dimensional velocity, $\mathbf{u_H}(u,v)$ is the two dimensional velocity, w is the vertical velocity and ∇ is the three dimensional gradient operator.

1.1.1.3 *Energy sources and sinks*

The atmosphere is driven by differential heating — the atmosphere is heated from below in the tropics and cooled in the poles at a higher altitude. This leads to a temperature gradient between the equator and the poles and hence mean available potential energy. Through baroclinic instability, mean available potential energy is transformed into eddy available potential energy and further to eddy kinetic energy and eventually to large scale mean kinetic energy (Lorenz, 1967). The large-scale atmospheric mean circulation then primarily drives oceanic mean circulation. The atmospheric forcing and the resulting oceanic circulation are at large scales. Through nonlinear processes, the energy contained in the large-scale oceanic circulation is converted from one energy form to another, redistributed among various scales, and to regions where the energy is dissipated by friction (Ferrari and Wunsch, 2009; Zhai et al., 2010). In the Lorenz Energy Cycle framework, dissipation is calculated as residuals. The generation terms of the different energy compartments are listed below

$$
\begin{aligned}
G(P_m) &= -\int_S \alpha_\circ \frac{g}{n_\circ} \overline{J}\ \overline{\rho^*}\ \mathrm{d}S - \int_S \beta_\circ \frac{g}{n_\circ} \overline{G}\ \overline{\rho^*}\ \mathrm{d}S \\
G(P_e) &= -\int_S \alpha_\circ \frac{g}{n_\circ} \overline{J'\rho'}\ \mathrm{d}S - \int_S \beta_\circ \frac{g}{n_\circ} \overline{G'\rho'}\ \mathrm{d}S \\
G(K_m) &= \int_S \rho_\circ \left(\overline{\tau_x}\ \overline{u} + \overline{\tau_y}\ \overline{v}\right)\ \mathrm{d}S \\
G(K_e) &= \int_S \rho_\circ \left(\overline{\tau_x' u'} + \overline{\tau_y' v'}\right)\ \mathrm{d}S
\end{aligned}
$$

where $\int_S \mathrm{d}S$ indicates the horizontal-surface integral, $\alpha_\circ = \left(\frac{\partial \overline{\rho}}{\partial \theta}\right)_{S,p}$ is the thermal expansion coefficient, and $\beta_\circ = \left(\frac{\partial \overline{\rho}}{\partial S}\right)_{\theta,p}$ is the saline contraction coefficient (temporal variations of the two expansion coefficients are neglected), p is pressure, θ is the potential temperature and S is the salinity. τ_x and τ_y are the zonal and meridional components of the winds stress respectively. $J = (1/\rho_s c)H$ is the temperature flux at the surface, $c = 4000 J(kgK)^{-1}$ is the specific heat of seawater, H the total heat flux at the surface, ρ_s is the density of surface water. $G = \overline{S_1}(E - P)$ is the salinity flux, $\overline{S_1}$ is the time-mean sea surface salinity, E is the evaporation rate and P is the precipitation rate.

1.1.1.4 *Budget equations*

The resulting budget equations contain sources, sinks and transfers of energy. A comprehensive derivation of the budget equations is presented in appendix A. Here we only present the summary of the equations.

$$
\begin{aligned}
\frac{\partial K_m}{\partial t} &= C(K_e, K_m) + C(P_m, K_m) + G(K_m) - D(K_m) = 0 \\
\frac{\partial K_e}{\partial t} &= -C(K_e, K_m) + C(P_e, K_e) + G(K_e) - D(K_e) = 0 \\
\frac{\partial P_m}{\partial t} &= C(P_e, P_m) - C(P_m, K_m) + G(P_m) - D(P_m) = 0 \\
\frac{\partial P_e}{\partial t} &= -C(P_e, P_m) - C(P_e, K_e) + G(P_e) - D(P_e) = 0
\end{aligned}
$$

1.1.2 Comparative energetics of the Ocean and the Atmosphere

Figure 1.3 and 1.2 show the Lorenz Energy Cycle of the ocean and atmosphere respectively. Both figures are adopted from von Storch et al., 2012. The oceanic

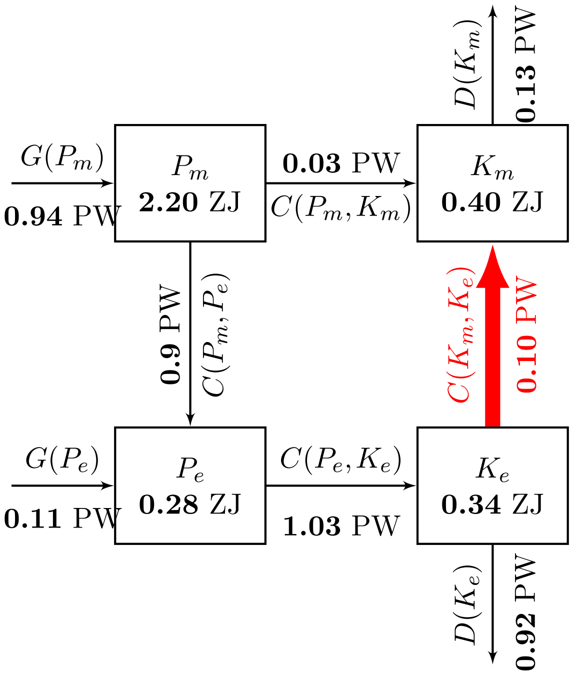

Figure 1.2: Atmospheric LEC adopted from von Storch et al., 2012. Energy reservoirs are in zettajoules (ZJ, 10^{21}), rates of generation, dissipation, and conversion in petawatts (PW, 10^{15}).

Lorenz energy cycle was derived from global 10 km numerical simulations while the energy cycle for the atmosphere is derived from reanalysis datasets (Li et al., 2007). However, estimates of the LEC of the atmosphere based on numerical models show characteristics similar to those observed while using reanalysis datasets (Boer and Lambert, 2008).

The main similarity between the two energy cycles is the dominance of the baroclinic pathway, $P_m \rightarrow P_e \rightarrow K_e$. In the atmosphere this pathway is powered by differential heating — the atmosphere is heated from below in the tropics and cooled from above in the poles. This creates available potential energy which is converted to eddy available potential energy and further to eddy kinetic energy. In the ocean, however, this pathway is powered by wind forcing. Wind drives divergent and convergent motions which generate non-uniform vertical motions in the ocean, which are responsible for transforming mean kinetic energy into mean available potential energy, and lead to the formation of ‘hills’ and ‘troughs’ at the ocean surface over scales of several hundred kilometres. The non-uniform vertical motions also lead to the inclination of density surfaces and horizontal variations in density. Horizontal gradients in density lead to a geostrophic current with vertical shear. If the shear is strong enough, the current becomes baroclinically unstable which transfers the mean available potential energy into eddy available potential and finally to eddy kinetic energy.

The oceanic and atmospheric energy cycles differ in three main aspects: (1) magnitude of the terms: the energy cycle of the atmosphere is more energetic than that of the ocean – the energy pathways of the atmosphere are about three orders of magnitude

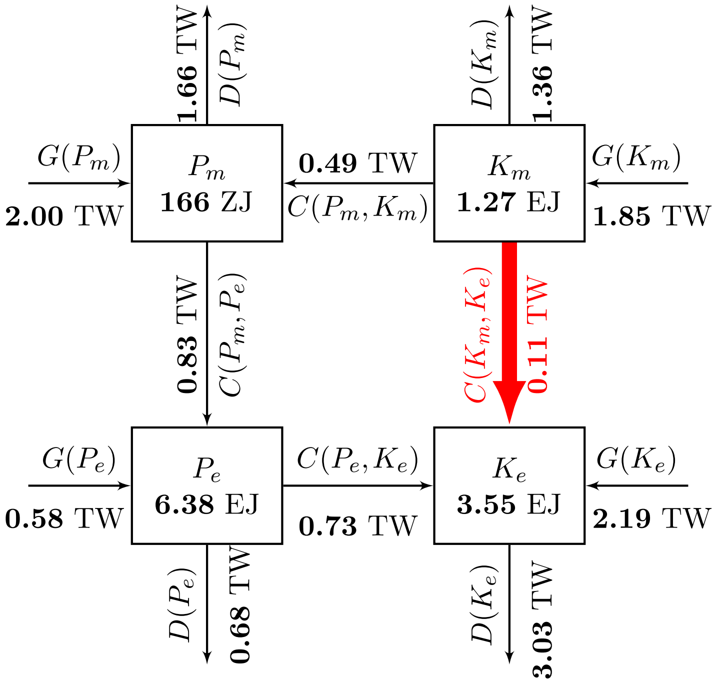

Figure 1.3: Oceanic LEC adopted from von Storch et al., 2012. Energy reservoirs are in zettajoules (ZJ, 10^{21}) and exajoules (EJ, 10^{18}), rates of generation, dissipation, and conversion in terawatts (TW, 10^{12}).

larger than those of the ocean [1]. (2) the way they are forced: While the atmosphere is driven by latitude-dependent heating, the ocean is primarily driven by surface momentum forcing at large scales but also the thermohaline circulation in the ocean is driven by mechanical mixing and buoyancy differences, and lastly (3) the direction of the energy pathways: in the ocean, mean kinetic energy is converted into mean available potential energy through upwelling. In the atmosphere, however, this transfer is small, 0.03 PW and is directed from the mean available potential energy to the mean kinetic energy. It is this transfer that portrays the ocean as a windmill in contrast to the atmosphere which operates as a heat engine (von Storch et al., 2012). Lastly, in the atmosphere, eddy kinetic energy is converted into mean kinetic energy $K_e \rightarrow K_m$ (red bold arrow in figure 1.3 and 1.2) and this is thought to represent an inverse kinetic energy cascade. However, in the ocean, this transfer is directed from the mean kinetic energy to the eddy kinetic energy which could imply that the inverse kinetic energy cascade is weaker or that there are other overlying processes like barotropic instability which transfer energy from the mean flow to the eddies.

---

[1] The mean available potential energy in the ocean appears to be larger than that of the atmosphere, however, the value shown in the oceanic Lorenz Energy Cycle could be erroneous. This is further discussed in chapter 2

1.2 RESEARCH QUESTIONS

1. **How robust are the characteristics of the oceanic Lorenz Energy Cycle presented in von Storch et al., 2012?**

   While the atmospheric energy cycle has been overly evaluated by the use of reanalysis, models and observations, To date, there exists only one estimate of the global oceanic Lorenz energy cycle (von Storch et al., 2012), therefore, it's not clear whether the basic characteristics of the previously estimated LEC are robust. Therefore, the extent to which the previous estimates can reliably reflect the energy transfer processes related to the LEC in the real ocean is unclear.

2. **How is kinetic energy exchanged between the mean oceanic circulation and the eddies?**

   The Lorenz energy cycle depicts only gross features and does not give detailed information — one aspect that is not captured by the global energy cycle is the modality of the kinetic energy exchange. The modality of the energy exchange is not well characterised due to its nonlocal nature (Chen et al., 2014). For global integrals, nonlocality is suppressed and therefore not represented in the global energy cycle. Quantifying the nonlocality of the eddy-mean flow interaction is not only crucial in understanding how oceanic energy, which is inputted at the surface, is transferred to the interior but also relevant in improving parameterisation (Ivey and Imberger, 1991; Eden and Greatbatch, 2008; Marshall and Adcroft, 2010).

3. **Why is the direction of kinetic energy exchange following eddy-mean flow interaction in the ocean opposite to that in the atmosphere?**

   In the atmosphere, kinetic energy conversion, $C(K_m, K_e)$ is directed from the eddies towards the mean flow (see red bold arrow in figure 1.2) and this is thought to represent an upscale transfer of energy. However, in the ocean, the transfer is reversed; mean kinetic energy is converted into eddy kinetic energy (see red bold arrow in figure 1.3). It's unclear why energy conversion in the ocean is opposite to that in the atmosphere. Witter and Chelton, 1998, based on idealistic simulations, pointed out that this reversal in energy conversion is related to bottom-topography in the ocean (see figure 8 in Witter and Chelton, 1998). It's not clear whether the sensitivities of the energy conversion to bottom topography observed in previous idealistic models would also arise in more complex high-resolution OGCMs. Unlike idealised models, OGCMs have non-zonal mean flows, planetary β-effect, ageostrophic dynamics, many vertical layers (not only 2) and so on. Any one of these factors could alter the sensitivity of the eddy-mean flow interaction.

1.3 NUMERICAL MODEL AND SIMULATIONS

1.3.1 ICON-O model

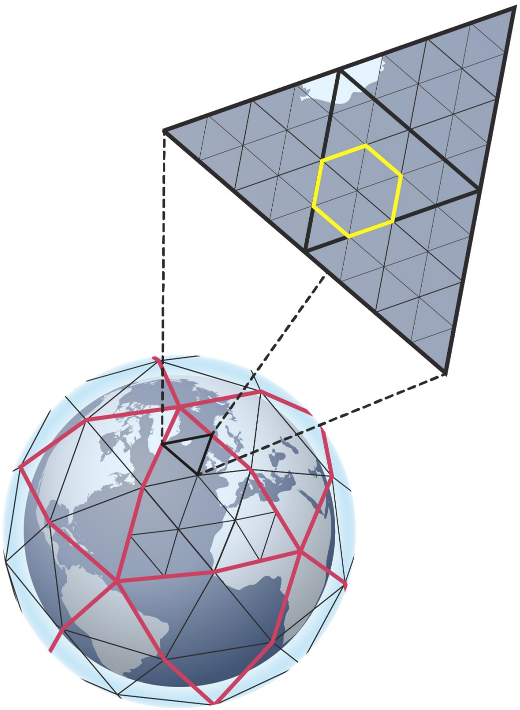

Figure 1.4: ICON-O horizontal model grid. The small triangles shows the primal grid and the yellow hexagon shows the dual grid.

To answer the research questions, we use data derived from the ICON-O model. The model has an unstructured horizontal grid, which is formed from an icosahedron. An icosahedron is a platonic solid with 20 equilateral triangles (faces), 30 edges and 12 vertices (for details on the icosahedron, see Staniforth and Thuburn, 2012). To form the horizontal grid, the icosahedron is circumscribed by a sphere such that, all its vertices are located on the surface of the sphere. Then, the poles are chosen to be located at two opposite vertices. Lastly, the sphere circumscribing the icosahedron is successively triangulated using great circle arcs. In the first triangulation step, term as Rn, each of the great circle arcs joining the 12 vertices is divided into n equal arcs. The new points form new vertices and are connected using great circle arcs forming n^2 equilateral triangles per every original triangle. Using $n = 2$, the resultant triangles are recursively triangulated (using great circle arcs) k times in a step termed as Bk. This results in an unstructured $RnBk$ grid with a total number of cells $n_c(= 20^n24^k)$. When the circumcenters of the different triangles of the primal grid are connected, (around a vertex) the dual grid is formed (figure 1.4). The dual grid comprises hexagons and pentagons. The latter is achieved if the vertex is one from the original icosahedron. In the vertical, the z-coordinate is used. The three-dimensional cells are referred to as prisms.

Here, the definition of the nominal horizontal grid resolution, is similar to the one used in (Zängl et al., 2015; Korn et al., 2022), for an $RnBk$ configuration, the nominal resolution, $\overline{\Delta x}$ is given as the average of the primal cell area which is approximately $\sqrt{\frac{\pi}{5}}\frac{r_e}{n2^k}$. where r_e is the Earth's radius. In this thesis, we use the $R2B8$ configuration. The configuration has these 3729001 cells and according to the approximation above, the horizontal resolution is about 10 km. In the vertical, it has 128 unevenly spaced levels from 5.5 m to 6262 m below the surface. The thickness of each layer is constant other than the uppermost layer where the surface elevation is taken into account. The layer thickness varies from 8.0 to 200.0 m in the deep layers. The topmost layer is 11.0 m thick. ICON-O employs the Arakawa C-type staggering of variables, where the scalar variables are placed at cell circumcenters and the normal components of velocity are located at midpoints of cell edges. The vertical velocity is located at the top and bottom of the triangular prisms, and the rest of the variables are defined on the middle level of the three-dimensional triangular or hexagonal prisms.

ICON-O solves the primitive equations of large-scale ocean dynamics with a free surface. The ocean primitive equations are an evolution equation for a state vector $\{\ v, \eta, \theta, S\}$ that consists of a horizontal velocity field v, the surface elevation η and the tracers: potential temperature θ and salinity S. Time stepping used in ICON-O is the classical semi-implicit Adams-Bashford-2 scheme. In the $R2B8$ configuration used here, the time step is 5 minutes. The fast dynamics of the free surface equation are integrated implicitly by solving a two-dimensional elliptic equation in each time step. This alleviates severe time-step restrictions due to the fast dynamics. The ICON-O model allows for a nonlinear evolution of the free surface, where the thickness of each water column varies in time and where freshwater fluxes are applied directly. After solving the surface-free surface equation, the velocity and tracer variables are moved forward in time following the Adams-Bashford extrapolation scheme. Turbulent vertical mixing in ICON is parameterised following the closure suggested in Gaspar et al., 1990a; Blanke and Delecluse, 1993; Eden et al., 2014. Tracer advection in ICON-O uses a flux-corrected transport algorithm consisting of an upwind scheme as the low-order transport component and a higher-order transport scheme that relies in the horizontal direction on Hilbert space compatible reconstructions and vertically on a piecewise-parabolic reconstruction. A reader interested in a comprehensive description of the dynamics of ICON-O, including the sea ice dynamics, is referred to Korn, 2017; Korn et al., 2022; Jungclaus et al., 2022.

ICON-O is the new model at the Max Planck Institute for Meteorology. Traditionally, the advent of a new model necessitates a model evaluation — ICON-O has been assessed and the prowess documented in Korn, 2017; Korn et al., 2022. However, the previous assessments did not cover the energetic perspective. Figure 1.5 shows the horizontally (globally) averaged profiles of kinetic energy derived from ICON-O simulations – such estimates of the ocean energetics have not been conducted before. ICON-O replaces the firmly established MPI-OM model (Jungclaus et al., 2013). While ICON-O has an unstructured horizontal grid, MPI-OM has a regular horizontal grid (a thorough comparison of ICON-O and MPI-Om is presented in section 2.3.1). The only existing estimate of the Lorenz Energy Cycle was derived from data based on the MPI-OM model (von Storch et al., 2012).

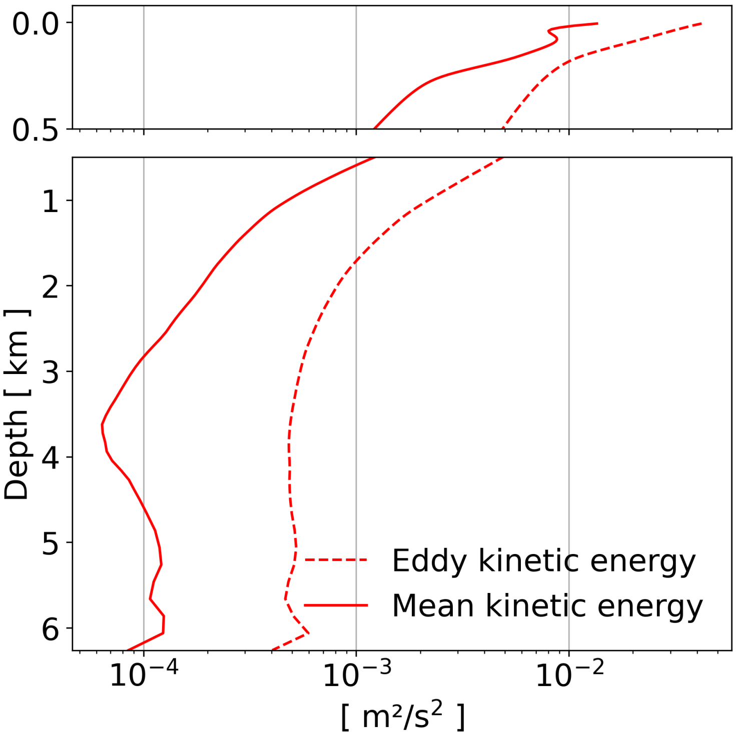

Figure 1.5: Kinetic energy derived from ICON-O forced with ERA5 forcing. Data was averaged over 5 years (2010 - 2014).

1.3.2 Model simulations and Data

Other than the MPIOM/NCEP simulation, the rest of the simulations are generated using the ICON-O model (a summary of the simulations is presented in table 2.1). MPIOM/NCEP simulation was generated in 2012 and some of the fields are no longer available (for details about this simulation, see section 2 in von Storch et al., 2012). The models are forced with surface fluxes derived from two reanalyses —NCEP/NCAR and ERA5. NCEP/NCAR is the longest atmospheric reanalysis dataset and has a resolution of about 200 km and 6 hourly temporal resolution (Kalnay et al., 1996). ERA5 is a more advanced atmospheric reanalysis with a resolution of about 31 km and hourly temporal resolution (Hersbach et al., 2020). In addition to the standard model output, two-variable products xz are generated at every model time step and outputted on a monthly basis to obtain $\overline{xz}$. $\overline{xz}$ represents the mean flux of z in the direction of x. Furthermore, producing xz on a monthly basis is used to infer the eddy flux, $\overline{x'z'}$

$$\overline{x'z'} = \overline{xz} - \overline{x}\ \overline{z}$$

2 SENSITIVITY OF THE LORENZ ENERGY CYCLE OF THE GLOBAL OCEAN

> *Mathematicians seem to have no difficulty in creating new concepts faster than the old ones become well understood*
>
> — Edward Norton Lorenz

This Paper has been published as: Ssebandeke, J., von Storch, J. S., & Brüggemann, N. (2023). Sensitivity of the Lorenz energy cycle of the global ocean. Ocean Dynamics, 1-16.

2.1 ABSTRACT

We re-examine the Lorenz Energy Cycle (LEC) for the global ocean by assessing its sensitivity to model and forcing differences. We do so by comparing LECs derived from two simulations based on different eddy-rich ocean models, ICON-O and MPI-OM, both driven by NCEP/NCAR reanalysis; and by comparing LECs derived from two simulations generated using ICON-O model but driven by two different reanalyses, NCEP/NCAR and ERA5. Regarding model difference, we find weaker eddy kinetic energy, k_e in the ICON-O simulation than in the MPI-OM simulation. We attribute this to the higher horizontal resolution of MPI-OM in the Southern Ocean. The weaker k_e in ICON-O is not caused by the lack of eddy available potential energy, p_e, but by the strong dissipation of p_e and the resulting weak conversion from p_e to k_e. Regarding forcing difference, we find that considerably more mechanical energy is generated by the ERA5 forcing, which has a higher spatial-temporal resolution compared to the NCEP/NCAR forcing. In particular, the generation of k_e, which also contains the resolved part of the internal wave spectrum, is enhanced by about 1 TW (40%). However, the dominance of the baroclinic and the barotropic pathways forces the enhanced generation of k_e to be balanced by an enhanced dissipation in the surface layer. The gross features of LEC are insensitive to both model and forcing differences, picturing the ocean as an inefficient "windmill" that converts only a small portion of the inputted mechanical energy into the interior mean and transient circulations.

2.2 INTRODUCTION

The oceanic and atmospheric general circulation comprises both the time-mean large-scale circulation and the transients, which are dominated by synoptic variations in the atmosphere and mesoscale eddies in the ocean. These components of general circulation exchange energy, and this energy-exchange is well quantified by the Lorenz Energy Cycle (LEC) (Lorenz, 1955 and references therein). The LEC is a quantitative framework for identifying how energy in the ocean and atmosphere proceeds, through transformation, from its generation to its dissipation, and it has become a standard tool for studying the energetics of the general circulation. While a robust picture of the atmospheric LEC has been established, through evaluations based on data of different qualities including those from various reanalyses (Lorenz, 1967; Oort, 1964; Li et al., 2007; Kim and Kim, 2013a; Marques et al., 2009), the picture of the oceanic LEC is much less established. The situation comes about, since the oceanic mesoscale eddies, whose spatial scale is of $O(100 \text{ km})$ and hence one order of magnitude smaller than that of synoptic variations — $O(1000 \text{ km})$— cannot be observed at a high enough frequency with a sufficient spatial coverage, nor truly be captured by the current ocean reanalyses. Capturing these eddies is however important for properly assessing energy transfer between the mean and the transient compartments of circulation. One way to advance is to use simulations in which mesoscale eddies are largely resolved. To our knowledge, there exist one estimate for the LEC of the global ocean (von Storch et al., 2012). It is not clear whether the basic characteristics of the previously estimated LEC are model independent, and therefore, the extent to which the previous estimates can reliably reflect the energy transfer processes related to the LEC in the real ocean is unclear. It is also not clear whether and to what extent the previously identified energy transfer processes change when an ocean model is forced with surface fluxes derived from a more advanced atmospheric reanalysis. This paper addresses these two questions.

We do so by comparing estimates of the ocean LEC obtained from two pairs of simulations. The first pair is performed with the same ocean model forced with surface fluxes derived from two different reanalyses — the NCEP/NCAR (hereafter NCEP) (Kalnay et al., 1996) and the newly released ERA5 reanalysis (hereafter ERA5) (Hersbach et al., 2020). We will refer to differences between this pair of simulations as "forcing differences" (note that other forcing products leading to potentially different LECs are not included within our reference). The second pair consists of simulations performed with two different ocean models — MPI-OM (Marsland et al., 2003; Jungclaus et al., 2013) and ICON-O (Korn, 2017; Korn et al., 2022) — but forced with the surface fluxes derived from the same reanalysis. Differences between this other pair of simulations will be referred to as "model differences" (note again that we only refer to the differences between these two models). The MPI-OM simulation is the one from which the previous estimate by von Storch et al., 2012 is derived and the ICON-O simulation is the same as used for the aforementioned inter-comparison with respect to different forcing products. ICON-O is a newly developed model at the Max Planck Institute for Meteorology (Korn et al., 2022).

The comparison will be based on the balance equations for the mean and the transient kinetic energy, K_m and K_e, and those for the mean and transient available potential energy, P_m and P_e. While the definitions of K_m and K_e are straightforward, those of P_m and P_e rely on approximations. In this paper we follow the definition originally proposed by Lorenz, 1955 and approximate the available potential energy in terms of the deviations of density from a spatially constant reference density ρ_{ref} (Oort et al., 1994). Potential energy associated with these density deviations can be, at least in principle, turned into motions via the related pressure gradients. The resulting LEC, including the definitions of all terms, is introduced in more detail in Appendix A. We note that this definition of available potential energy, together with its associated energy transfers and budgets, differs from the other considerations e.g. that by Winters et al., 1995. As reviewed by von Storch, 2019, the LEC as defined e.g. by Oort et al., 1994; von Storch et al., 2012 focuses on the energy transfers associated with the mesoscale eddy field while the one defined in Winters et al., 1995 focuses on the effect of mixing related to diabatic processes inside the ocean.

This paper is organized as follows: section 2 describes the models and the surface forcing. Section 3 describes the LEC estimated from the ICON-O simulation forced with the NCEP forcing. Differences arising from using different models and from using different surface forcings will be addressed in Section 4. Discussions and a summary are provided in the final section.

2.3 THE NUMERICAL SIMULATIONS

2.3.1 Numerical models

ICON-O (Korn, 2017; Korn et al., 2022) and MPI-OM (Marsland et al., 2003; Jungclaus et al., 2013) are both primitive equation models; however, they employ completely different model architectures and are coupled to completely different sea ice models. ICON-O was designed to improve parallel computing on high performance computers and has recently become the work horse at Max-Planck Institute for Meteorology. The Gent–McWilliams parameterization (Gent and Mcwilliams, 1990) that describes the effect of mesoscale eddies is switched off in MPI-OM and in all ICON-O configurations considered in this study. Vertical mixing is parameterized using the Richardson-number dependent formulation following Pacanowski and Philander, 1981 in MPI-OM and by the TKE scheme following Gaspar et al., 1990b in ICON-O. These parameterizations are responsible for most of the diapycnal mixing in the upper ocean.

In the vertical, both ICON-O and MPI-OM use the standard z-coordinate framework. In the horizontal, both are considered to have a nominal resolution of about 10 km, which allows resolving the bulk of mesoscale eddies outside the polar regions. However, MPI-OM is formulated on a tripolar grid with rectangular shaped grid cells, whereas ICON-O is formulated on an icosahedral grid with triangular shaped grid-cells. The different structure of the grids results in a different number and a different distribution of grid points. The ICON-O grid has a total of 3,699,276 wet grid points in the surface layer and total 128 vertical levels. The MPIOM grid has a total of 5,558,745 wet grid points in the surface layer and total 80 vertical levels. the larger number of grid points in MPI-OM is due to the fact that the grid size, south of the equator, is refined based on the cosine of the latitude — $0.1^\circ \cos(\phi)$, where ϕ is the latitude. Thus, the MPIOM grid in the Southern hemisphere is much less uniform, ranging from about 10 km near the equator, up to 5-6 km near 60°S, and up to about 2-3 km in the Weddell and Ross sea. In the northern hemisphere, the grid size of the MPI-OM grid is more comparable to that of ICON-O.

Overall, there are considerable differences between ICON-O and MPI-OM in the numerics, in the applied parameterizations, and horizontal and vertical grid used. This is why we consider both model configurations as independent. A comparison of the LEC diagnosed for both of these model configurations in Section 2.4, allows us to identify the robust and model-independent features of the ocean's energy pathways.

To enhance comparability, the treatment of the output for both ICON-O simulations are carried out in the same way as it was done with the MPI-OM simulation in von Storch et al., 2012. The MPI-OM simulation was obtained by forcing MPI-OM with the NCEP reanalysis, hereafter referred to as MPIOM/NCEP (see von Storch et al., 2012 for more details of the setup). One of the two ICON-O simulations, hereafter referred to as ICON/NCEP, is conducted exactly in the same way as MPIOM/NCEP. It is spun up for 25 years using heat, freshwater and momentum fluxes obtained from the German Ocean Model Inter-comparison Project (OMIP) climatology forcing (Röske, 2006). After the spin-up phase, the forcing is switched to the 6-hourly NCEP reanalysis dataset (Kalnay et al., 1996) and the model is integrated from 1948 to 2019. The second ICON-O simulation, ICON/ERA5, is generated by branching from the ICON/NCEP simulation in 1980 and replacing the NCEP forcing with the ERA5 forcing dataset (Hersbach et al., 2020). A summary of the model simulations is presented in table 2.1.

Data output from the same 10 years, namely from 2001-2010, are used to estimate the 10-year averaged LEC in the three simulations. Analogous to von Storch et al., 2012, eddies are defined as deviations from the time mean that fluctuate on timescales ranging from the model time step to 10 years. The individual terms of LEC, namely the energy reservoirs K_m, K_e, P_m and P_e, the generations of these reservoirs $G(K_m)$, $G(P_e)$, $G(K_m)$ and $G(K_e)$, as well as the conversion terms $C(P_m, K_m)$, $C(P_m, P_e)$, $C(P_e, K_e)$ and $C(K_m, K_e)$, are defined in Appendix A. For a conversion term $C(X, Y)$, the convention is such that $C(X, Y) = -C(Y, X)$ and the direction of $C(X, Y)$ goes from X to Y. Hereafter we use capital letters to indicate globally integrated energy terms, and small letters to indicate local energy terms. Since the magnitudes of the mean and eddy available potential energy depend on the reference density ρ_{ref} used, it is difficult to discuss the magnitudes of these energy terms.

There might also be an error in P_m obtained from MPIOM/NCEP, which is two orders of magnitudes larger than P_m in ICON/NCEP and ICON/ERA5. This however cannot be further confirmed, since not all data from MPIOM/NCEP, which was carried out more than 10 years ago, are available for us. P_m and P_e will nevertheless be calculated and listed for the sake of completeness. The data still available from MPIOM/NCEP are the 3-dimensional velocities and the global integrated numbers as listed in von Storch et al., 2012. The comparison with the MPIOM/NCEP LEC, to be discussed in Section 2.5.1, will hence be based essentially on the published results (von Storch et al., 2012). Analogous to MPIOM/NCEP, the second moments needed for calculating the LEC terms for ICON/NCEP and ICON/ERA5 are generated at every model time step, and outputted on a monthly basis. We note that in this way, p_e and k_e result from transient motions that vary on timescales ranging from the model time step to the time average period of 10 years. We expect that the transients are dominated by mesoscale eddies arising from baroclinic and barotropic instability throughout the ocean and by near-inertial waves near the surface. For simplicity, we refer to k_e and p_e as eddy kinetic energy and eddy available potential energy, even though they are not related to mesoscale eddies only.

2.3.2 Surface forcing

We use two reanalyses data sets ERA5 (Hersbach et al., 2020) and NCEP (Kalnay et al., 1996) as surface forcing for the temperature, salinity and momentum equations of the ICON-O simulations. The wind stress, used to mechanically drive ICON-O and MPI-OM, is thereby taken directly from the reanalyses products without considering the ocean velocity in the derivation of the stresses. This leads to an overestimation of the wind energy input, which needs to be kept in mind when interpreting our results (Zhai et al., 2012). The heat and freshwater flux are derived based on bulk formulae using a combination of meteorological variables from the reanalyses and the simulated ocean surface temperature.

The surface forcing from the NCEP reanalysis product differs significantly from the ERA5 reanalysis product, concerning both the mean and the variability of the surface fluxes. The higher spatial-temporal resolution of ERA5 (31 km, hourly) relative to NCEP (200 km, 6 hourly) leads to stronger variability in the surface fluxes in ERA5 than in NCEP. As shown by the difference between standard deviation of ERA5 fluxes and that of NCEP fluxes (Fig.2.1), enhanced variability is found for all three fluxes in most part of the ocean outside the polar regions. Regarding the wind stress, the largest difference in variability is found in the storm track regions over the mid-latitude oceans where a maximum of about 0.02 N/m^2 is reached. A similar picture is found for the heat flux, where the difference in the variability reaches values up to 30 W/m^2 in the Gulf Stream and Kuroshio. For the freshwater flux, the largest difference of more than 4 mm/day is found in the tropics, especially in the central and eastern tropical Pacific and in the tropical Atlantic. These differences in standard deviations are of comparable magnitudes as the zonally averaged time-mean fluxes shown Fig.2.2.

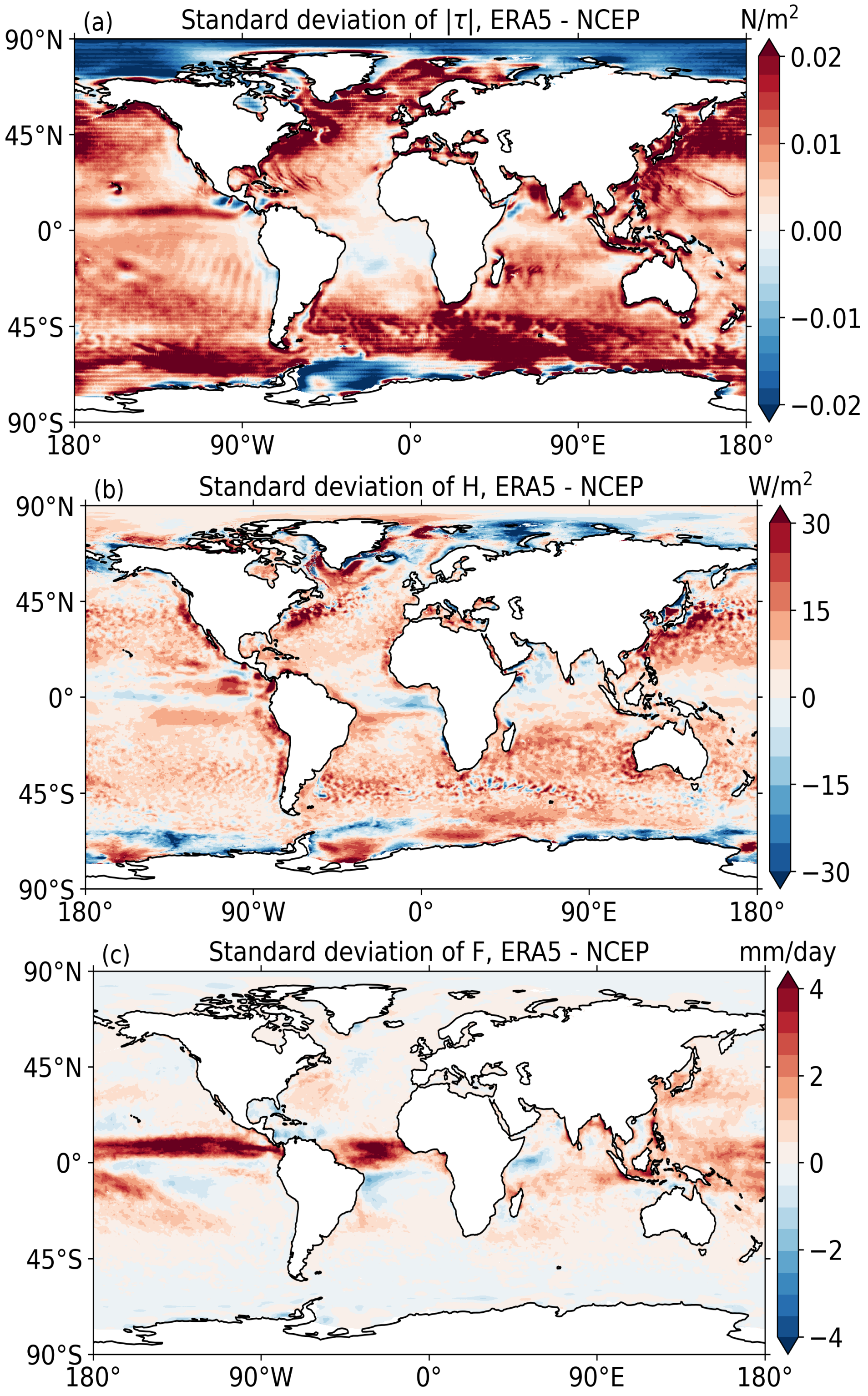

Figure 2.1: Difference in the standard deviation of surface forcing (ERA5 minus NCEP) for a) magnitude of wind stress, b) net heat flux, and c) net fresh water flux, obtained from 1 hourly ERA5-reanalysis and 6 hourly NCEP-reanalysis over the common 10-year period from 2001-2010. The standard deviations of heat and freshwater are estimated using monthly averages and therefore represent time-variations between one month and 10 years

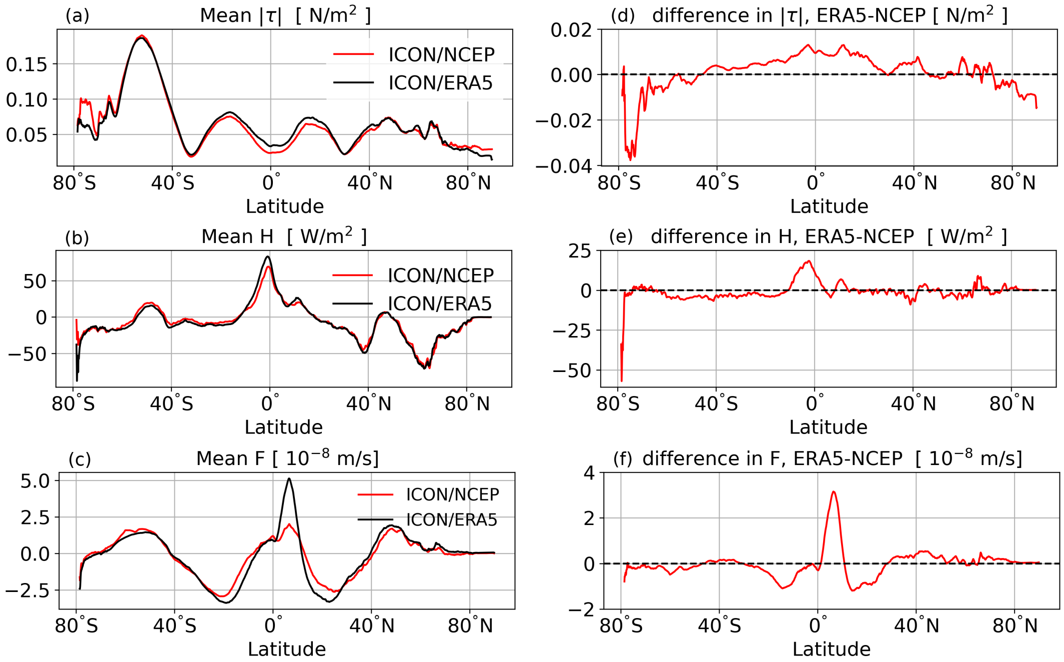

Figure 2.2: Time-mean zonal-mean fluxes (left) of momentum (top), heat (middle), and fresh water (bottom), derived from ERA5- (black) and NCEP-reanalysis (red) and the difference between ERA5 and NCEP (right). The fluxes are calculated for the common 10-year period from 2001-2010

The zonally averaged time-mean fluxes obtained from the ERA5-reanalysis (black lines in the left column of Fig.2.2) are mostly comparable to those obtained from the NCEP-reanalysis (red lines in the left column of Fig.2.2). However, there exists also noticeable differences between the two (right column of Fig.2.2). Relative to NCEP, ERA5 wind stress is stronger over the tropical and subtropical oceans and weaker over the high-latitude oceans. ERA5 heat flux is noticeably larger than the NCEP heat flux near and south of the Equator. For the freshwater flux, the ERA5 flux in a narrow latitudinal band just north of the equator is more than twice as strong as the NCEP flux.

The large differences in the variability of fluxes, together with the changes in the mean fluxes, could produce differences in the generation of kinetic energy and available potential energy at the sea surface. Whether and how these different generations affect the energy pathways inside the ocean will be analyzed in section 2.5.2.

Table 2.1: Summary of the simulations

	ICON/NCEP	**ICON/ERA5**	**MPIOM/NCEP**
Model	ICON-O	ICON-O	MPI-OM
Model horizontal resolution	10 km	10 km	10 km. South of the equator, the grid size is 0.1° $\cos(\phi)$, where ϕ is latitude
Model vertical resolution	128 (8 - 200) m	128 (8 - 200) m	80 (10 - 279) m
Forcing	NCEP/NCAR	ERA5	NCEP/NCAR
Forcing resolution	200 km, 6 hr	31 km, 1 hr	200 km, 6 hr

2.4 LORENZ ENERGY CYCLE IN ICON/NCEP

This section describes the LEC derived from ICON/NCEP, which will be used as the reference LEC for assessing the sensitivity of LEC to model difference and to forcing difference. The ICON/NCEP LEC is depicted by black bold numbers in Fig. 2.3. Overall, the generation and dissipation terms, G_X and D_X, are larger than the conversion terms, $C(X,Y)$. This suggests that a large portion of the energy input does not lead to transformations between eddies and mean circulation or between kinetic and potential energy but that the energy which is put in at the ocean surface might be dissipated without being transformed to another energy compartment of the LEC. The generation of P_e, $G(P_e)$ in ICON/NCEP is consistent with the new findings in Bishop et al., 2020, namely that when $G(P_e)$ is decomposed into two parts, one associated to the seasonal cycle and the other with all non-seasonal time scales, the latter is a sink for P_e, especially along the Gulf stream, Kuroshio and in the tropical oceans. The strongest conversion among the LEC energy compartments is that between mean available potential and eddy available potential energy $C(P_m,P_e)$ and the consecutive conversion from eddy available into eddy kinetic energy $C(P_e,K_e)$. This energy pathway is frequently associated with baroclinic instability arising from vertical shear of horizontal velocity.

Hereafter, we will refer to the conversion from P_m via P_e to K_e as the baroclinic pathway; However, it should be noted that also a considerable amount of eddy available potential energy is introduced and an even larger amount is dissipated along this pathway. We would like to note that diapycnal mixing within the geostrophic mesoscale circulation is expected to be small in reality. In this regard, the large dissipation of P_e might either occur within regions of enhanced diapycnal mixing like the upper-ocean mixed layer or it occurs due to numerical mixing by the discretized tracer advection. In the ICON/NCEP run, the baroclinic pathway consists of $C(P_m,P_e)$ that amounts to 0.84 TW and $C(P_e, K_e)$ that amounts to 0.49 TW.

The third strongest conversion is that of $C(K_m, P_m)$, which amounts to about 0.4 TW. The weakest conversion is $C(K_m, K_e)$, which amounts to about 0.17 TW. Since $C(K_m, K_e)$ is related to momentum flux along the horizontal gradient of horizontal velocity, and since a strong horizontal shear in horizontal velocity can result in barotropic instability, $C(K_m, K_e)$ will be hereafter referred to as the barotropic pathway. Below we describe the conversions associated with different pathways in ICON/NCEP in more detail.

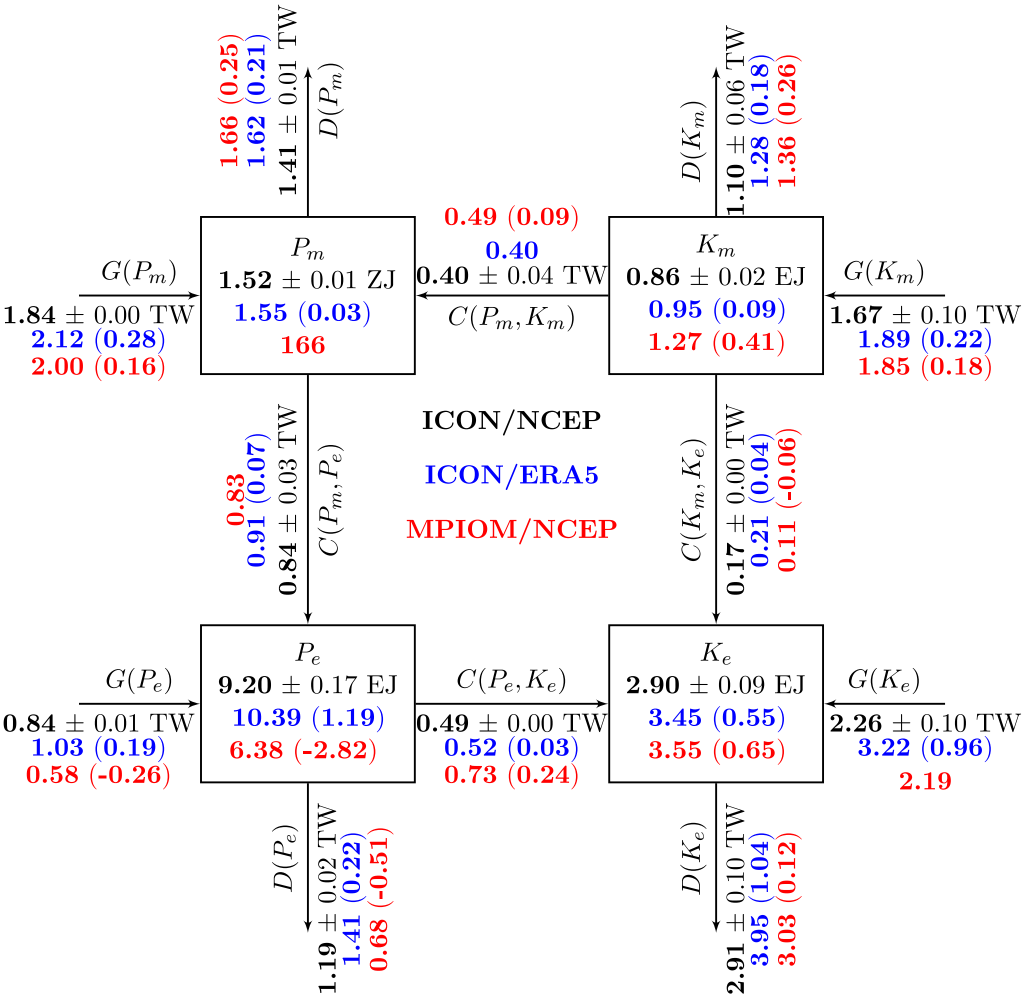

Figure 2.3: LEC for ICON/NCEP (black), ICON/ERA5 (blue) and MPIOM/NCEP (red). The values corresponding to MPIOM/NCEP are adopted from von Storch et al., 2012. The energy reservoirs are in exajoules (EJ, 10^{18}) and zettajoules (ZJ, 10^{21}). The generation, exchange and dissipation terms are in terawatts (TW, 10^{12}). The red bracketed numbers are model differences (MPIOM/NCEP minus ICON/NCEP) and the blue bracketed numbers are forcing differences (ICON/ERA5 minus ICON/NCEP). Only those differences, which are larger than the typical magnitude of sampling errors, are indicated by bracketed numbers

Integrated vertically, the conversion from p_m to p_e (Fig.2.4, top) tend to occur at the same place where p_e is converted into k_e (Fig.2.4, bottom), such as along the Gulf Stream and Kuroshio, around Azores in the North Atlantic, along fronts in the Southern Ocean, as well as in the central eastern equatorial Pacific and the central eastern equatorial Atlantic. Outside the equatorial region, this co-occurrence is indicative of the baroclinic pathway from p_m to p_e and eventually to k_e. Less clear is the co-occurrence near the equator where geostrophy breaks down, but the energy is nevertheless transferred from p_m to p_e and subsequently to k_e as if it is driven by baroclinic instability. In the Gulf Stream and Kuroshio, especially where the two currents start to be detached from the coast, and also occasionally in Southern Ocean fronts, the opposite pathway going from k_e to p_e and eventually to p_m is also observed.

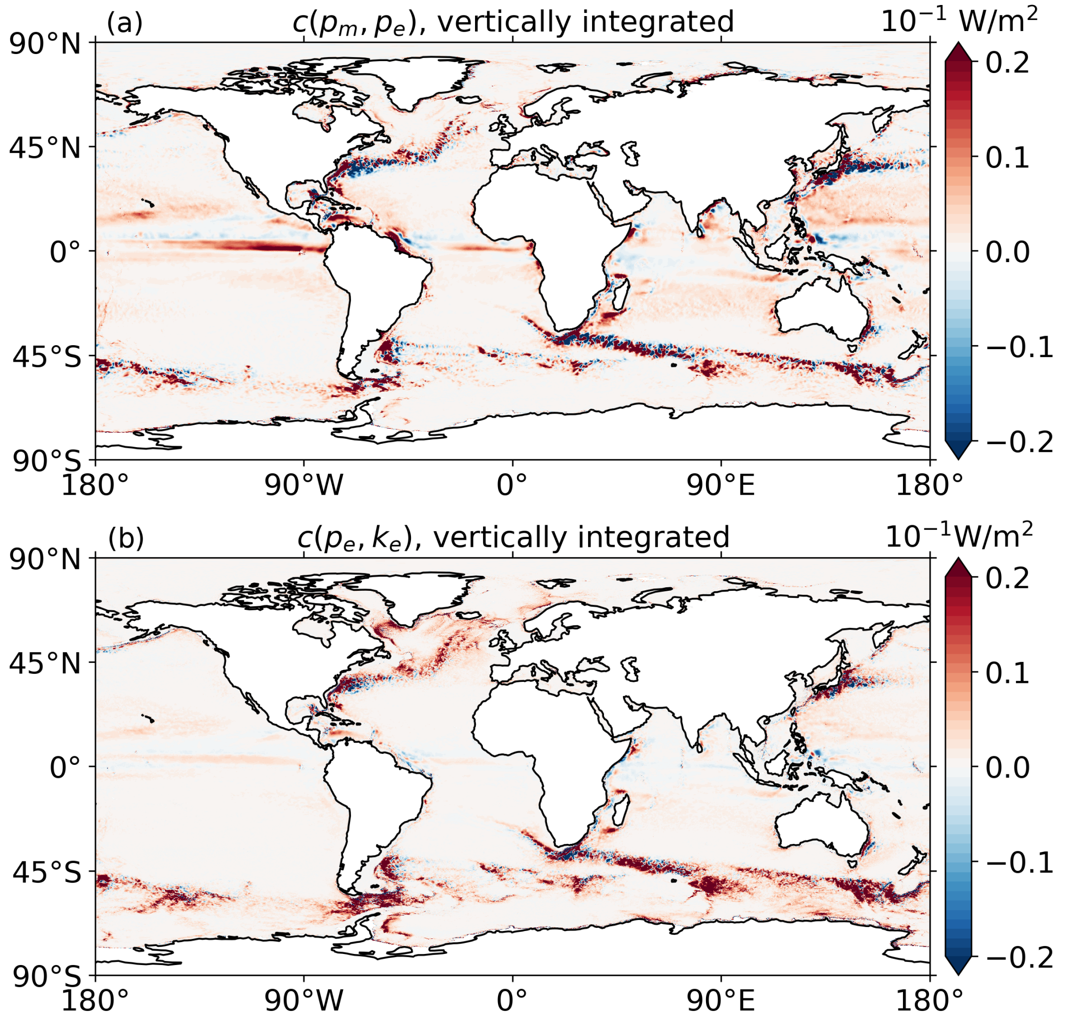

Figure 2.4: Horizontal distribution of the vertically integrated conversion rate from mean available potential energy to eddy available potential energy, $c(p_m, p_e)$ (top) and from eddy available potential energy to eddy kinetic energy, $c(p_e, k_e)$ (bottom)

Fig.2.5 shows the latitude and depth cross-section of the zonally integrated conversion $c(p_m, p_e)$ and the conversion $c(p_e, k_e)$. Since these conversions occur mainly along the boundary currents outside the Southern Ocean, but all over the place in the Southern

Ocean, the zonally integrated conversions are much stronger in the Southern Ocean than elsewhere. In the Southern Ocean, the baroclinic conversion, with magnitudes larger than 80 mW/m^2, occurs up to a depth of 4 km. The strong conversion from p_m to p_e and to k_e found in the equatorial Pacific and equatorial Atlantic in Fig.2.4 is confined to a thin surface layer.

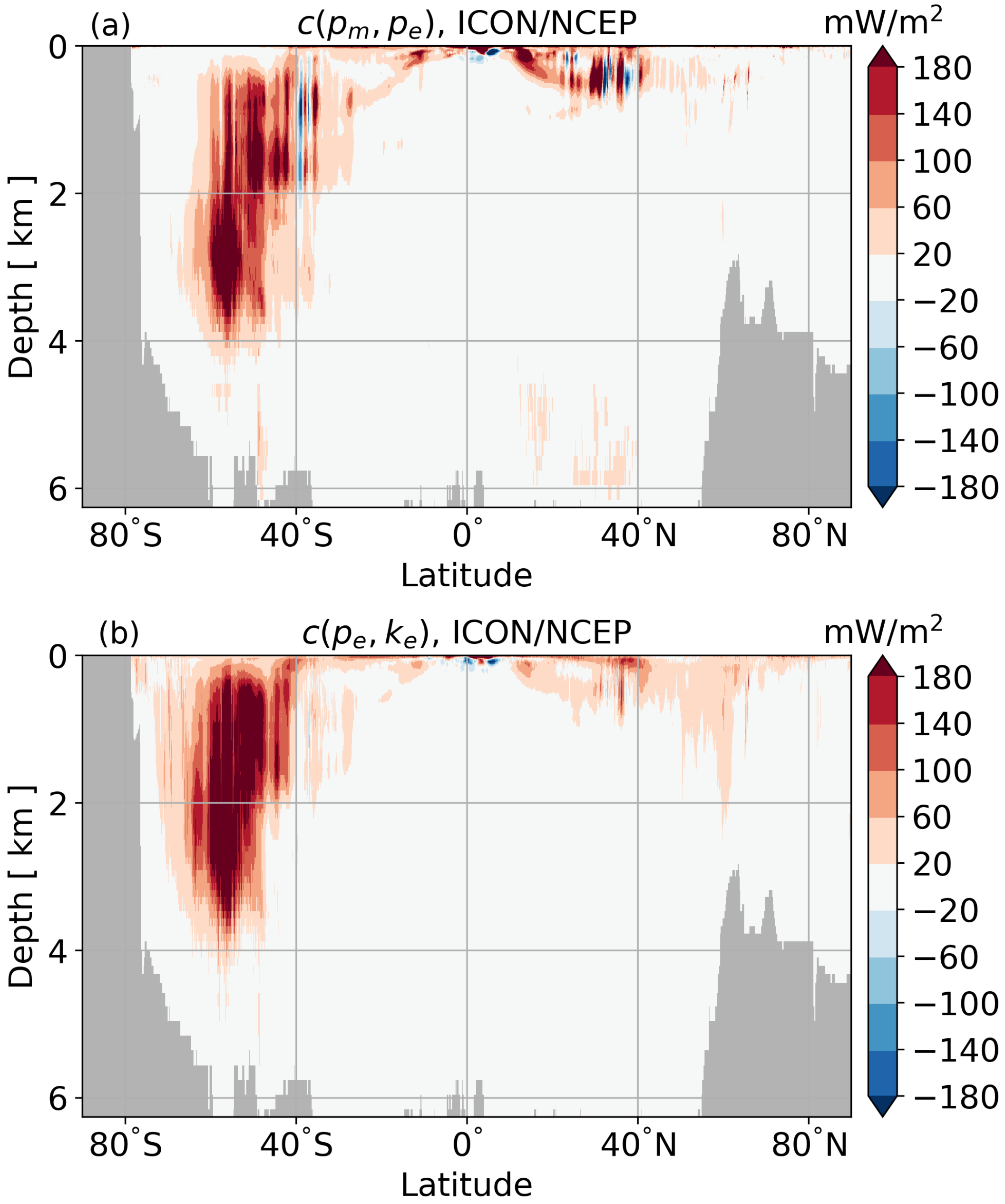

Figure 2.5: Depth-latitude sections of the zonally integrated conversions $c(p_m, p_e)$ (top) and $c(p_e, k_e)$

Away from the baroclinic pathway, there is a sizable conversion of mean kinetic energy to mean available potential energy (i.e. negative $c(p_m, k_m)$). This happens where relatively dense water masses are moved upwards or relatively light water masses are moved downwards, resulting in the spatial distribution of $c(p_m, k_m)$ shown in Fig.2.6 (top). Note that dense and light waters are defined relative to the reference density

ρ_{ref}. The strong positive values along the equator result from upwelling of light water, or more precisely upwelling of water lighter than ρ_{ref}. Generally, the distribution of $c(p_m, k_m)$ is strongly linked to the distribution of Ekman pumping / sucking velocity, which is predominantly strong in the upper 100 m in the equatorial region (Chereskin and Roemmich, 1991). Regions with strong Ekman velocities e.g. the Southern Ocean, along eastern boundaries and the tropical ocean have strong $c(p_m, k_m)$ conversion rates. The stronger negative values in the Southern Ocean are due to upwelling of water denser than the reference density profile. In the mid-latitudes, the conversion is positive due to the down-welling of relatively dense water. The bottom panel of Fig.2.6 shows that the conversion $c(p_m, k_m)$, with absolute magnitude of above 0.8 W/m^2, is confined to the upper 100 m near the equator, but extends to about 3000 m in the Southern Ocean. The horizontally integrated $c(p_m, k_m)$ is negative in the upper 3000 m and positive below (Fig.2.7, left) indicating that the conversion is from the mean kinetic energy k_m to mean available potential energy p_m above but the other way around below 3000 m.

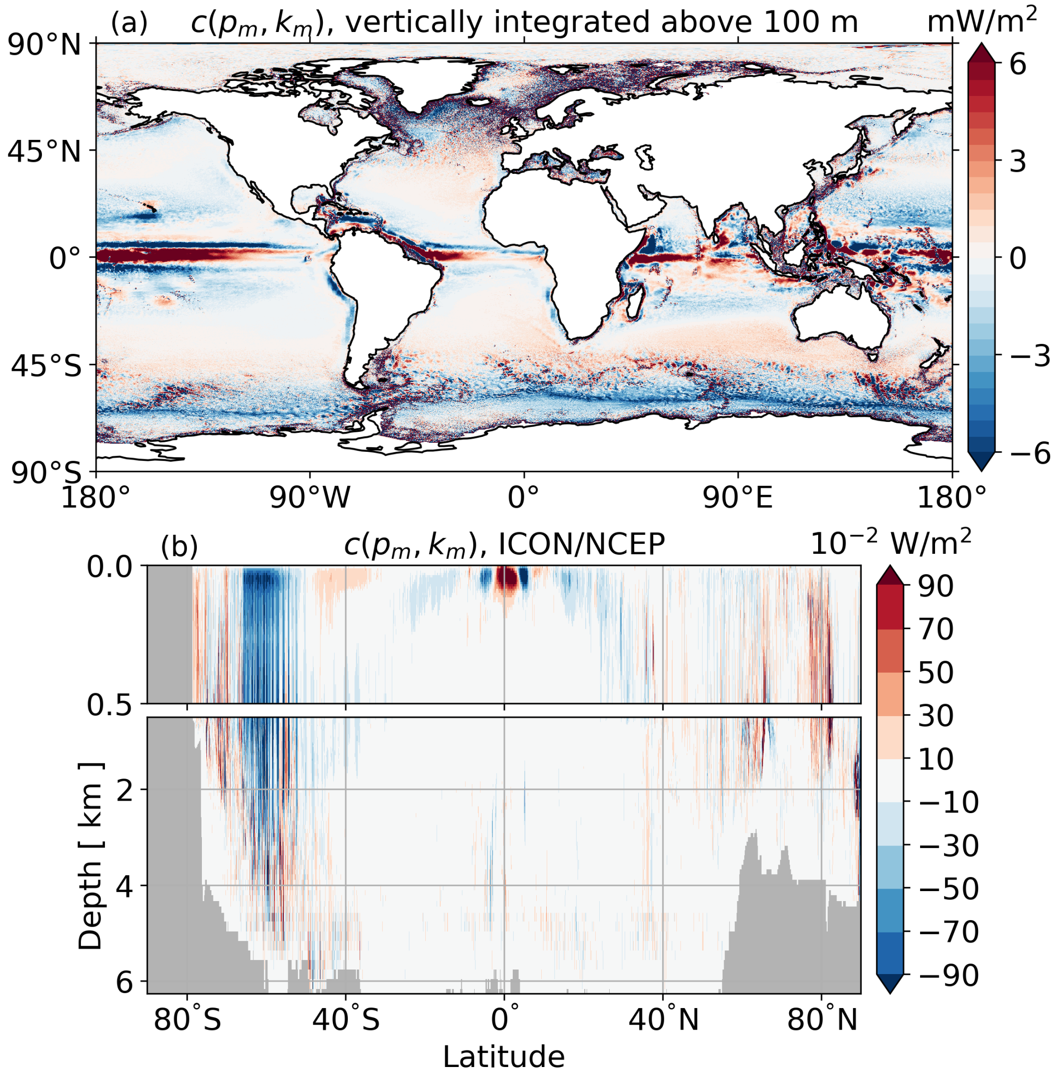

Figure 2.6: (top) Horizontal distribution of the vertically integrated (above 100 m) conversion rate from mean available potential energy to mean kinetic energy, $c(p_m, k_m)$ (bottom) depth-latitude section of the zonally integrated $c(p_m, k_m)$

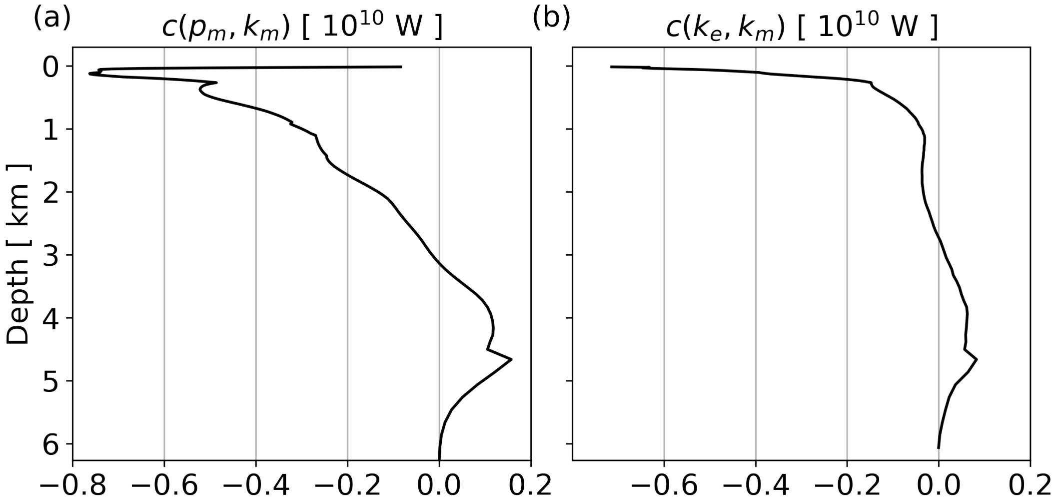

Figure 2.7: Vertical profiles of $c(p_m,k_m)$ (left) and $c(k_e,k_m)$

The weakest globally integrated conversion of the ICON/NCEP LEC is that from mean kinetic energy to eddy kinetic energy (negative $c(k_e,k_m)$). Large values of $c(k_e,k_m)$ that change their sign within a short distance of a few grid cells are found in the Gulf Stream, Kuroshio and in the frontal regions in the Southern Ocean (not shown). Loose et al., 2023 observed a similar behaviour — abrupt sign change in the barotropic exchange term — after applying spatial filtering on simulations from an isopycnal 1/32° idealised model of the Southern and Atlantic ocean. When $c(k_e,k_m)$ integrated zonally (Fig.2.8), a systematic picture emerges. We find a conversion from mean kinetic energy to eddy kinetic energy (negative $c(k_e,k_m)$) in the upper 3 km of the ocean, and a conversion from eddy kinetic energy to mean kinetic energy (positive $c(k_e,k_m)$) below 3 km. The former likely arises from barotropic instability due to the strong horizontal shears in the upper ocean velocities. The latter might be a sign of an inverse energy cascade where energy is transferred back from the eddy field (k_e) to the mean circulation (k_m). The vertical profile of horizontally integrated $c(k_e,k_m)$ (Fig.2.7, right) confirms the reversal of the sign of $c(k_e,k_m)$ at about 2.8 km. It shows further that the strength of the conversion from k_m to k_e in the upper 100 to 200 m is much stronger than the opposite conversion from k_e to k_m with a maximum just below 4.5 km. Integrated not only horizontally but also vertically, this therefore results in a global energy conversion from k_m to k_e as the residue from counter acting energy fluxes.

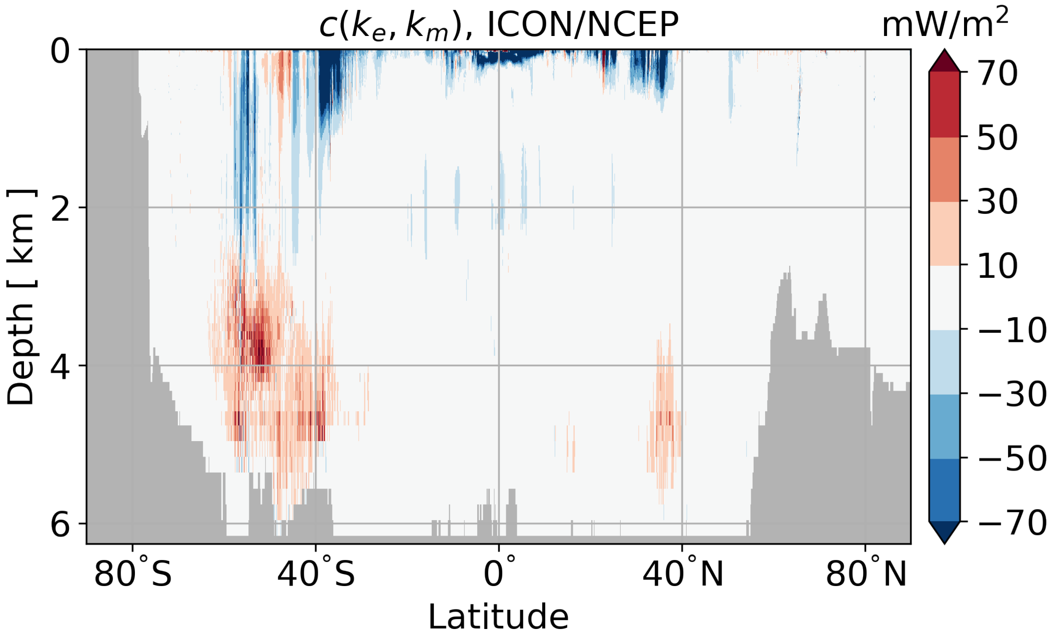

Figure 2.8: Depth-latitude section of zonally integrated conversion $c(k_e, k_m)$.

2.5 SENSITIVITY OF LORENZ ENERGY CYCLE

In the following, we will discuss two sensitivities of the reference LEC obtained from ICON/NCEP: first with respect to the difference of LEC obtained with MPIOM/NCEP and second with respect to the difference LEC obtained with ICON/ERA5. In Fig.2.3, we indicate the different values for the energy reservoirs and the energy conversions with black for the reference ICON/NCEP simulation, with blue for ICON/ERA5 and with red for MPIOM/NCEP. Differences to the reference simulation for ICON/ERA5 and MPIOM/NCEP are indicated by the numbers in brackets.

To estimate the significance of these changes, we compare them against the typical magnitude of LEC variability Δ arising from sampling errors. Therefore, we split the 10 years of the ICON/NCEP output into two 5-year chunks and estimate the LEC for each of these two chunks. This difference of the LEC components obtained from the two chunks of the same simulation is then Δ, our measure for the LEC variability due to sampling error that also exists without changing model or changing surface forcing (a more precise estimate of the sampling error is cost intensive and beyond the scope of this study). Hereafter, a model or forcing differences of single LEC components will be considered significant when they are larger than this Δ from sampling error variability. Only those differences which pass this "poor-man's" significance test are indicated in Fig.2.3. In most cases, the model or forcing differences are, however, substantially larger than the sampling variability which gives us confidence that most observed changes can be considered as significant.

2.5.1 Sensitivity to model difference

The LEC terms derived from MPIOM/NCEP (red numbers in Fig.2.3, taken from von Storch et al., 2012) and those derived from ICON/NCEP (black numbers) reveal the following same gross features: First, the generation and dissipation terms balance each other to the lowest order and have magnitudes that are noticeably larger than those of the conversion terms. Secondly, the directions of all interior conversions are the same in MPIOM/NCEP and ICON/NCEP. Finally, the strongest pathway is the baroclinic pathway that converts P_m to P_e and eventually to K_e; the second strongest pathway is the conversion from mean kinetic energy K_m to mean available potential energy P_m; and the weakest one is the conversion from mean kinetic energy K_m to eddy kinetic energy K_e.

These agreements are encouraging, given that MPI-OM and ICON-O are two completely different ocean models since they suggest that the described gross features of the energy pathways are robust not only in terms of their directions, but also in terms of their magnitudes. For both models, the conversion from mean available potential energy P_m to eddy available potential energy P_e is about 0.8 TW, the conversion from mean kinetic energy K_m to eddy kinetic energy K_e is about 0.4-0.5 TW, and the conversion from mean kinetic energy K_m to eddy kinetic energy K_e is about 0.1-0.2 TW. While the similarity of these numbers is encouraging, it should also be noted that both models have relatively similar resolution over large parts of the ocean. Thus, both models do not resolve scales substantially smaller than the first baroclinic Rossby radius. To this end, they also do not resolve sub-mesoscale dynamics or lee wave generation by eddies. We can therefore not conclude that the numbers which we obtain from the models considered here will also hold when these other dynamical regimes are explored.

Apart from the above common features, the LEC derived from ICON/NCEP, especially with respect to interior conversions, deviates from that derived from MPIOM/NCEP in some aspects. While the first part of the baroclinic pathway, i.e. the conversion from P_m to P_e, is comparable in ICON/NCEP and MPIOM/NCEP, the second part of this pathway, i.e. from P_e to K_e, is about 50% stronger in MPIOM/NCEP than in ICON/NCEP. For the conversion from mean kinetic energy K_m to eddy kinetic energy K_e, it is about 30% stronger in ICON/NCEP than in MPIOM/NCEP. Below we analyse these differences in the baroclinic pathway and in the barotropic pathway in more detail.

For the baroclinic pathway, we first compare the geographical distributions of vertically integrated $c(p_m, p_e)$ and $c(p_e, k_e)$ in ICON/NCEP (Fig.2.4) with those in MPIOM/NCEP (Fig.8 and Fig.9 in von Storch et al., 2012). These distributions compare well with each other, not only with respect to the locations of maxima of $c(p_m, p_e)$ and $c(p_e, k_e)$ in the regions of expected strong baroclinic instability along the Gulf Stream, Kuroshio and the fronts in the Southern Ocean, but also in the central and eastern equatorial Pacific and the central and eastern equatorial Atlantic. Thus, the weaker conversion $C(P_e, P_m)$ in ICON/NCEP than in MPIOM/NCEP cannot be explained by the difference in the overall spatial distribution of these conversions.

Since the conversion $c(p_e, k_e)$ is determined by the covariance between density anomaly ρ' and vertical velocity anomaly w', we suspect that the weak conversion $C(p_e, k_e)$ in ICON/NCEP is related to the smaller magnitude of w' in ICON/NCEP than in MPIOM/NCEP. Given that the 3-dimensional velocity from MPIOM/NCEP is still available to us, we check this by calculating the standard deviation of w', $\sigma_{w'}$, and use the area averaged $\sigma_{w'}$ as a measure for typical magnitude of w' in ICON/NCEP and MPIOM/NCEP (Fig.2.9, left). We find that in MPIOM/NCEP, $\sigma_{w'}$ is about factor 5 to 6 stronger between 50°S - 70°S than north of 10°N, reaching values of about 0.5 to 0.6 mm/s between 50°S - 70°S below 1 km (red solid and red dashed line). In ICON/NCEP, however, $\sigma_{w'}$ has comparable magnitude, around 0.1 to 0.2 mm/s, both between 50°S - 70°S and north of 10°N (black solid and black dash line). Some of these variations in w' may be correlated with ρ', resulting in weaker $C(P_e, P_m)$ in ICON/NCEP than in MPIOM/NCEP.

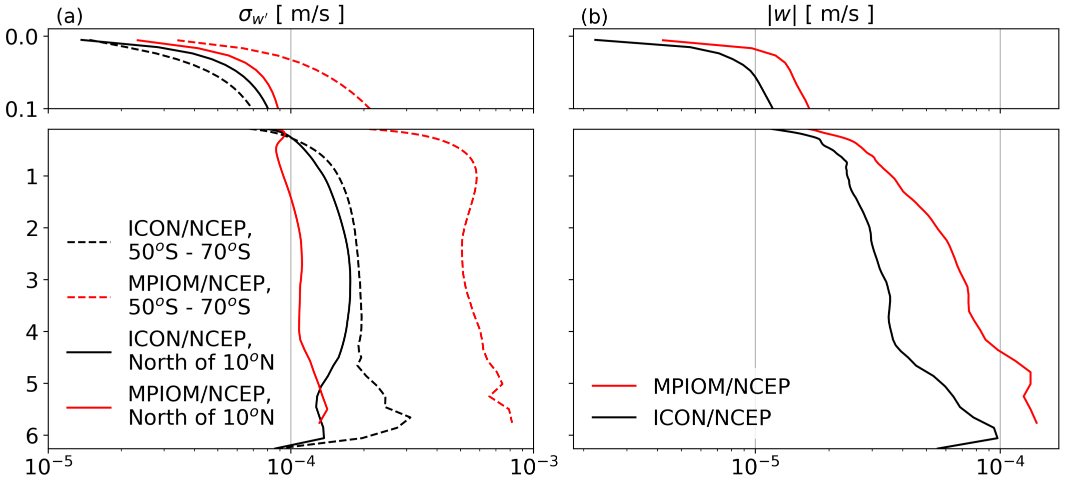

Figure 2.9: Standard deviation of w' over 5 years (2001 - 2005) (left) averaged horizontally over the latitudinal band from 70°S to 50°S (solid) and over the region north of 10°N (dashed), and the global averaged magnitude of the time-mean vertical velocity $|\overline{w}|$ (right) in MPIOM/NCEP (red) and in ICON/NCEP (black).

The large variability in w' shown in Fig.2.9 can be, at least partially, related to quasi-geostrophic eddies emerging from baroclinic instability. Note that Fig.2.10b points to a stronger eddy activity (stronger k_e) in the Southern Ocean in MPIOM/NCEP compared with ICON/NCEP. This stronger eddy activity in the Southern Ocean in MPIOM/NCEP is likely a consequence of the higher horizontal resolution of MPIOM/NCEP compared with ICON/NCEP.

From the assumption that the mesoscale eddy field is not causing substantial amounts of diapycnal mixing in the ocean interior, it would follow that $c(p_m, p_e)$ and $c(p_e, k_e)$ should have comparable magnitudes below the mixed layer. However, the numbers in Fig.2.3 show that $C(P_e, K_e)$ is slightly weaker than $C(P_m, P_e)$ in MPIOM/NCEP. This highlights the effect of either upper ocean diapycnal mixing or nonphysical numerical mixing.

In ICON/NCEP this difference is even stronger, with $c(p_e, k_e)$ amounting to 58% of $c(p_m, p_e)$ in ICON/NCEP, compared to 88% in MPIOM/NCEP. The difference between the models suggests that the ICON-O configurations applied here have more diapycnal mixing compared to MPIOM. Support for this hypothesis comes from the result of Mohammadi-Aragh et al., 2015 that in a configuration with a lower grid Reynolds number, baroclinic instability occurring close to the grid scale can lead to higher numerical mixing. With the lower resolution of ICON-O than in MPI-OM in the eddy-active Southern Ocean, the grid Reynolds number in ICON-O is lower than that in MPI-OM there. The numerical dissipation of p_e and k_e and with that the reduction in $c(p_e, k_e)$ can be stronger in the Southern ocean in ICON-O than in MPI-OM.

Probably, the strength of $C(P_e, K_e)$ in ICON/NCEP can be enhanced by increasing the resolution at higher latitudes, however, this investigation is beyond the scope of this study. It remains an open question to which degree the diapycnal mixing responsible for the dissipation of p_e in all model simulations (but strongest in ICON) is caused by diabatic processes in the upper-ocean mixed layer or by interior physical or numerical water mass conversions.

For the barotropic pathway described by $c(k_m, k_e)$, whose global integral is smaller in MPIOM/NCEP (0.11 TW) than in ICON/NCEP (0.17 TW), we compare the vertical profile of horizontal integrated $c(k_e, k_m)$ shown in Fig.2.7 (right) with the same profile derived from MPIOM/NCEP (Fig.11a) in von Storch et al., 2012. Both profiles show a similar sign reversal around 2.5 to 3 km. However, the horizontal integral of $c(k_e, k_m)$ is noticeably smaller in the ocean interior in ICON/NCEP than in MPIOM/NCEP. The maximum of the positive conversion from k_e to k_m around 4 km amounts to about 0.35 $\times 10^{10}$ W in MPIOM/NCEP, but is below 0.1 $\times 10^{10}$ W in ICON/NCEP. So the larger value of $C(K_m, K_e)$ in ICON/NCEP is caused by weaker counter conversion in the deep ocean in ICON/NCEP than in MPIOM/NCEP.

For the conversion from mean kinetic energy to mean available potential energy$c(k_m, p_m)$, whose global value is larger in MPIOM/NCEP than in ICON/NCEP, we compare the vertical profile of horizontally integrated $c(p_m, k_m)$ shown in Fig.2.7 (left) with the same profile derived from MPIOM/NCEP (Fig.12 in von Storch et al., 2012). Both profiles show negative values of $c(p_m, k_m)$ above 3 km and positive values below 3 km. However, the magnitude of $c(p_m, k_m)$ is larger in MPIOM/NCEP than that in ICON/NCEP. The minimum of the horizontally integrated $c(p_m, k_m)$ amounts almost to -1.5$\times 10^{10}$ W in MPIOM/NCEP, but is barely - 0.8$\times 10^{10}$ W in ICON/NCEP. The maximum of the horizontally integrated $c(p_m, k_m)$ at about 4 km amounts to about 0.6$\times 10^{10}$ W in MPIOM/NCEP, but reaches barely 0.2$\times 10^{10}$ W in ICON/NCEP. The smaller magnitude of $c(p_m, k_m)$ in ICON/NCEP compared with MPIOM/NCEP is most likely caused by a weaker time-mean vertical velocity in ICON/NCEP than in MPIOM/NCEP as can be inferred from Fig.2.9b. Since the same surface forcing is

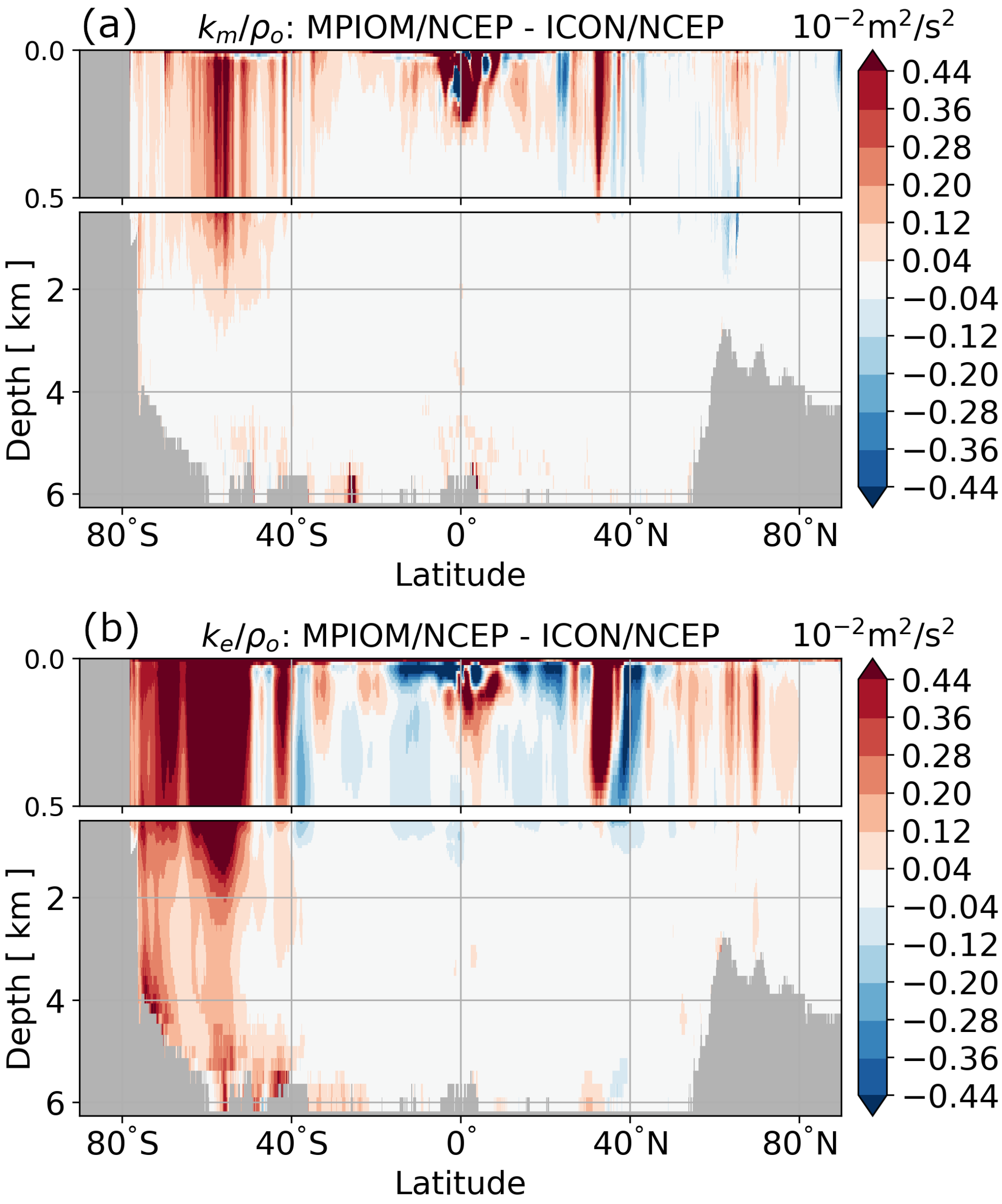

Figure 2.10: Differences in zonally averaged $k_m/\rho_\circ$ between MPIOM/NCEP and ICON/NCEP (top) and in zonally averaged $k_e/\rho_\circ$ between MPIOM/NCEP and ICON/NCEP (bottom) in m^2/s^2.

used, the increase in mean vertical velocity is likely caused by the different time-mean circulations in ICON/NCEP and MPIOM/NCEP. When integrated globally, the strong conversion from K_m to P_m in MPIOM/NCEP results in a global $C(K_m, P_m)$ of about 0.49 TW, which is larger than $C(K_m, P_m)$ of about 0.4 TW in ICON/NCEP.

2.5.2 Sensitivity to forcing difference

In this section, we assess the sensitivity of the global LEC to surface forcing by comparing the LEC terms derived from ICON/ERA5 (blue numbers in Fig.2.3) with those derived from ICON/NCEP (black numbers).

For each of the four energy compartments, K_m, K_e, P_m, and P_e, the generation terms increase substantially. However, also the dissipation terms increase by nearly the same amount (compare blue bracketed numbers in Fig. 2.3 for the forcing differences in the generation and dissipation terms). More specifically, $G(K_e)$ is increased by about 42% from its value in ICON/NCEP and becomes almost 1 TW stronger in ICON/ERA5. The generation of eddy available potential energy $G(P_e)$ is increased by about 23% from its value in ICON/NCEP and becomes almost 0.2 TW stronger in ICON/ERA5.

Fig.2.13 shows that the large increases in the generation of eddy kinetic energy $g(k_e)$ is most dominant in the mid- to high-latitude regions, whereas the large increases in the generation of eddy available potential energy $g(p_e)$ are more concentrated on the Gulf Stream and Kuroshio region. Dissipation increases in ICON/ERA5 by about 36% for K_e and 18% for P_e. Regarding the mean kinetic energy and mean available potential energy, the increases in the generation, reaching 13% in $G(K_m)$ and 15% in $G(P_m)$, are accompanied by increases in dissipation as well, reaching 16% in K_m and 15% in P_m.

The largest changes in the conversion terms concerns the barotropic pathway from K_m to K_e, which is about 24%, or 0.04 TW, stronger in ICON/ERA5 than in ICON/NCEP. The baroclinic pathway increases by about 8% for $C(P_m, P_e)$ and 6% for $C(P_e, K_e)$ in ICON/ERA5 than in ICON/NCEP. The conversion from K_m to P_m is not notably affected by the forcing difference. Except for $C(K_m, P_m)$, forcing-induced changes in all terms of the LEC are statistically significant with respect to our "poor man's" test. Nevertheless, since the test is not precise, we will focus only on the biggest change in the generation $G(K_e)$ and the biggest relative change in the conversion $C(K_m, K_e)$. Both affecting the eddy kinetic energy K_e.

We start our consideration with the forcing difference in conversion $c(k_e, k_m)$. Fig.2.11 shows that the mean kinetic energy k_m is more strongly converted to eddy kinetic energy in ICON-ERA5 than in ICON/NCEP in the upper 500 m in the low-latitude oceans equator-ward of about 40°. This latitudinal band coincides roughly with the band where the time-mean wind stress is stronger in ERA5 than in NCEP (upper right panel in Fig.2.2). Integrated globally, the generation of mean kinetic energy is somewhat stronger in ICON/ERA5 than in ICON/NCEP. We hence hypothesize that the stronger mean wind stress in ERA5 leads to a stronger generation in mean kinetic energy and with that stronger time-mean currents. Fig.2.12a shows indeed that apart from a few interruptions by narrow latitudinal bands where k_m decreases, the zonally averaged value in ICON/ERA5 is increased from 40°S to 45°N; albeit, the increase is much stronger in the tropical oceans from about 10°S to 10°N. The stronger time-mean currents could then lead to a stronger conversion $c(k_m, k_e)$. The enhanced zonally

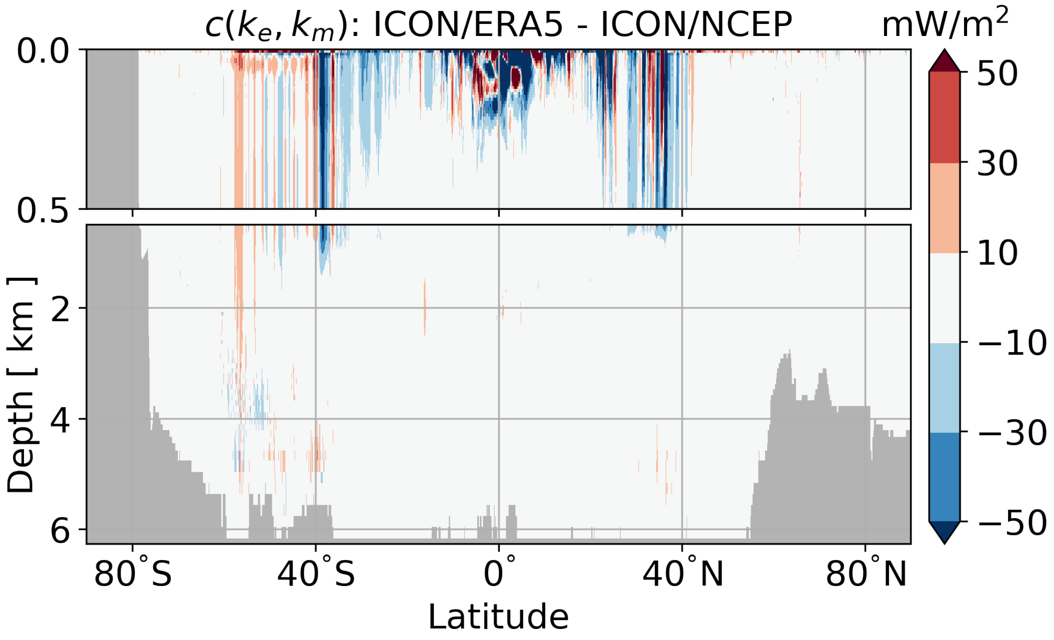

Figure 2.11: Differences in the conversion $c(k_e, k_m)$ between ICON/ERA5 and ICON/NCEP.

averaged k_e equator-ward of about 40° above roughly about 500 m (Fig.2.12b) could be the result of the stronger conversion $c(k_m, k_e)$ in ICON/ERA5 than in ICON/NCEP.

We consider now the largest forcing difference found in the generation of eddy kinetic energy $g(k_e)$, which amounts to nearly 1 TW when integrated globally. Fig.2.13 shows that $g(k_e)$ is almost everywhere stronger in ICON/ERA5 than in ICON/NCEP. The stronger generation is due to the stronger wind stress variability in ERA5 than in NCEP (Fig.2.1). It is however unclear how the higher variability in surface winds should systematically generate an enhanced eddy field (note that this requires a correlation between the wind fluctuations which typically occur on time scales of hours to days and the eddy field which acts on time scales of weeks to months). The more likely explanation is that the stronger wind fluctuations in ERA5 lead to an enhanced excitation of ageostrophic dynamics like inertial oscillations. Such enhanced excitation in ICON/ERA5 relative to ICON/NCEP is consistent with the systematic increase in the generation of near-inertial motions with increasing temporal resolution of the wind forcing found by Rimac et al., 2013.

According to Rimac et al., 2016, most of the excited inertial oscillations (about 90%) dissipate within the ocean's mixed layer. This could affect the fate of the nearly 1 TW stronger generation $G(K_e)$ due to the wind stress fluctuations in ERA5.

It will be interesting to see from future studies with higher resolution model configurations (e.g. resolving sub-mesoscale dynamics) and more energetically consistent parameterizations (e.g. allowing additional energy fluxes from k_e to either a parameterized internal wave or turbulent kinetic energy compartment) whether and

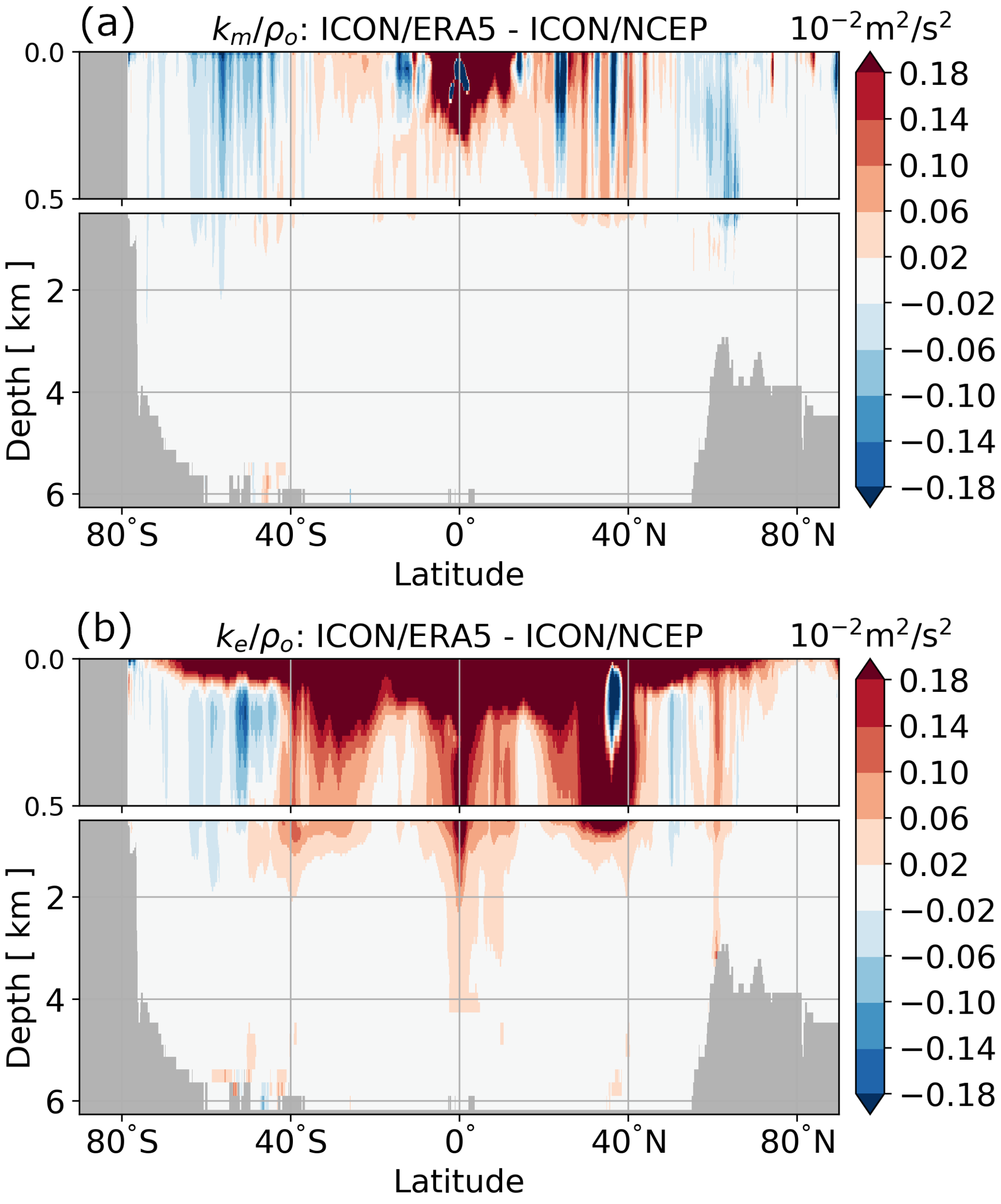

Figure 2.12: Differences in zonally averaged $k_m/\rho_\circ$ between ICON/ERA5 and ICON/NCEP (top) and in zonally averaged $k_e/\rho_\circ$ between ICON/ERA5 and ICON/NCEP (bottom).

how a feedback between the k_e compartment and the resolved circulation is established.

2.6 SUMMARY

In this paper, we investigate the sensitivity of the LEC to model difference and to forcing difference. The investigation due to model difference is based on two pairs

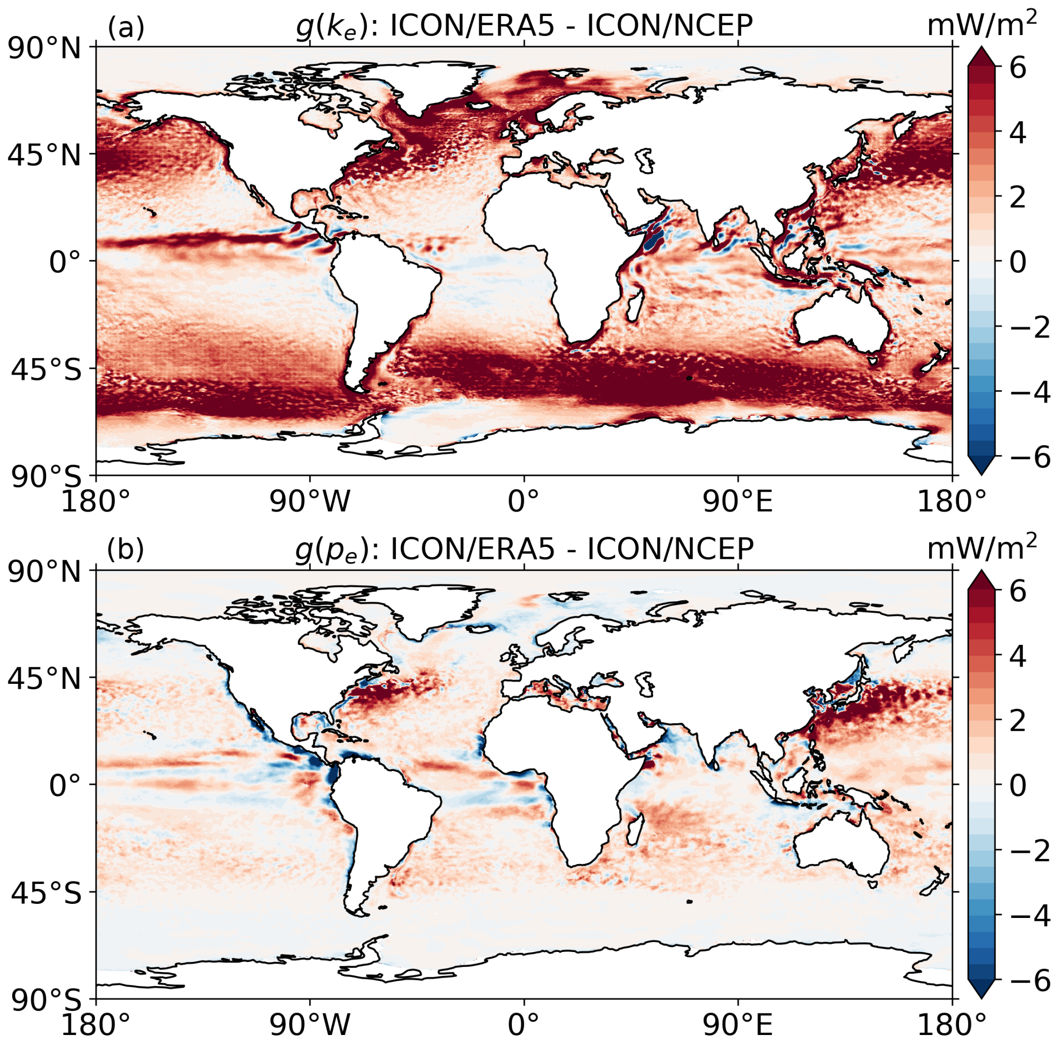

Figure 2.13: Differences in eddy kinetic energy generation g_{k_e} (top) and in eddy available potential energy generation $g(p_e)$ (bottom) between ICON/ERA5 and ICON/NCEP.

of ocean-only simulations at nominal O(10 km) resolution. The first pair consists of ICON/NCEP and MPIOM/NCEP, performed with two ocean general circulation models with completely different model architectures — MPI-OM and ICON-O — driven by the same surface forcing (NCEP). The second investigation due to forcing difference is based on the ICON/NCEP and ICON/ERA5 simulations, performed both with the same ocean model and configuration (namely ICON-O with 10 km resolution) but driven by surface fluxes obtained from two different reanalyses — NCEP and ERA5.

The first remarkable result which we obtain is the relative insensitivity of the energy conversions between the different compartments of the LEC — no matter whether we consider a forcing or a model difference. In particular, we note that not only the directions of the conversions stay the same but also the magnitudes of the LEC terms themselves as well as the overall spatial distributions of the conversion terms change little, no matter whether we consider the forcing or the model differences.

Despite these overall similarities, we also detect differences when comparing the underlying ICON-O to MPI-OM simulations. The first one concerns the baroclinic pathway that converts mean available potential energy p_m to eddy available potential energy p_e via $c(p_m, p_e)$ and further converts eddy available potential p_e to eddy kinetic energy k_e via $c(p_e, k_e)$. We find that the first transformation $c(p_m, p_e)$ is comparable in both simulations but the second $c(p_e, k_e)$ is considerably weaker in ICON. Consequently, there is enhanced dissipation of p_e in ICON/NCEP compared with MPIOM/NCEP. This might be related to the coarser resolution of the ICON-O configuration in the Southern Ocean where the resolution of 10 km only marginally resolves the first baroclinic Rossby radius. This probably leads to a too strong damping of the eddy kinetic energy field and to too strong diabatic mixing which reduces the eddy available potential energy.

The second difference concerns the conversion $c(k_m, k_e)$ in the deep ocean, which is in the opposite direction compared to the upper 2.5 km. This deep conversion, which is noticeably weaker and results in a larger global value of $C(K_m, K_e)$ in ICON/NCEP than in MPIOM/NCEP, is likely related to the weaker mesoscale eddies in ICON/NCEP which also most likely reduces the amount of energy transferred towards larger scales and therewith the mean circulation in the case of geostrophic turbulence.

The third difference concerns the conversion $c(p_m, k_m)$, which quantifies the generation of mean available potential energy in terms of wind-driven Ekman velocity. The $c(p_m, k_m)$ term is weaker in ICON/NCEP than in MPIOM/NCEP, due to weaker mean vertical velocity in ICON/NCEP than in MPIOM/NCEP.

The largest change among the terms of the LEC induced by forcing difference when comparing ICON/NCEP with ICON/ERA5 is the increase in the generation of eddy kinetic energy $g(k_e)$. Integrated globally, $G(K_e)$ is larger than all other generation terms. Using high-frequency ERA5 wind stress further increases $G(K_e)$ obtained from NCEP wind stress by about 1 TW. This enhanced generation is most likely balanced by an enhanced dissipation of eddy kinetic energy in the ocean's mixed layer, without having strong effects on the interior circulation. Note that in addition to the mesoscale eddy field, transient motions such as inertial oscillations are part of what we refer to as eddy dynamics (e.g. k_e but also $D(k_e)$ etc.).

The gross features of the LEC pictures the ocean as a "windmill" which transfers the forcing of the ocean by the winds into the circulation of the ocean (von Storch et al., 2012). The insensitivity of the LEC with respect to the enhanced high-frequent wind forcing ($G(k_e)$) indicates that this "windmill" is not able to effectively use this enhanced energy input for large scale currents. In this regard, it might be considered as an inefficient "windmill" regarding the large-scale circulation. On the other hand, it may become a more efficient "mixer" since the energy within the inertial oscillations and internal waves might ultimately lead to energy transfers from these compartments to small-scale turbulence. In parts, this is already reflected by the TKE scheme used in our ICON configurations where energy dissipated by vertical shear is transferred to turbulent kinetic energy. It will be interesting to observe to what degree such energy pathways change if simulations are performed at higher resolutions, such as those in which sub-mesoscale dynamics and a larger fraction of the internal wave field are resolved. Changes in the LEC may also be expected when more sophisticated parameterizations are used, such as those which enable consistent transfers between resolved and unresolved energy compartments.

3 ON THE EXCHANGE OF KINETIC ENERGY BETWEEN THE MEAN FLOW AND THE EDDIES

> *People should treat the oceans like we do anything else that we care about – with consideration, with care, and affection. That's it. For that we must educate*
>
> — Walter Munk

This Paper is in preparation: Ssebandeke, J., von Storch, J. S., & Brüggemann, N. (2023). On the exchange of kinetic energy between the mean flow and the eddies. Ocean Dynamics.

3.1 ABSTRACT

We evaluate how kinetic energy is exchanged between the eddies and the mean circulation following eddy-mean flow interactions using an eddy-rich, 10 km horizontal resolution, numerical simulation based on the ICON-O model. We show that the exchange of kinetic energy is nonlocal — nonlocality is most prominent in the Southern Ocean, western boundary currents and in the equatorial regions. Furthermore, we show that the exchange of energy is such that the mean flow loses energy in the surface layers, and most of the energy released by the mean flow is used for eddy growth, while the rest is transferred to the deeper ocean and then, together with the energy released by the eddies, it's transferred back to the mean flow.

3.2 INTRODUCTION

It is well established that kinetic energy of the mesoscale variability in the ocean is primarily generated through instabilities, represented as eddy-mean flow interactions in the Lorenz Energy Cycle framework, however, the way in which kinetic energy is gained by the eddies is not well characterised due to the nonlocal nature of the energy interactions and hence exchange (Harrison and Robinson, 1978; Chen et al., 2014; Murakami, 2011). Nonlocality in eddy-mean flow interactions originates when the energy extracted from the mean flow does not locally sustain energy-growth of eddies (or vice versa), but rather redistributed and consequently used to support energy-growth of eddies in remote regions. Quantifying the redistribution of energy following nonlocal interactions is not only crucial in understanding how oceanic energy, which is inputted at the surface, is transferred to the interior, but also relevant in improving parameterisation (Ivey and Imberger, 1991; Eden and Greatbatch, 2008; Marshall and Adcroft, 2010) — most of the parameterizations describe local effects of unresolved motions, but unresolved motions do not have only local effects. While the regional energy-redistribution following nonlocal interactions has increasingly been studied (Chen et al., 2014; Kang and Curchitser, 2015; Capó et al., 2019; Jamet et al., 2022; Matsuta and Masumoto, 2021; Bryden, 1982), the global redistribution has not been evaluated before.

Another aspect concerns the downward redistribution of energy by fluxes resulting from nonlocal interactions. Previous studies have mostly considered integrals over the full water-column depth (Chen et al., 2014; Kang and Curchitser, 2015) — this only outlines the contribution of the horizontal fluxes because the full water-column depth is closed in the vertical, and therefore vertical fluxes vanish. Jamet et al., 2022 highlighted the contribution of vertical fluxes resulting from nonlocal interactions, however, that study was limited to the sub-mesoscale regime. Here, we use a layer-wise consideration to quantify the downward redistribution of energy resulting from nonlocal eddy-mean flow interactions in the mesoscale regime. The rest of the article is organized as follows: section 3.3 presents the diagnostic framework, and section 3.4 presents the description of the model and numerical simulation. Results are presented in section 3.5. Lastly, a summary is presented in section 3.6.

3.3 DIAGNOSTIC FRAMEWORK

3.3.1 Budget of kinetic energy per unit volume

The equations for eddy kinetic energy, $k_e = \frac{1}{2}\rho_\circ\left(\overline{v'^2} + \overline{u'^2}\right)$ and mean kinetic energy, $k_m = \frac{1}{2}\rho_\circ\left(\overline{v}^2 + \overline{u}^2\right)$ can be written as (for details, see equation (A.8) and (A.15) in Appendix A; Olbers et al., 2012; von Storch et al., 2012):

$$\frac{\partial}{\partial t}k_e + \ldots = i_{ke} \tag{3.1}$$

$$\frac{\partial}{\partial t}k_m + \ldots = i_{km} \tag{3.2}$$

where $i_{k_e} = -\rho_\circ\left(\overline{\mathbf{u}_\mathrm{h}'v'}\cdot\nabla_\mathrm{h}\overline{v} + \overline{\mathbf{u}_\mathrm{h}'u'}\cdot\nabla_\mathrm{h}\overline{u}\right) - \rho_\circ\left(\overline{w'v'}\frac{\partial\overline{v}}{\partial z} + \overline{w'u'}\frac{\partial\overline{u}}{\partial z}\right)$. The former is the along-layer component and represents interactions that are limited to a particular layer. The latter component represents across-layer interactions. ∇_h represents the two dimensional gradient operator, $\mathbf{u}_\mathrm{h}$ is the two dimensional velocity with components (u, v) and $\rho_\circ$ is the reference density. The prime represents variations in time, while the overbar represents a time mean. i_{ke} represents the change of eddy kinetic energy due to the eddy-mean flow interaction. When this term is positive, it implies that eddy kinetic energy is intensified otherwise it's dissipated. $i_{k_m} = -\rho_\circ\left(\overline{v}\cdot\nabla_\mathrm{h}\overline{\mathbf{u}_\mathrm{h}'v'} + \overline{u}\cdot\nabla_\mathrm{h}\overline{\mathbf{u}_\mathrm{h}'u'}\right) - \rho_\circ\left(\overline{v}\frac{\partial}{\partial z}\overline{w'v'} + \overline{u}\frac{\partial}{\partial z}\overline{w'u'}\right)$. Similarly, the former component is the along-layer component while the latter is the across-layer component of the interaction term. i_{k_m} represents the change of mean kinetic energy due to eddy-mean flow interaction. If this term is negative, the mean flow is slowed down otherwise, it's intensified. i_{km} can further be decomposed[1]as:

$$
\begin{aligned}
i_{k_m} &= -\rho_\circ \left(\overline{v} \nabla \cdot \overline{\mathbf{u}' v'} + \overline{u} \nabla \cdot \overline{\mathbf{u}' u'} \right) \\
&= -\rho_\circ \nabla \cdot \left(\overline{u}\ \overline{u' \mathbf{u}'} + \overline{v}\ \overline{v' \mathbf{u}'} \right) + \rho_\circ \left(\overline{\mathbf{u}' v'} \cdot \nabla \overline{v} + \overline{\mathbf{u}' u'} \cdot \nabla \overline{u} \right) \\
&= i_k - i_{ke} \qquad (3.3)
\end{aligned}
$$

where $i_k = \nabla \cdot t_k$, $t_k = -\rho_\circ \left(\overline{u}\ \overline{u' \mathbf{u}'} + \overline{v}\ \overline{v' \mathbf{u}'} \right)$ is the energy flux per unit volume, with components: $t_k^x\ \hat{\mathbf{i}} + t_k^y\ \hat{\mathbf{j}} + t_k^z\ \hat{\mathbf{k}}$, $t_k^x = -\rho_\circ \left(\overline{u}\ \overline{u'u'} + \overline{v}\ \overline{v'u'} \right)$, $i_k^y = -\rho_\circ \left(\overline{u}\ \overline{u'v'} + \overline{v}\ \overline{v'v'} \right)$, $i_k^z = -\rho_\circ \left(\overline{u}\ \overline{u'w'} + \overline{v}\ \overline{v'w'} \right)$

$$
\Rightarrow \frac{\partial}{\partial t} k_m + \ldots = i_k - i_{ke} \qquad (3.4)
$$

Notice that i_{ke} appears in equation 3.1 and 3.4, but with opposite signs, and therefore represents exchange of energy between mean kinetic energy and eddy kinetic energy. Note that, equation (3.3) could as well be used in equation (3.1), to replace i_{k_e} with $i_{k_m} + i_k$. This implies that in the case of non-vanishing flux divergence, i_k the exchange between eddy and mean kinetic energy is not necessarily local but e.g. energy extracted from the eddies could be transferred horizontally or vertically instead of being directly transferred to the mean flow or vice versa. i_k represents the nonlocal redistribution of energy. For closed regions, like the global ocean, i_k vanishes. This implies that, i_{k_e} acts as an energy conversion term. For regions with open boundaries, i_k can either vanish or not. Regions where i_k vanishes undergo local energy exchange, otherwise the energy exchange is nonlocal. The equation for total kinetic energy, k can be obtained by summing the equation for eddy kinetic energy (equation (3.1)) and that of mean kinetic energy (equation (3.2)). i.e. $k = k_e + k_m$

$$
\frac{\partial}{\partial t} k + \ldots = i_k \qquad (3.5)
$$

We observe that i_k appears in the equation for total kinetic and therefore modifies the total kinetic energy. Where this term is negative, total kinetic energy is reduced otherwise it's intensified. A similar derivation has been presented in Chen et al., 2014; Harrison and Robinson, 1978.

---

[1] We use the following identity in the decomposition of i_{km}. For a vector $\mathbf{A}$ and scalar ψ, $\nabla \cdot (\psi \mathbf{A}) = \psi \nabla \cdot \mathbf{A} + \mathbf{A} \cdot \nabla \psi$

3.3.2 Budget of kinetic energy integrated over a volume

When equation (3.5) is integrated over a volume, V enclosed by a closed-surface, S we obtain

$$\begin{aligned}\frac{\partial}{\partial}\iiint_V k\,\mathrm{d}V + \ldots = I_k &= \iiint_V i_k\,\mathrm{d}V = \iiint_V \nabla\cdot t_k\,\mathrm{d}V \\ &= -\rho_\circ \iiint_V \nabla\cdot\Big(\,\overline{u}\;\overline{u'\mathbf{u'}} + \overline{v}\;\overline{v'\mathbf{u'}}\,\Big)\,\mathrm{d}V \\ &= -\rho_\circ \oint_S \Big(\,\overline{u}\;\overline{u'\mathbf{u'}} + \overline{v}\;\overline{v'\mathbf{u'}}\,\Big)\cdot\hat{n}\,\mathrm{d}S \qquad (3.6)\end{aligned}$$

Based on Gauss's theorem, the volume integral over the flux divergence can be decomposed into fluxes perpendicular to the bounding surfaces of that volume. Here, we assume the volume is a box with boundaries along constant depth, constant latitude and constant longitude. Here, we focus on two cases:

Case I: Global layered ocean. Here, we consider the total ocean area. In this consideration the horizontal components of equation 3.6 vanish.

Case II: Latitudinal bands. Here, we consider zonal bands that are open in the vertical and in the meridional direction but closed in the zonal direction.

The notation is such that small letters represent interaction terms per unit volume while capital letters represent the interaction terms integrated over a volume i.e.

$$I_k = \iiint_V i_k\,\mathrm{d}V, \qquad I_{k_e} = \iiint_V i_{k_e}\,\mathrm{d}V, \qquad I_{k_m} = \iiint_V i_{k_m}\,\mathrm{d}V$$

3.4 NUMERICAL SIMULATION

We use the ICON-O model — a primitive equation model, which has an unstructured horizontal grid, with a C-type staggering of variables (Korn, 2017). The fidelity of ICON-O in simulating key features of global ocean dynamics and energetics is documented in Korn et al., 2022; Ssebandeke et al., 2023. The model configuration used in this study has a horizontal resolution of about 10 km and 128 z-levels with thicknesses varying from 8 to 200 m.

As initial conditions, we used data from the Ocean ReAnalysis System 5 (ORAS5) reanalysis dataset – ORAS5 is the latest ocean reanalysis dataset produced by the ECMWF and has a horizontal resolution of 25 km, and 75 vertical levels (Zuo et al., 2019). We interpolated salinity and temperature for January 2010 from the ORAS5 reanalysis dataset onto the ICON-O grid and then forced the model with ERA5 forcing (Hersbach et al., 2020). We then allow the system to evolve for 10 years – 2010 to 2020. Fig 3.1 shows the total kinetic energy from the starting time, January 2010 to the end, January 2020. Within the first year, the monthly mean kinetic energy reaches a stable state and oscillates around 3×10^{-3}J for the following years. Only the last 5

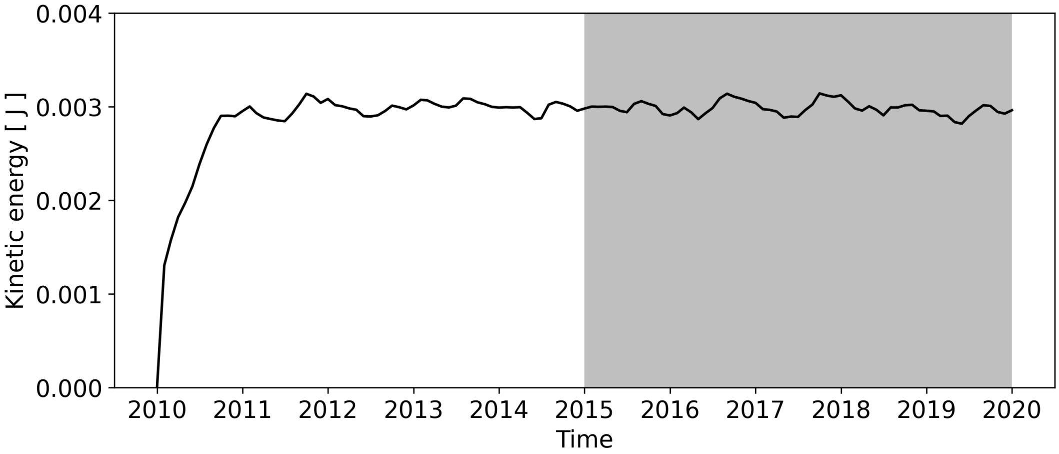

Figure 3.1: Time series of the monthly-mean global kinetic energy derived from our ICON-O simulation with 10 km horizontal grid spacing. The grey shaded area shows the study period, 2015 - 2020

years of the simulation, 2015-2020 are analysed.

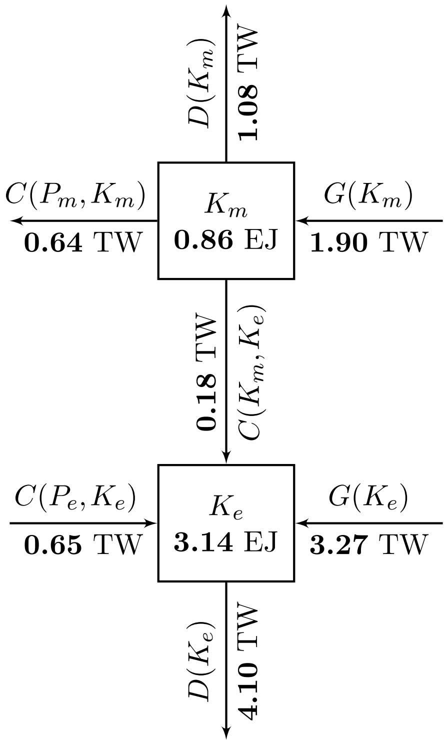

Figure 3.2: Kinetic energy branch of the Lorenz Energy Cycle. The energy reservoirs are in exa-joules (EJ, 10^{18}). The generation, exchange and dissipation terms are in tera-watts (TW, 10^{12}).

We evaluate the numerical simulation by comparing the kinetic energy branch of the Lorenz Energy Cycle derived from the simulation here to that derived from ICON/NCEP (see figure 3 in Ssebandeke et al., 2023). Some of the main differences between the simulations are related to (1) the averaging period in Ssebandeke et al., 2023 is 10 years compared to 5 years used here, surface fluxes in ICON/NCEP are derived from NCEP reanalysis, instead of ERA5 as used here and lastly, (3) ICON/NCEP was initially spun-up for 25 years and NCEP forcing was applied from 1948 to 2010. This is a much longer spin-up compared to the 5 years used here. This can lead to fundamental differences in circulation and stratification which then might also affect the energy cycle. Regardless of these differences, the overall magnitude, direction of energy pathways, and horizontal structure of the different terms of the LEC are consistent in both estimates of the Lorenz energy cycle. For this work, we concentrate on the eddy-mean flow interaction split into the single contributions as discussed in section 3.3 ($c(k_e, k_m) = -i_{k_e} = i_{k_m} - i_k$). For the sake of comparing the results from this simulation with those from the ICON/NCEP simulation in Ssebandeke et al., 2023, the reader is referred to compare Fig. 3.5 and 3.4 (b) of this study, with Fig. 7 (b) and 8 from Ssebandeke et al., 2023. Here, we only note that overall, the results are relatively similar. The largest values are located in the surface layers. Above 2.7 km, the values are mostly positive representing a transfer from mean kinetic energy to eddy kinetic energy. In the deeper layers, the transfer is directed from eddies to the mean flow. The global integral of the conversion in ICON/NCEP, (-0.17 TW) is only slightly weaker than that observed in the simulation (-0.18 TW) used here (figure 3.2). The difference appears to be caused by excessive gain of energy by eddies in the surface layer in this simulation.

3.5 RESULTS

3.5.1 Non-local energy exchange

Figure 3.3 (a) and (b) shows the horizontal distribution of the energy interaction terms — i_{k_e}, and i_{k_m} — at 96 m. The other levels have a similar spatial structure — the largest values are observed along strong major mean currents, in the southern ocean, western boundaries and in the equatorial regions. Note that i_k is not zero (Fig. 3.3 (c)) which implies that there are notable differences between i_{k_m} and i_{k_e}. The difference in magnitude of the values of i_{k_e} and i_{k_m}, which can, for instance, be seen in the Southern Ocean represent nonlocal energy exchange. Nonlocality in the Pacific sector and Indian Ocean sector of the Southern Ocean has been reported in Chen et al., 2014. However, Chen et al., 2014 observed locality in the Atlantic sector (see figure 7 in Chen et al., 2014), but we observe nonlocality in this sector of the southern ocean.

An outstanding challenge in the interpretation of the interaction terms concerns the abrupt change in sign of the interaction terms — positive and negative values are situated right next to each other (see also Loose et al., 2023). To circumvent this impediment, we diagnose the depth-latitude cross-section. Figure 3.4 shows the depth-latitude cross-section of section Q in figure 3.3, and that of the global ocean. We observe in figure 3.4 (a) that absolute values of $|i_{k_e}|$, greater than 160×10^{-6} Wm^{-3} are only located between 50°S and 52°S, else where the values are less than 80×10^{-6} Wm^{-3}. In contrast, the absolute values for $|i_{k_m}|$ and $|i_k|$ larger than 160×10^{-6} Wm^{-3}

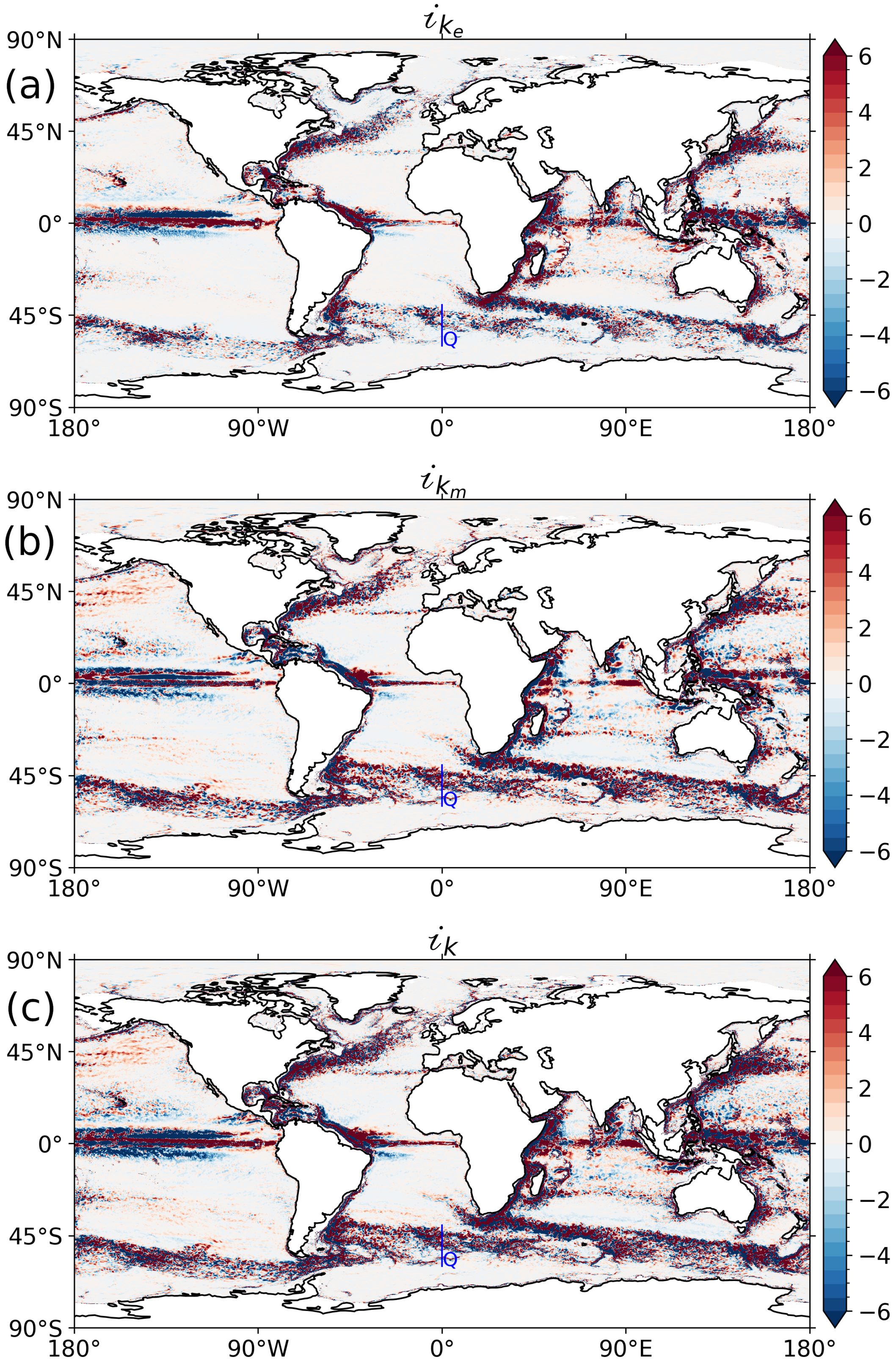

Figure 3.3: Horizontal distribution of (a) i_{k_e}, (b) i_{k_m} and (c) i_k at 96 m. Units: 1×10^{-6} Wm^{-3}. The depth-latitude cross section of line, Q is shown in figure 3.4.

are observed at various locations within the region (figure 3.4 (c) & (e)). This clearly shows that nonlocality plays a crucial role in regional dynamics. It should however, be noted that i_{k_e}, i_{k_m} and i_k have different structures in other regions of the global ocean — there are various forms of interactions as noted by Murakami, 2011. The right column of Fig. 3.4 shows that when integrated over a latitudinal band of each layer, there is by and large a compensation between i_{k_e} and i_{k_m}. The left column shows that without integration, i_{k_e} can be much weaker than i_{k_m}. This is consistent with $i_{k_m} = i_k$ - i_{k_e}. The pattern for i_{k_m} (figure 3.4 (d)) is similar to that of i_{k_e} (figure 3.4 (b)), but with reverse signs and hence portrays exchange of energy between mean kinetic energy and eddy kinetic energy.

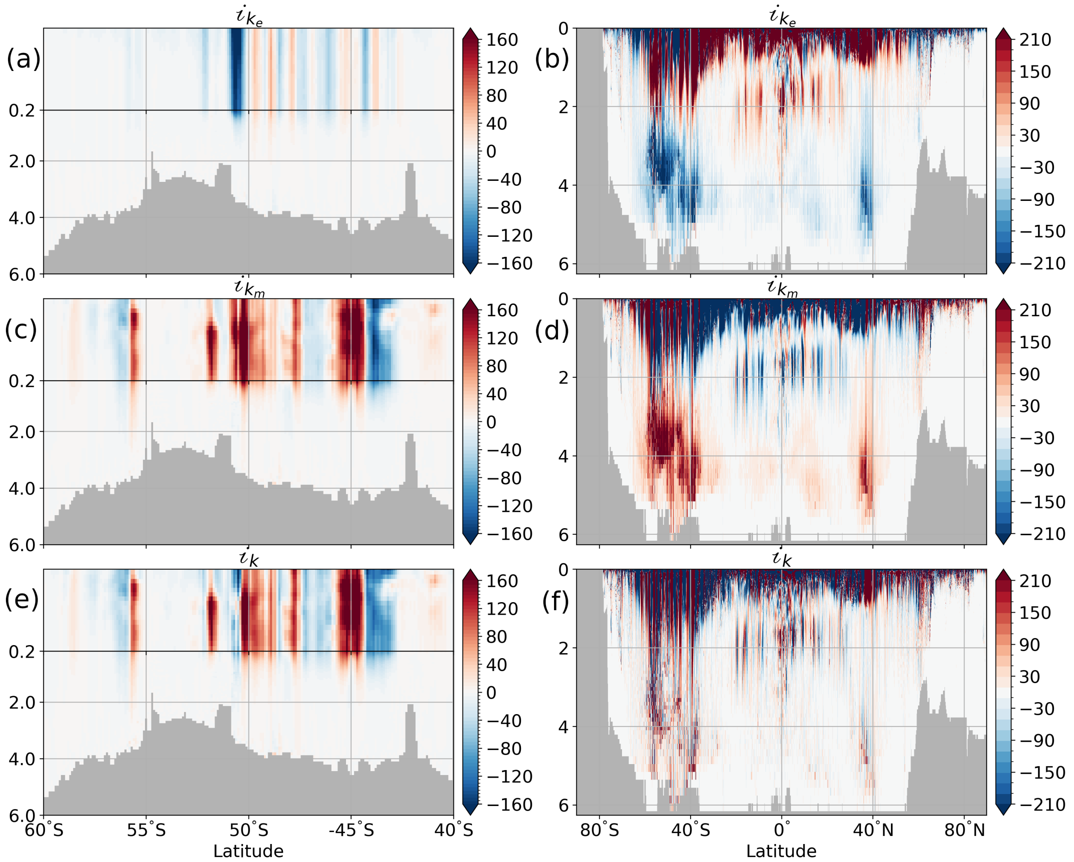

Figure 3.4: Depth-latitude cross-section along the line Q in figure 3.3 (a) i_{k_e}, (c) i_{k_m} and (e) i_k. Global depth-latitude zonal integral of (b) i_{k_e}, (d) i_{k_m} and (f) i_k. Units 1×10^{-6} Wm^{-3}.

Figure 3.5 shows the vertical profiles of I_k, I_{k_m} and I_{k_e}. The conversion is dominated by I_{k_m} and I_{k_e} — generally I_{k_m} and I_{k_e} are higher than I_k by a factor of about 3. However, since I_k is nonzero it means the conversion is not totally local — I_k represents the vertical rate of transfer of kinetic energy. The profile for I_k is negative in the upper about 200 m, below this layer the profile is positive. The largest value of I_k, -0.14×10^{10} W is about 25% of the corresponding value for I_{k_e}. Above 2.7 km, I_{k_m} is negative, and I_{k_e} is positive. This implies that, above 2.7 km, the mean flow loses kinetic energy and the eddy kinetic energy is intensified. Below 2.7 km, I_{k_m} is positive and I_{k_e} is negative. This implies that the mean circulation is intensified while eddy kinetic energy becomes weaker — similar to what is observed in the atmosphere (Li et al., 2007).

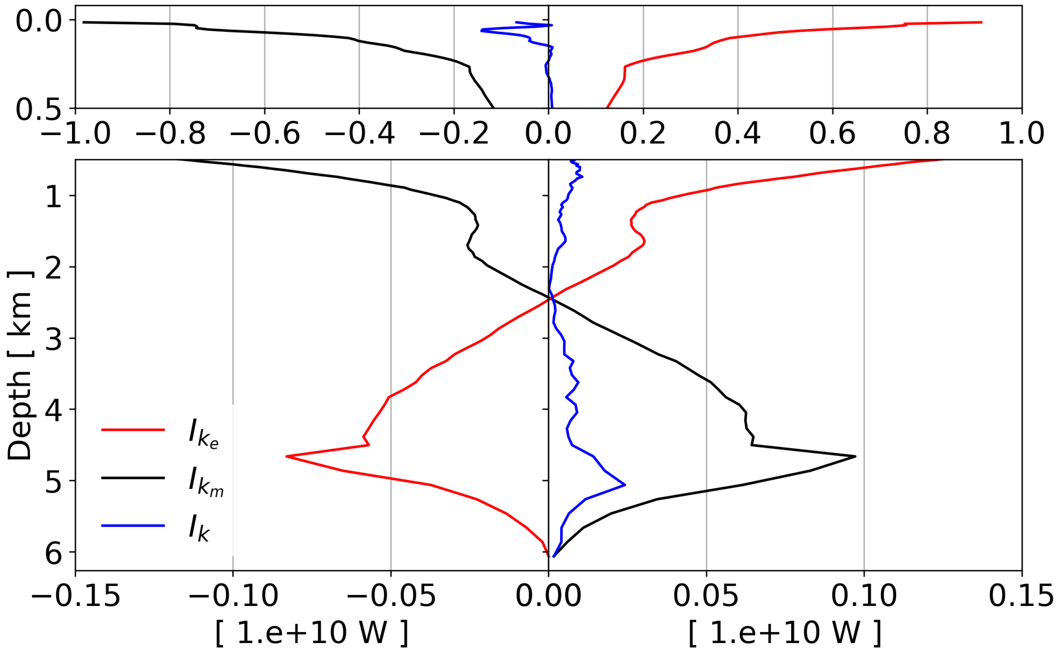

Figure 3.5: Vertical profiles (integral over a global horizontal layer of depth, dz) of I_k, I_{k_m} and I_{k_e}

3.5.2 Vertical redistribution of energy

In this section, we concentrate on the redistribution of energy given by I_k (nonlocal term, i_k integrated over a volume). Following **case II** (see classification in section 3.3.2), we analysed the latitudinal redistribution of energy; this includes both meridional and vertical redistribution of energy. The latitudinal energy redistribution shows three key regions where nonlocality is prominent: the Southern Ocean, equatorial Ocean and western boundaries (not shown). The subtropics and polar regions are mostly local. Outside the Southern Ocean, nonlocality is limited to the upper 500 meters. In the Atlantic basin, nonlocality is only prominent in the Gulf Stream latitudinal band — the tropical Atlantic experiences local interactions. In contrast, equatorial regions in both the Indian and Pacific Ocean basin are nonlocal. In the Pacific, furthermore, nonlocality is also observed in the Kuroshio latitudinal band. This is re-affirms results from Chen et al., 2014. In that article, prominence of nonlocality was found in the Kuroshio, Gulf Stream, Pacific and Indian Ocean sectors of the southern ocean. The subtropical gyres were found to be local. This is also in line with several other regional studies (Kang and Curchitser, 2015; Matsuta and Masumoto, 2021). As mentioned in section 3.2, most of the previous studies emphasised the horizontal redistribution of energy. Here, we compare the horizontal redistribution, and vertical redistribution of kinetic energy following nonlocal interactions. Figure 3.6 shows the ratio of the magnitude of vertical energy flux to the magnitude of horizontal energy flux $\frac{|t_k^z|}{|t_k^x+t_k^y|}$ in the Southern Ocean. We concentrate on the southern Ocean because most of the activity regarding the interaction is located in the southern ocean (see figure 3.4), however, the spatial pattern (of the ratio) in the western boundary regions is similar to that observed in the Southern Ocean. Horizontal redistribution dominates vertical redistribution along strong mean currents. Away from strong mean currents, vertical redistribution of energy tends to dominate the total energy redistribution.

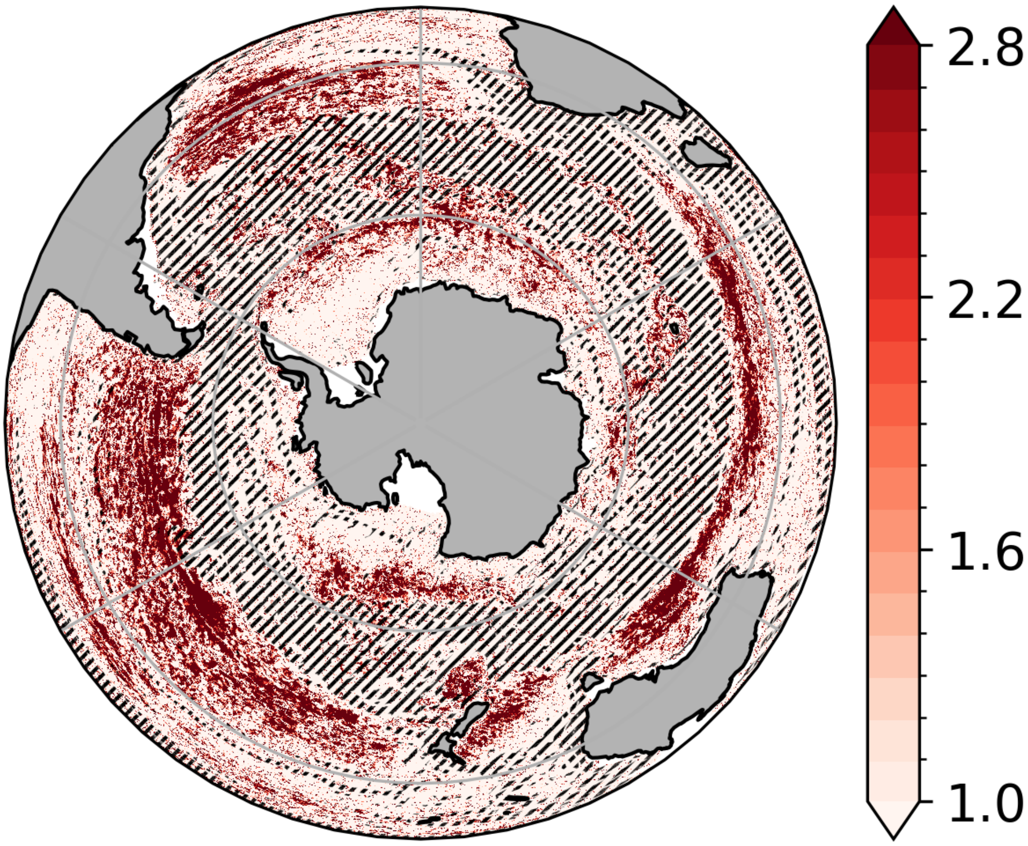

Figure 3.6: Ratio of the magnitude of vertical energy flux to the magnitude of horizontal energy flux, $\frac{|t_k^z|}{|t_k^x+t_k^y|}$ at 96m in the Southern Ocean. Values greater than 1 show regions where vertical redistribution is greater than horizontal redistribution. Hatches show regions where $log_{10}\left\{0.5(\overline{u}^2+\overline{v}^2)\right\} > -3$

To understand how energy is vertically redistributed, we diagnose the vertical energy flux, per unit volume t_k^z. For simplicity, we only analyse $\overline{u}\;\overline{u'w'} + \overline{v}\;\overline{v'w'}$, since we are only interested in the direction of propagation, not the magnitudes. The largest values are located in the equatorial region (not shown). In the mid-latitudes, the values are negative and represent a downward propagation of energy. In the subtropics the values are positive, indicating an upward transfer of the energy (figure 3.7(a)). Large values in the mid-latitudes, over -5×10^{-6} m^3/s^3, extend below about 2 km, however, values with similar magnitudes are limited to the upper 1km in the subtropics. The difference in the direction of the energy propagation between the mid-latitudes and subtropics appears to be related to the mismatch in depth at which excess energy is released by the mean flow. In the mid-latitudes — in the upper 100m — the mean flow releases more energy (figure 3.7 (b)) than the eddies take up (figure 3.7 (c)). The redundant

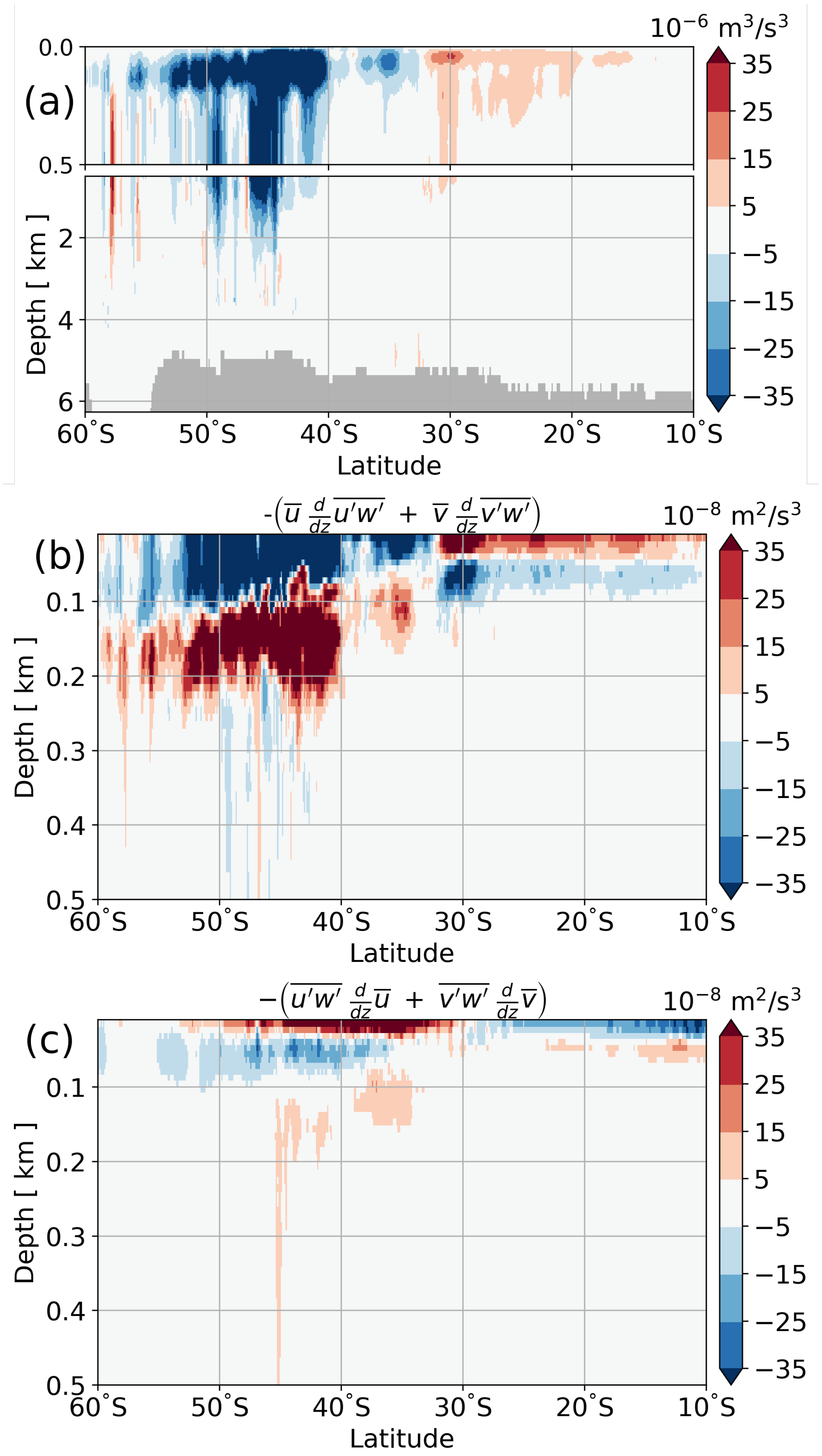

Figure 3.7: (a) $\overline{u}\ \overline{u'w'} + \overline{v}\ \overline{v'w'}$. Positive values indicate upward orientation, otherwise it's downward. (b) vertical component of the $i_{k_m}/\rho_\circ$ (c) vertical component of the $i_{k_e}/\rho_\circ$ in the South-Atlantic (10° S - 60° S, 30° W - 10° E).

excess energy is then transported downwards and used to intensify the mean flow in the subsurface. Equator-ward of about 35 °S, the excess release of energy by the mean flow is situated below the surface and therefore necessitates an upward transport of energy.

3.6 SUMMARY

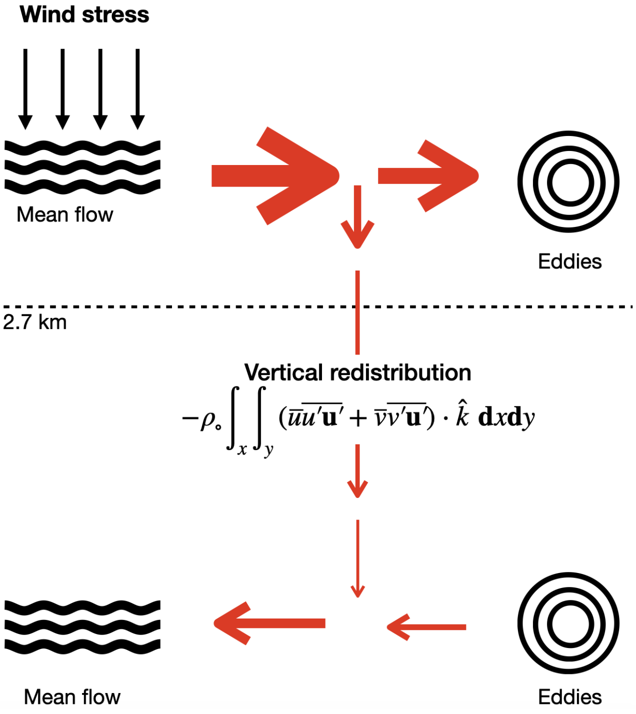

Figure 3.8: Summary of how kinetic energy is exchanged between the mean flow and the eddies

In this study, we have established how kinetic energy is exchanged between the eddies and the mean flow. We have shown that this exchange, on a regional basis, is nonlocal — nonlocality is an essential source of energy especially in the eddy-rich regions like the Southern Ocean and in the western boundaries. This is conforming with the previous regional studies (Chen et al., 2014; Kang and Curchitser, 2015; Matsuta and Masumoto, 2021). The global exchange is nearly local; the mean flow loses energy in the surface layers, and most of the energy released by the mean flow is used for eddy growth, while the rest is transferred to the deeper ocean and then, together with the energy released by the eddies, it's transferred back to the mean flow. This exchange is summarised in figure 3.8. Regarding the nature of vertical redistribution of energy, we observed that redistribution of energy is oriented downward in the mid-latitudes and upward in the subtropics. This mismatch in the direction of the energy redistribution is related to the position of excess energy. In the mid-latitudes, excess energy is located in the surface layers and in the subtropics, excess energy is located at a deeper layer. Therefore to reconcile the difference in the location of excess energy, the energy is transported downwards in the mid-latitudes but upwards in the subtropics.

4 A BRIEF NOTE ON THE SENSITIVITY OF KINETIC-ENERGY EXCHANGE TO TOPOGRAPHIC FORCING

> *Shall I refuse my dinner because I do not fully understand the process of digestion?*
>
> — Oliver Heaviside

Here, I present some brief but interesting results which may lay the foundation for further research.

4.1 ABSTRACT

We assess the sensitivity of the gross features of eddy-mean flow interaction, $C(K_e, K_m)$ to topographic forcing in a complex OGCM. We do so through a series of sensitivity experiments; the series of experiments comprise two simulations that differ only by the configuration of the used topography — **topo_10km**, with 10 km resolution of bottom-topography, and **topo_160km**, with 160 km resolution of bottom-topography. The forcing, horizontal resolution and other model parameters are similar in both simulations. We observe that the mean circulation and transient eddies are notably sensitive to the variations in topography. In the simulation with smoother topography, the flow has increased kinetic energy. We have established that contrary to what is observed in the idealised 2-layer model, the gross features of the kinetic energy exchange in a complex OGCM are insensitive to topographic variations.

4.2 INTRODUCTION

As mentioned in section 1.1.1.2, the exchange of kinetic energy between the mean flow and the transient eddies, $C(K_e, K_m)$ is given by

$$C(K_e, K_m) = \int_V \rho_\circ \left(\overline{\mathbf{u}'v'} \cdot \nabla \overline{v} + \overline{\mathbf{u}'u'} \cdot \nabla \overline{u} \right) \, \mathrm{d}V$$

where $\int_V \mathrm{d}V$ indicates the integral over the volume of the ocean, $\mathbf{u}$ is the three dimensional velocity with components (u, v, w), ∇ is the three dimensional gradient operator, $\rho_\circ$ is the reference density. The overbar indicates a time-mean and the prime represents deviations from the time-mean.

In the atmosphere, the exchange of kinetic energy, $C(K_e, K_m)$ is directed from the eddies towards the mean circulation and this is thought to represent an upscale transfer of energy (figure 1.2). However, in the ocean, the transfer is reversed; mean kinetic energy is converted into eddy kinetic energy (figure 1.3). It's unclear why energy conversion in the ocean is opposite to that in the atmosphere. A more plausible way of thinking is that this is related to the fact that the two systems are forced differently, the atmosphere is driven by differential forcing while the ocean is mainly driven by wind forcing and tides. The wind forcing in the ocean drives mean currents and then through barotropic and baroclinic instability, energy is transferred to the eddies. Regarding integrated net direction of the kinetic energy transfer between mean and eddy flow, one might conclude that barotropic instability overwhelms other processes like the inverse cascade that would transfer the energy from small scales (eddies) to the large-scale circulation.

Table 4.1: Comparison of simulations used in Witter and Chelton, 1998 and in this study. **Cases 1**, **3** and **6** are idealistic simulations from Witter and Chelton, 1998. **topo__10km** and **topo__10km** are simulations performed using ICON-O model with 10 km horizontal resolution. Bottom topography used in ICON-O is obtained from SRMT30 (Cowan and Cooper, 2005)

Simulation	Resolution (Time period)	Forcing	Topography
Case 1	20 km (5 - 7200 days)	Steady, zonal jet $\tau_\circ \sin^2(\pi y/L_y)$ $\tau_\circ = 0.025\ \mathrm{Nm}^{-2}$ $L_y = 1200$ km	zonally uniform ridge (400 m tall, 800 km wide)
Case 3			zonal modulation of the ridge height in case 1
Case 6			zonal modulation of the ridge height and width in case 1
topo__10km	10 km (5 min - 5 years)	ERA5	SRTM30 topography at 10 km resolution
topo__160km			SRTM30 topography at 160 km resolution

However, with an idealized ocean model configuration — 2-layer, wind-forced quasi-geostrophic channel model — Witter and Chelton, 1998 used a series of three sensitivity experiments (**case 1**, **3**, & **6**) summarised in table 4.1 with variations in bottom topography (see figure 2 in Witter and Chelton, 1998 for details regarding topographic variations), and showed that reverse direction of the energy transfer in the ocean is related to bottom topography (figure 4.1). In **case 1**, with a zonally uniform ridge, the conversion is positive in both layers — energy conversion is directed from eddy kinetic energy to mean kinetic energy. In **cases 3** & **6**, where the ridge is modulated, the conversion is positive in the deeper layer but negative in the upper layer. This is similar to what is observed in the complex OGCM (figure 1.3). It is unclear if the sensitivities observed in the idealistic simulations will be observed in more complex OGCMs as well.

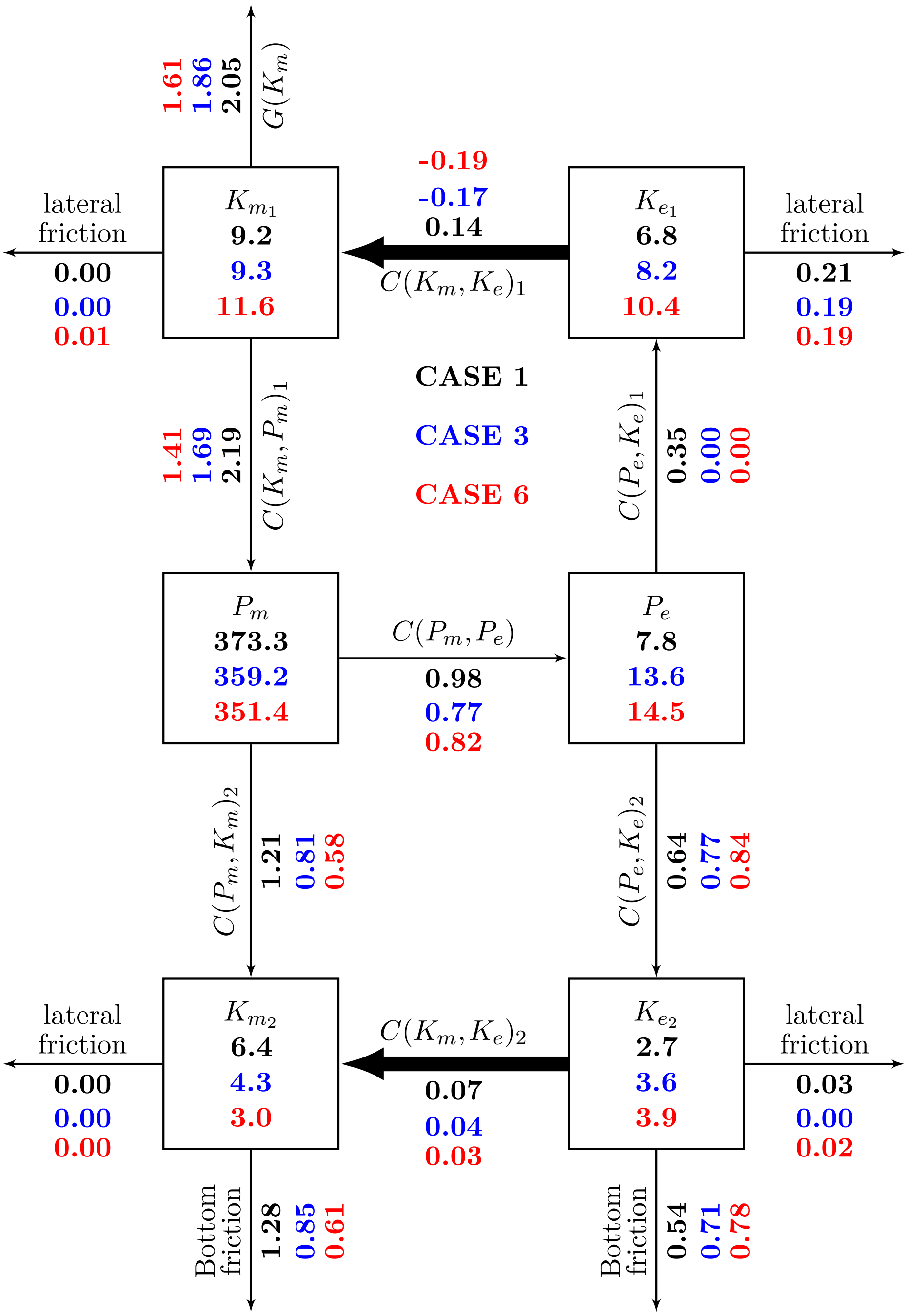

Figure 4.1: Energy cycle for **cases 1**, **3** & **6** (adapted from Witter and Chelton, 1998). The units for the energies are m^3/s^2, rounded to the nearest unit. Those for the transfer rates are 10^{-5} m^3/s^3, rounded to the nearest 0.1 unit. The definitions of the different terms is available in McWilliams et al., 1978. The subscripts $_{1,\&2}$ represent the model layers, 1 & 2 respectively.

4.3 METHODS

To study the sensitivity of the energy exchange with respect to bottom topography, replaced the bottom topography in the model setup used in chapter 3, with smoother bottom topography— modified SRMT30 topography (Cowan and Cooper, 2005) at 160 km (derived from the *R*2*B*4 configuration of ICON-O), and run the model over a period of 10 years, 2010 - 2020. Analogous to the simulation in chapter 3, within the first year, the monthly-mean kinetic energy reaches a stable state and oscillates around 3.4×10^{-3} J for the following years (not shown). Hereafter, the simulation performed in chapter 3 with 10 km resolution modified SRMT30 topography (derived from the ICON-O *R*2*B*8 configuration) is referred to as the **topo_10km** simulation. The new simulation with smoother topography (160 km) is referred to as **topo_160km**. The bottom topography and the resulting circulation in the Kuroshio region are shown in figure 4.2. Effects of topographic steering can be seen — in the **topo_10km** version the mean current continuously flows along the coast. In contrast, the current is detached from the coast at about 37.5°N in the **topo_160km** version.

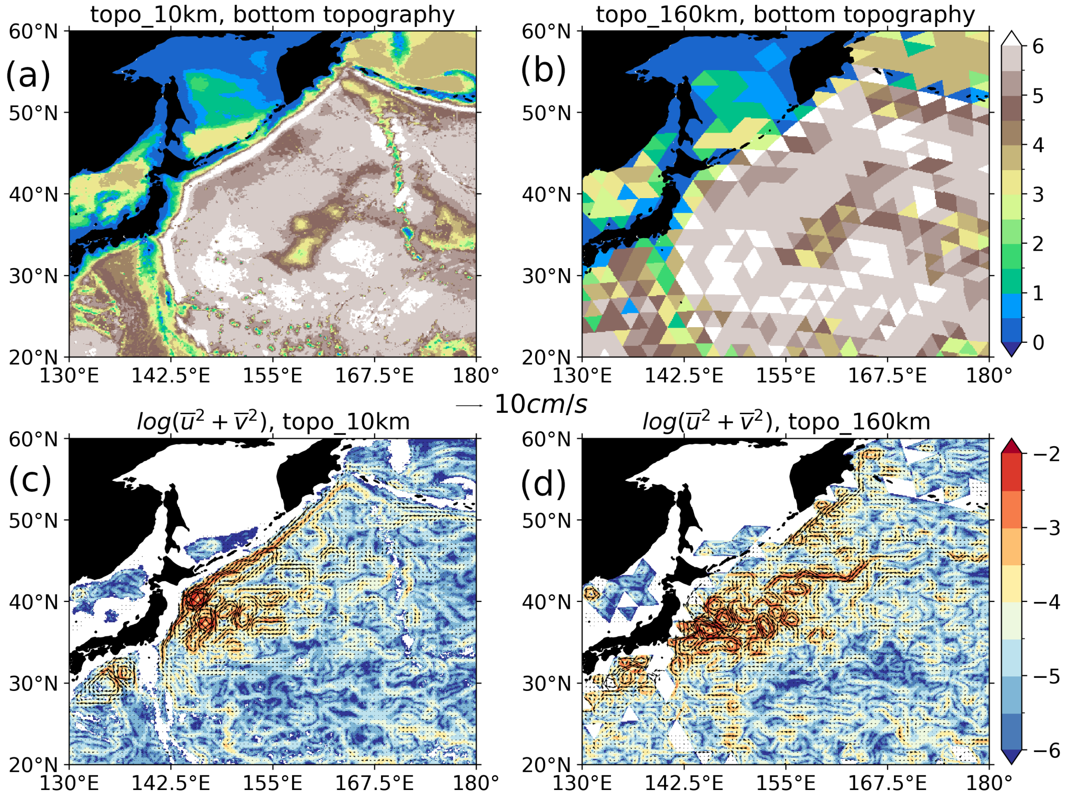

Figure 4.2: (a) **topo_10km** bottom topography (b) **topo_160km** bottom topography in kilometers. Bottom topography is derived from the modified SRTM30 (Cowan and Cooper, 2005). (c) mean kinetic energy for the **topo_10km** simulation and (d) mean kinetic energy for the **topo_160km** simulation at 1983 m. Arrows show the direction of flow. Units in m^2/s^2.

4.4 RESULTS

4.4.1 Sensitivity of kinetic energy to topographic forcing

Figure 4.3 (a) & (b) shows the horizontal distribution of mean kinetic energy in the **topo__160km** and **topo__10km** configuration respectively. In both configurations, kinetic energy is concentrated in sharp boundary currents and filaments in the Southern Ocean. However, the mean currents are more intense in the **topo__160km** configuration, especially in the Southern Ocean. For example, values of $u^2 + v^2 > 0.01m^2/s^2$ are observed in the Drake Passage area in the **topo__160km** configuration. The corresponding values in the **topo__10km** configuration are generally weaker than $0.01m^2/s^2$. Similarly, the horizontal distribution of eddy kinetic energy in the two configurations is notably different — **topo__160km** has stronger eddy kinetic energy, especially in the Southern Ocean (figure 4.3 (c) & (d)). Figure 4.4 (a) shows the horizontally integrated profiles of mean kinetic energy (solid curve) and eddy kinetic energy (dashed curve) in the two configurations. Above about 1 km, the energies are comparable. Below about 1 km, the profiles for **topo__160km** are stronger than those of **topo__10km**. The largest difference of the energy compartments can be found for eddy kinetic energy which amounts 3.46 EJ for **topo__160km** once globally integrated and therewith exceeds the value for **topo__10km** by 0.32EJ. The corresponding global integrals of mean kinetic energy are 0.95 EJ for **topo__160km** and 0.86 EJ in **topo__10km** the configuration. Overall, **topo__160km** is more energetic than **topo__10km**. This is expected since **topo__10km** has a more rough bottom topography — rough bottom topography is associated with enhanced dissipation (Feddersen et al., 2003; Yang et al., 2021; Trossman et al., 2017).

4.4.2 Sensitivity of the gross features of $C(K_e, K_m)$ to topographic forcing

There are two main gross features of $C(K_e, K_m)$ for the global ocean: (1) the global integral of $C(K_e, K_m)$ is negative — overall, kinetic energy exchange is directed from mean kinetic energy to the eddy kinetic energy. This is contrary to what is observed in the atmosphere — overall, in the atmosphere, the kinetic energy exchange is directed from eddy kinetic energy to the mean kinetic energy (Li et al., 2007). (2) The exchange is mainly negative above 2.7 km, but positive below (see figure 4.5 & 4.4 (b)). We observe that the spatial pattern $C(K_e, K_m)$ is similar in both configurations — $C(K_e, K_m)$ is mostly negative in the upper about 2.7 km and positive below. However, there are notable differences in the magnitudes of the $C(K_e, K_m)$ in the two configurations especially in the Southern Ocean (figure 4.4 (c)). The global integral of $C(K_e, K_m)$ in both configurations is negative — -0.18 TW in **topo__10km** and -0.16 TW in **topo__160km**. Overall, the inherent nature of the conversion remains unchanged, only subtle changes in magnitude are observed.

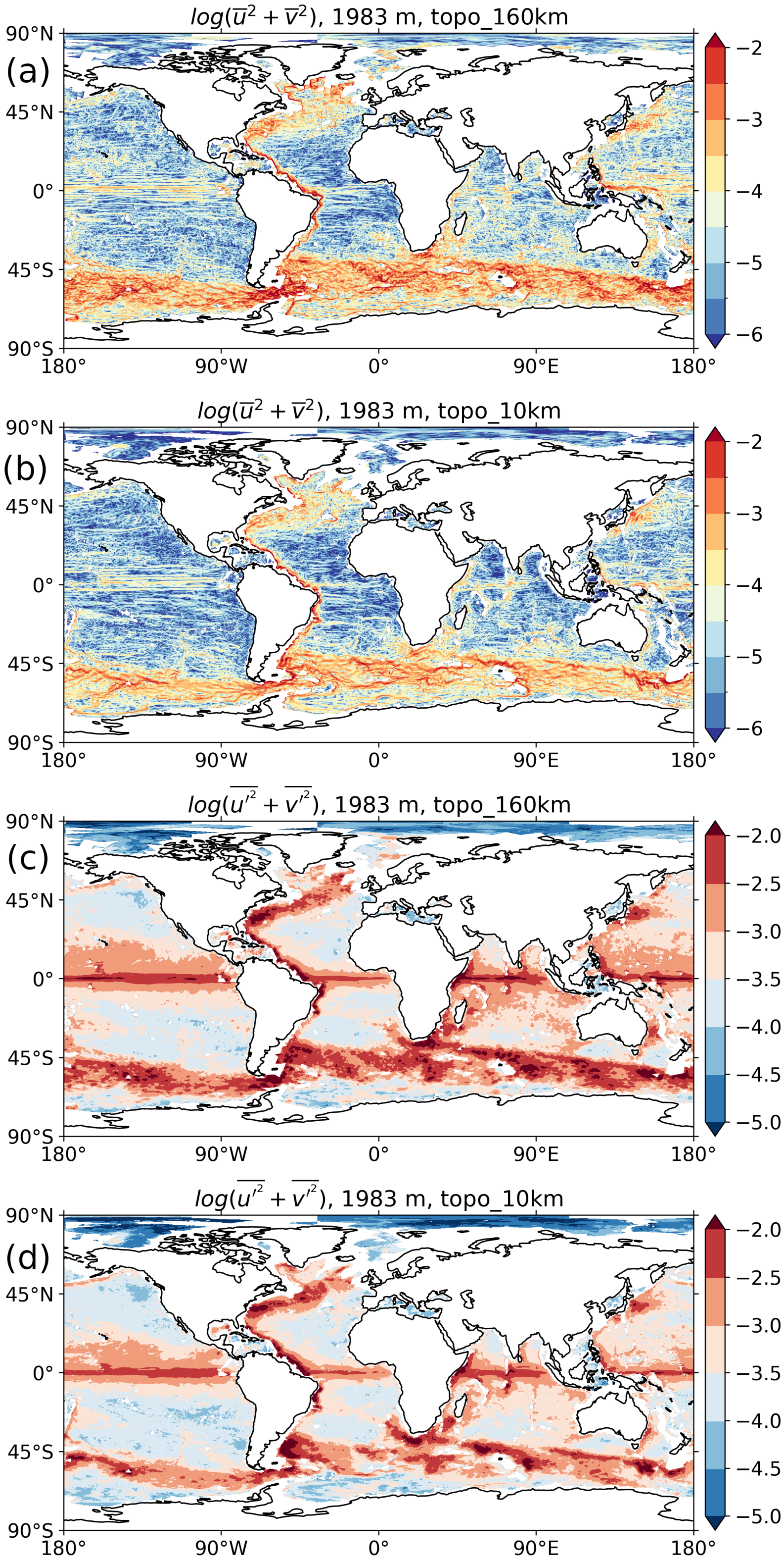

Figure 4.3: Horizontal distribution of $log(\overline{u}^2+\overline{v}^2)$ for (a) **topo_160km** and (b) **topo_10km**, and horizontal distribution of $log(\overline{u'^2}+\overline{v'^2})$ for (c) **topo_160km**, and (d) **topo_10km** at 1983 m depth. Data is derived from 5 years of data, 2015 - 2020.

4.4.3 Sensitivity of the energy cycle to topographic forcing

Here we concentrate on the kinetic branch of the Lorenz Energy Cycle because we are only concerned about kinetic energy and its conversion, $C(K_e, K_m)$ between the mean circulation and the transients. A summary of the kinetic energy branch of the Lorenz Energy Cycle derived from the two simulations — **topo__10km** and **topo__160km** — is shown in figure 4.6. The energy cycle is derived from data averaged over 5 years, 2015 - 2020. Therefore, the variability considered here includes mesoscale eddies, seasonal variability and inter-annual variability.

Overall, the magnitudes are comparable, and the directions of energy exchange are consistent in both configurations. The energies are more intense in the **topo__160km** configuration — as shown in section 4.4.1, the differences are located below 1 km in the ocean interior. The dissipation is also moreless comparable, however, it is more intense in the **topo__160km** configuration. However, it should be noted that dissipation here is calculated as a residual term, and therefore ambiguous to interpret as it also includes numerical errors and also the time change of energy which might not be negligible. Energy generation, $G(K_m)$ and $G(K_e)$ is mostly unchanged, partly because the two configurations are forced in the same way— with the same ERA5 surface fluxes. The generation values obtained here are also comparable to 3.22 TW ($G(K_e)$), and 1.89 TW ($G(K_m)$) obtained from the ICON/ERA5 simulation in Ssebandeke et al., 2023.

The most notable differences in energy conversion are located in the baroclinic pathway, $C(P_m, K_m) \to C(P_m, P_e) \to C(P_e, K_e)$. The largest differences are located in the $C(P_m, K_m)$, which is related to the processes of upwelling — these differences are located at almost all model layers (figure 4.7 (a)). The global integral of $C(P_m, K_m)$ in **topo__10km**, 0.64 TW is 0.16 TW greater than the value in **topo__160km**. For

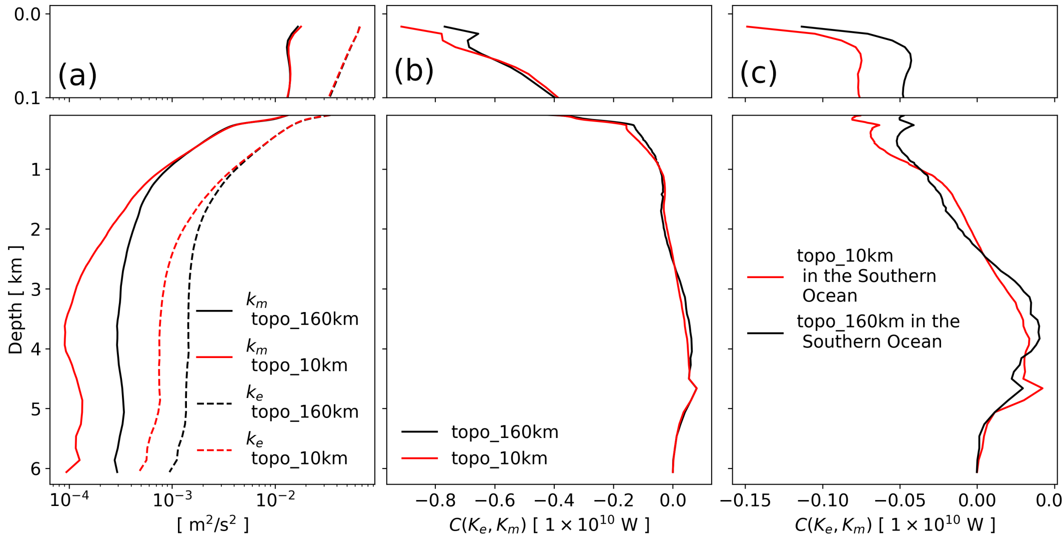

Figure 4.4: Vertical profiles of (a) kinetic energy — mean kinetic energy, K_m (solid line) and eddy kinetic energy, K_e (dashed line), (b) $C(K_e, K_m)$, globally (horizontally) integrated, and (c) $C(K_e, K_m)$, horizontally integrated over the Southern Ocean.

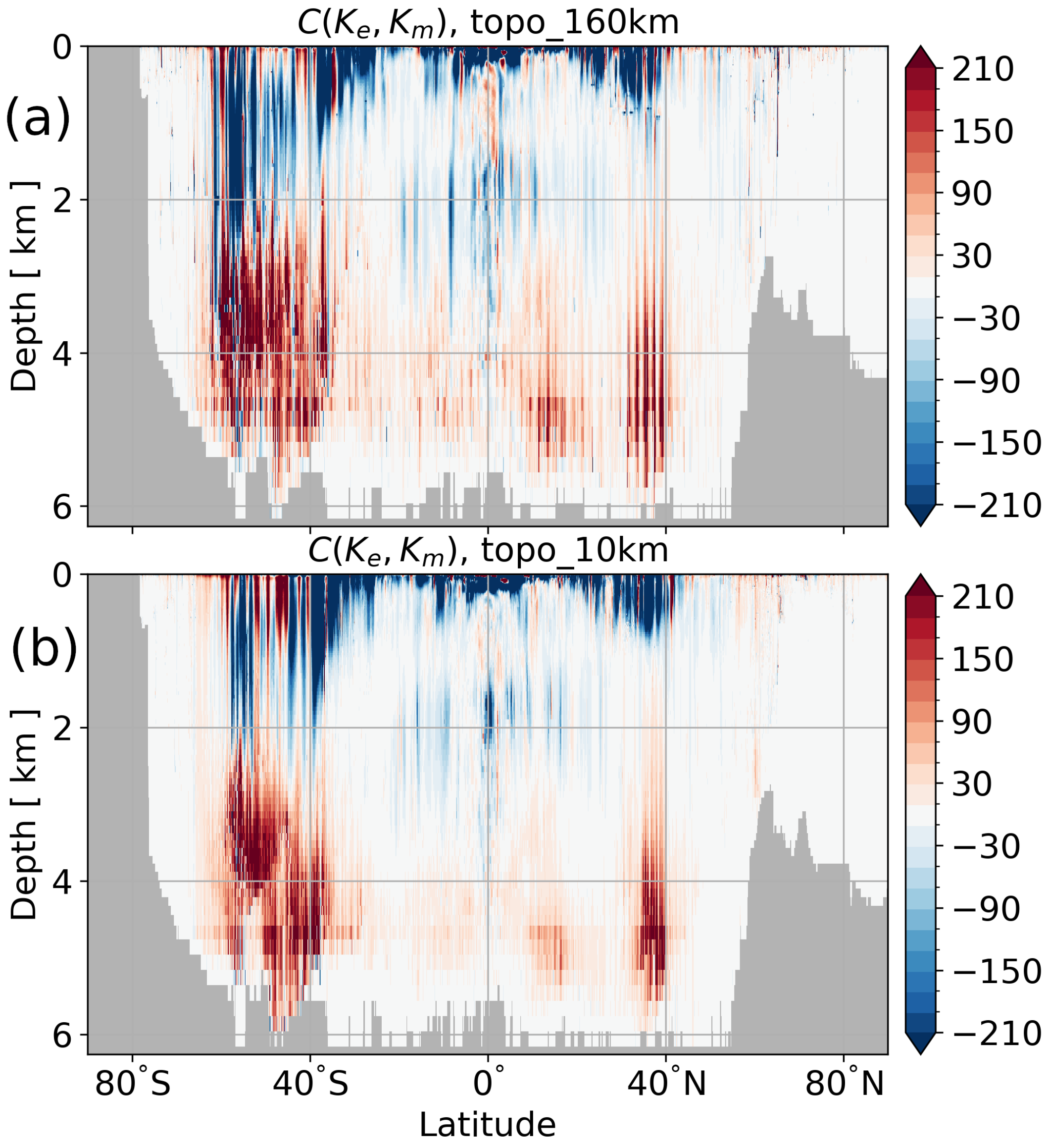

Figure 4.5: Depth-latitude section of the zonally integrated $C(K_e, K_m)$ in (a) **topo_160km** configuration, and (b) **topo_10km** configuration. Units: 1×10^4 W.

the $C(P_m, P_e)$ term, **topo_160km** is 0.02 TW stronger than that in **topo_10km**. Similarly, $C(P_e, K_e)$ is more intense in **topo_160km** (figure 4.7 (b)). The global integral of $C(K_e, K_m)$ in **topo_10km** is only 0.02 TW stronger than that of the **topo_160km** simulation, however the direction of the energy interaction remains unchanged.

4.5 CONCLUSION

Here, we assess whether the sensitivities observed in the idealised, 2-layer simulations are also observed in a complex OGCM. The sensitivities of kinetic energy observed in the complex OGCM are contrary to what was observed in the idealistic, 2-layer

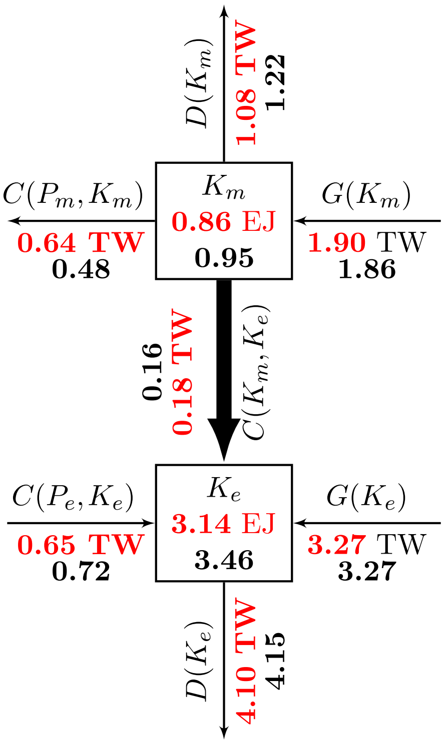

Figure 4.6: Kinetic energy branch of the Lorenz Energy Cycle derived from (black) **topo__160km**, and (red) **topo__10km** configuration. The energy reservoirs are in exa-joules (EJ, 10^{18}). The generation, exchange and dissipation terms are in tera-watts (TW, 10^{12}). Data is averaged over a 5 year period, 2015 - 2020.

model. In the idealistic model, **case 1** with the smoothest topography (uniform zonal ridge) has mostly less intense kinetic energy (figure 4.1). In the complex OGCM, **topo__160km** with a smoother bottom topography has more intense kinetic energy. The sensitivities for the $C(P_m, K_m)$ term, are also contrary — in the idealistic, 2-layer model, $C(P_m, K_m)$ is largest in **case 1** with the smoothest topography. However, in the complex OGCM, $C(P_m, K_m)$ is largest in **topo__10km** with the rougher topography. In the deeper layer, in the idealistic model, the sensitivities for the $C(P_e, K_e)$ are similar to those in the complex OGCM, but contrary in the surface layers. Similarly, the sensitivities of $C(K_e, K_m)$ in the deeper layer, for the ideal model are similar to those in the complex OGCM. In the surface layer however, $C(K_e, K_m)$ is positive for **case 1** but we observed that for a complex OGCM, the gross features of the eddy-mean flow interaction remain unchanged.

The results presented here are preliminary. Further analysis will be conducted for a more complete picture and : (1) to understand why some of the sensitivities in the complex OGCM are contrary to those in the ideal, 2-layer model. (2) assess changes in $C(K_e, K_m)$ over regions. The gross features of $C(K_e, K_m)$ might be insensitive to topographic variations, but there could be regional changes in the $C(K_e, K_m)$ caused by topographic variations. (3) Maybe conduct more extreme simulations —flat bottom experiments using an OGCM. **topo__160km** is not everywhere smoother than the **topo__10km** topography. The former has dedicated jumps at certain points

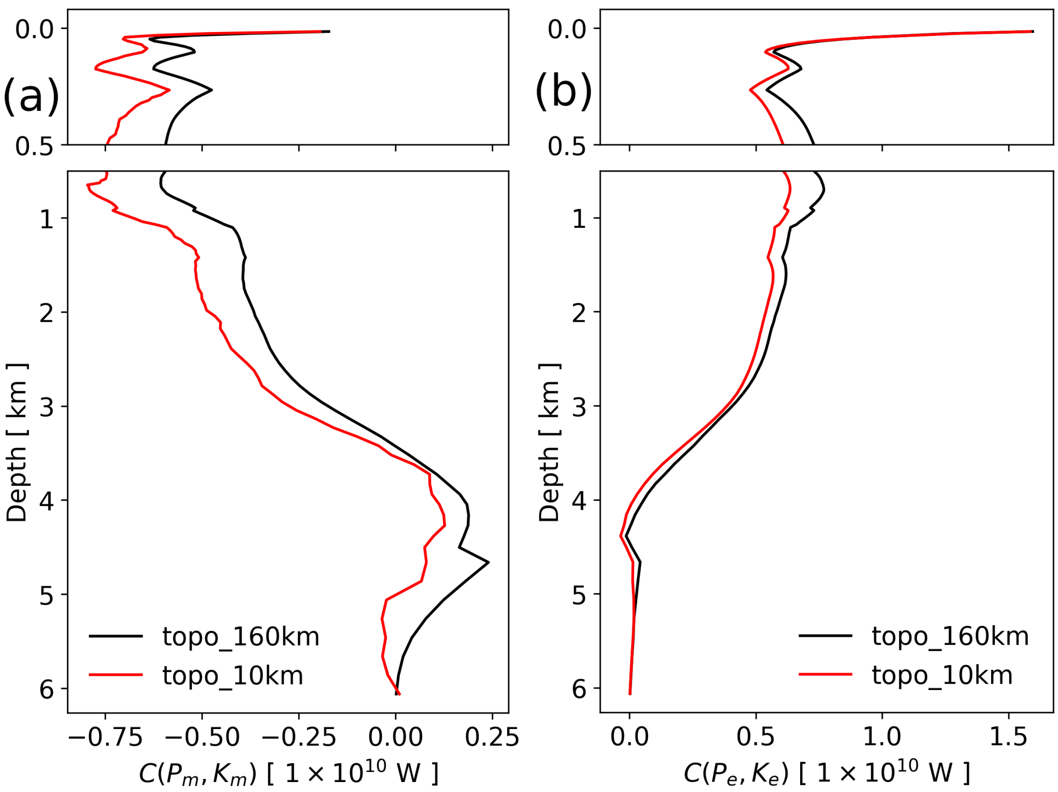

Figure 4.7: Global vertical profiles of (a) $C(P_m, K_m)$ and (b) $C(P_e, K_e)$

(**topo_160km** triangle edges) and is constant until the next **topo_160km** edge. However, these jumps could be quite intense in contrast to smooth variations in the **topo_10km** case. (4) It would also be interesting to investigate the effect of topography on non-locality presented in chapter 3.

5 CONCLUSIONS AND OUTLOOK

> *One never notices what has been done;*
> *one can only see what remains to be done*
>
> — Marie Curie

5.1 ANSWERING THE RESEARCH QUESTIONS

1. **How robust are the characteristics of the oceanic Lorenz Energy Cycle presented in von Storch et al., 2012?**

Because we use a newly developed model — ICON-O, we started by assessing the model prowess from an energetic perspective. The assessment was done by comparing the energy cycle obtained from ICON-O simulations to that obtained from the MPI-OM model, which is an already firmly established model. We observed that ICON-O can effectively simulate global energetics, but it's less energetic compared to MPI-OM with similar resolution [1]. This is an extension to ICON-O model evaluation studies performed before (Korn, 2017; Korn et al., 2022).

As mentioned in section 1.2, to date, there is only one estimate of the global oceanic Lorenz Energy Cycle (von Storch et al., 2012), and therefore it's unclear whether the characteristics observed in that study are robust. In chapter 2, we evaluated the sensitivity of the energy cycle to both model and forcing differences by comparing LECs derived from two simulations based on different eddy-rich ocean models, ICON-O and MPI-OM, both driven by NCEP/NCAR reanalysis; and by comparing LECs derived from two simulations generated using ICON-O model but driven by two different reanalyses, NCEP/NCAR and ERA5. Regarding model difference, we found weaker eddy kinetic energy, k_e in the ICON-O simulation than in the MPI-OM simulation. We attribute this to the higher horizontal resolution of MPI-OM in the Southern Ocean (see table 2.1 for details regarding the differences in the model resolutions). Weaker k_e was observed not to be caused by the lack of eddy available potential energy, p_e, but

---

[1] Note that in this study we have used the $R2B8$ configuration of ICON-O, which has a different configuration compared to the MPI-OM model used in the STORM/NCEP simulation. For details, see chapter 2

by the strong dissipation of p_e and the resulting weak conversion from p_e to k_e. Regarding forcing difference, we find that considerably more mechanical energy is generated by the ERA5 forcing, which has a higher spatial-temporal resolution compared to the NCEP/NCAR forcing. In particular, the generation of k_e, which also contains the resolved part of the internal wave spectrum, is enhanced by about 1 TW (40%). However, the dominance of the baroclinic and the barotropic pathways forces the enhanced generation of k_e to be balanced by an enhanced dissipation in the surface layer. The gross features of LEC are insensitive to both model and forcing differences, picturing the ocean as an inefficient 'windmill' that converts only a small portion of the inputted mechanical energy into the interior mean and transient circulations.

Overall, we observed that the direction and magnitude of all Lorenz Energy Cycle terms are consistent in all simulations and therefore the characteristics observed in von Storch et al., 2012 are robust.

2. **How is kinetic energy exchanged between the mean oceanic circulation and the eddies?**

   It is well established that kinetic energy of the mesoscale variability in the ocean is primarily generated through instabilities, represented as eddy-mean flow interactions in the Lorenz Energy Cycle framework, however, the modality of the interactions is not well characterised due to the nonlocal nature of these energy interactions. In chapter 3, we described how kinetic energy is exchanged between the mean flow and the eddies following eddy-mean flow interactions and outlined the relevance of nonlocality in the distribution of kinetic energy. We showed that the exchange of kinetic energy is such that the mean flow loses energy in the surface layers, and most of the energy released by the mean flow is used for eddy growth, while the rest is transferred to the deeper ocean and then, together with the energy released by the eddies, it's transferred back to the mean flow.

3. **Why is the direction of kinetic energy exchange following eddy-mean flow interaction in the ocean opposite to that in the atmosphere?**

   While kinetic energy transfer is directed from the eddies towards the mean flow in the atmosphere, in the ocean, mean kinetic energy is converted into eddy kinetic energy. It's unclear why these two systems behave differently regarding kinetic energy exchange. Using an idealized 2-layer model, Witter and Chelton, 1998 showed that bottom topography has a large influence on the direction of the energy transfer in the ocean. However, we show that the gross features of the energy exchange are insensitive to bottom topography in a realistic OGCM. Therefore, it remains unclear why the ocean behaves differently compared to the atmosphere regarding the direction of kinetic energy exchange.

5.2 OUTLOOK

We have presented new insights regarding several aspects of the oceanic Lorenz Energy cycle — a framework which is rarely evaluated due to the scarcity of double-variable products of data which are essential for inferring eddy fluxes in the ocean. We have shown that ocean circulation is insensitive to increased energy input, and therefore functions as an inefficient 'windmill' which converts only a small portion of the inputted mechanical energy into the interior mean and transient circulations. Furthermore, we have established that the exchange of kinetic energy is such that the mean flow loses energy in the surface layers, and most of the energy released by the mean flow is used for eddy growth, while the rest is transferred to the deeper ocean and then, together with the energy released by the eddies, it's transferred back to the mean flow.

However, several questions remain unanswered, especially relating to the eddy-mean flow interaction. Key amongst these questions is, why the direction of energy conversion in the atmosphere is opposite to that in the ocean. As mentioned above, idealistic studies suggested that this is related to bottom topography. However, our analysis shows that for a realistic OGCM, changes in bottom topography don't affect the global direction of the energy conversion. Therefore, the cause of the disparity in the direction of energy conversion in the atmosphere and the ocean remains unclear. The scales controlling the eddy-mean flow interaction in the ocean are also unknown.

All the work in this dissertation is based on numerical models, however, numerical models are prone to biases (Farneti et al., 2022). It would be interesting to explore these aspects using observations. Alas, observations necessary for investigating the global ocean Lorenz Energy Cycle are still not available which requires the community to focus on single aspects of the LEC, i.e. a regional focus or a focus on the ocean surface. However, the combination of such observations with high-resolution model simulations provides an interesting potential for future studies.

A DERIVATION OF THE LORENZ ENERGY CYCLE

> *Another advantage of a mathematical statement is that it is so definite that it might be definitely wrong. . . Some verbal statements have not this merit.*
>
> — Lewis Fry Richardson

A.1 KINETIC ENERGY

Starting from the momentum equation under the Boussinesq approximation and a small aspect ratio:

$$\frac{\mathrm{d}\mathbf{u_H}}{\mathrm{d}t} + f\mathbf{k}\times\mathbf{u_H} = -\frac{1}{\rho_\circ}\nabla_\mathbf{H} p + \frac{\partial \tau}{\partial z}$$

where $\mathbf{u} = (\mathbf{u_H}, w) = (u, v, w)$, $\tau = (\tau_x, \tau_y) = A_z \frac{\partial}{\partial z}\mathbf{u_H}$, with A_z the turbulent vertical viscosity, $\nabla_\mathbf{H}$ is a horizontal gradient operator and $\rho_\circ = 1025.022$ kg m^{-3} in ICON-O and p is the hydro-static pressure.

$$\frac{\mathrm{d}}{\mathrm{d}t} = \frac{\partial}{\partial t} + \mathbf{u}\cdot\nabla = \frac{\partial}{\partial t} + \mathbf{u_H}\cdot\nabla_\mathbf{H} + w\frac{\partial}{\partial z}$$

Decompose the variables in the momentum equation in x and y directions into a time average part, over-bar, and a fluctuating part, prime.

$$\frac{\partial}{\partial t}(\overline{v}+v') + (\overline{\mathbf{u}}+\mathbf{u}')\cdot\nabla(\overline{v}+v') + f(\overline{u}+u') = -\frac{1}{\rho_\circ}\frac{\partial}{\partial y}(\overline{p}+p') + \frac{\partial}{\partial z}(\overline{\tau_y}+\tau_y') \quad \text{(A.1)}$$

$$\frac{\partial}{\partial t}(\overline{u}+u') + (\overline{\mathbf{u}}+\mathbf{u}')\cdot\nabla(\overline{u}+u') - f(\overline{v}+v') = -\frac{1}{\rho_\circ}\frac{\partial}{\partial x}(\overline{p}+p') + \frac{\partial}{\partial z}(\overline{\tau_x}+\tau_x') \quad \text{(A.2)}$$

Averaging properties:

$$\begin{aligned} x &= \overline{x} + x' \\ y &= \overline{y} + y' \\ \overline{xy} &= \overline{x}\,\overline{y} + \overline{x'y'} \end{aligned} \tag{A.3}$$

$$\overline{\overline{x}} = \overline{x}, \qquad \overline{x'} = \overline{x - \overline{x}} = \overline{x} - \overline{x} = 0 \tag{A.4}$$

a.1.1 Eddy kinetic energy

Equation (A.1) is multiplied by u' and averaged.

$$\overline{u'\frac{\partial(\overline{u}+u')}{\partial t}} + \overline{u'(\overline{\mathbf{u}}+\mathbf{u}')\cdot\nabla(\overline{u}+u')} - \overline{u'f(\overline{v}+v')} = -\overline{\frac{u'}{\rho_\circ}\frac{\partial(\overline{p}+p')}{\partial x}} \\ + \overline{u'\frac{\partial(\overline{\tau_x}+\tau_x')}{\partial z}} \tag{A.5}$$

Using the averaging properties in A.4, equation (A.5) becomes:

$$\frac{\partial}{\partial t}\left(\frac{\overline{u\prime^2}}{2}\right) + \nabla\cdot\left(\overline{\mathbf{u}}\frac{1}{2}\overline{u\prime^2}\right) + \overline{\mathbf{u}'u'}\cdot\nabla\overline{u} + \nabla\cdot\left(\frac{1}{2}\overline{\mathbf{u}'u\prime^2}\right) - f\overline{u\prime v\prime} = -\overline{\frac{u'}{\rho_\circ}\frac{\partial p'}{\partial x}} \\ + \overline{u'\frac{\partial \tau\prime_x}{\partial z}} \tag{A.6}$$

Similarly, equation (A.2) is multiplied by v' and averaged.

$$\frac{\partial}{\partial t}\left(\frac{\overline{v\prime^2}}{2}\right) + \nabla\cdot\left(\overline{\mathbf{u}}\frac{1}{2}\overline{v\prime^2}\right) + \overline{\mathbf{u}'v'}\cdot\nabla\overline{v} + \nabla\cdot\left(\frac{1}{2}\overline{\mathbf{u}'v\prime^2}\right) + f\overline{u\prime v\prime} = -\overline{\frac{v'}{\rho_\circ}\frac{\partial p'}{\partial y}} \\ + \overline{u'\frac{\partial \tau_y'}{\partial z}} \tag{A.7}$$

Summing up equation (A.6) & (A.7) and multiplying through by $\rho_\circ$ gives:

$$\frac{\partial}{\partial t}\left[\frac{\rho_\circ}{2}\left(\overline{v\prime^2} + \overline{u\prime^2}\right)\right] + \nabla\cdot\left[\overline{\mathbf{u}\frac{\rho_\circ}{2}\left(u\prime^2 + v\prime^2\right)}\right] + \rho_\circ\left(\overline{\mathbf{u\prime_H}\mathbf{u}' : \nabla\overline{\mathbf{u_H}}}\right) = -\overline{\mathbf{u\prime_H}\cdot\nabla_{\mathbf{H}}p'} \\ + \overline{\rho_\circ\mathbf{u\prime_h}\cdot\frac{\partial\tau'}{\partial z}}$$

$$\frac{\partial \overline{k_e}}{\partial t} + \nabla \cdot \left(\overline{\mathbf{u} k_e}\right) + \rho_\circ \left(\overline{\mathbf{u}'_{\mathbf{H}} \mathbf{u}'} : \nabla \overline{\mathbf{u}_{\mathbf{H}}}\right) = \overline{w' \frac{\partial p'}{\partial z}} + \rho_\circ \frac{\partial}{\partial z} \left(\overline{\tau'_x u'} + \overline{\tau'_y v'}\right) \\ - \rho_\circ A_z \left(\frac{\partial \overline{u'}}{\partial z}\right)^2 - \rho_\circ A_z \left(\frac{\partial \overline{v'}}{\partial z}\right)^2$$

$$\Rightarrow \left(\frac{\partial}{\partial t} + \overline{\mathbf{u}} \cdot \nabla\right) k_e + \nabla \cdot \left(\frac{\rho_\circ}{2} \overline{\mathbf{u}'(u\prime^2 + v\prime^2)}\right) = -\rho_\circ \left(\overline{\mathbf{u}\prime_{\mathbf{H}} \mathbf{u}'} : \nabla \overline{\mathbf{u}_{\mathbf{H}}}\right) - g\overline{\rho' w'} \\ + \rho_\circ \frac{\partial}{\partial z} \left(\overline{\tau\prime_x u'} + \overline{\tau\prime_y v'}\right) - \epsilon(k_e) \quad \text{(A.8)}$$

where $k_e = \frac{\rho_\circ}{2} \left(\overline{v\prime^2 + u\prime^2}\right)$, $\epsilon(k_e) = \rho_\circ A_z \left(\frac{\partial \overline{u'}}{\partial z}\right)^2 + \rho_\circ A_z \left(\frac{\partial \overline{v'}}{\partial z}\right)^2$, $\overline{\mathbf{u}\prime_{\mathbf{H}} \mathbf{u}'} : \nabla \overline{\mathbf{u}_{\mathbf{H}}} = \overline{\mathbf{u}' v'} \cdot \nabla \overline{v} + \overline{\mathbf{u}' u'} \cdot \nabla \overline{u}$ (colon denotes the double scalar product). Notice that we have used the continuity equation and hydrostatic equation.

a.1.2 Mean kinetic energy

Equation (A.1) is multiplied by $\overline{u}$ and averaged.

$$\overline{\overline{u} \frac{\partial(\overline{u} + u')}{\partial t}} + \overline{\overline{u}(\overline{\mathbf{u}} + \mathbf{u}') \cdot \nabla(\overline{u} + u')} - \overline{\overline{u} f(\overline{v} + v')} = -\overline{\frac{\overline{u}}{\rho_\circ} \frac{\partial(\overline{p} + p')}{\partial x}} \\ + \overline{\overline{u} \frac{\partial(\overline{\tau_x} + \tau'_x)}{\partial z}} \quad \text{(A.9)}$$

Using the averaging properties in A.4, equation (A.9)

$$\frac{\partial}{\partial t}\left(\frac{\overline{u}^2}{2}\right) + \nabla \cdot \left(\overline{\mathbf{u}} \; \frac{1}{2} \overline{u}^2\right) - \overline{\mathbf{u}' u'} \cdot \nabla \overline{u} + \nabla \cdot \left(\overline{u} \; \overline{\mathbf{u}' u'}\right) - f \overline{u} \; \overline{v} = \frac{\overline{u}}{\rho_\circ} \frac{\partial \overline{p}}{\partial x} \\ + \overline{u} \frac{\partial \overline{\tau_x}}{\partial z} \quad \text{(A.10)}$$

Similarly, equation (A.2) is multiplied by $\overline{v}$ and averaged. This gives:

$$\frac{\partial}{\partial t}\left(\frac{\overline{v}^2}{2}\right) + \nabla \cdot \left(\overline{\mathbf{u}} \; \frac{1}{2} \overline{v}^2\right) - \overline{\mathbf{u}' v'} \cdot \nabla \overline{v} + \nabla \cdot \left(\overline{v} \; \overline{\mathbf{u}' v'}\right) + f \overline{u} \; \overline{v} = \frac{\overline{v}}{\rho_\circ} \frac{\partial \overline{p}}{\partial x} \\ + \overline{v} \frac{\partial \overline{\tau_y}}{\partial z} \quad \text{(A.11)}$$

Summing up equation A.10 & A.11 and multiplying through by $\rho_\circ$

$$\begin{aligned}\left(\frac{\partial k_m}{\partial t}+\overline{\mathbf{u}}\cdot\nabla\right)k_m+\nabla\cdot\left(\rho_\circ\overline{\mathbf{u_H}}\cdot\overline{\mathbf{u}'\mathbf{u}'_{\mathbf{H}}}+\overline{p}\ \overline{\mathbf{u}}\right)-\ \rho_\circ\overline{\mathbf{u}'_{\mathbf{H}}\mathbf{u}'}:\nabla\overline{\mathbf{u_H}}=\overline{w}\frac{\partial\overline{p}}{\partial z}\\+\rho_\circ\overline{\mathbf{u_h}}\cdot\frac{\partial\overline{\tau}}{\partial z}\end{aligned}$$

we define a density, $\rho^*(x,y,z,t)$ and pressure, $p^*(x,y,z,t)$ perturbation relative to a stratified background state

$$\begin{aligned}\rho(x,y,z,t)&=\rho^*(x,y,z,t)+\langle\overline{\rho}\rangle(z)\\p(x,y,z,t)&=p^*(x,y,z,t)+\langle\overline{p}\rangle(z)\end{aligned}$$

$$\begin{aligned}\rho^*&=\overline{\rho^*}+\rho^{*'}\\\Rightarrow\rho^{*'}&=\rho^*-\overline{\rho^*}\\&=(\rho-\langle\overline{\rho}\rangle)-\overline{(\rho-\langle\overline{\rho}\rangle)}\\&=\rho-\overline{\rho}\\\therefore\rho^{*'}&=\rho'\end{aligned}$$

$$\begin{aligned}\rho(x,y,z,t)&=\overline{\rho^*(x,y,z,t)}+\rho'(x,y,z,t)+\langle\overline{\rho}\rangle(z)\\p(x,y,z,t)&=\overline{p^*(x,y,z,t)}+p'(x,y,z,t)+\langle\overline{p}\rangle(z)\end{aligned}\tag{A.12}$$

$$\begin{aligned}\nabla\cdot(\overline{p}\ \overline{u})&=\nabla\cdot(\overline{p^*}\ \overline{u})+\nabla\cdot(\langle\overline{p}\rangle\ \overline{u})\\&=\nabla\cdot(\overline{p^*}\ \overline{u})+\overline{w}\frac{\partial\langle\overline{p}\rangle}{\partial z}\\&=\nabla\cdot(\overline{p^*}\ \overline{u})-g\overline{w}\ \langle\overline{\rho}\rangle\\&=\nabla\cdot(\overline{p^*}\ \overline{u})-g\overline{w}\ \overline{\rho}+g\overline{w}\ \overline{\rho^*}\\\therefore\nabla\cdot(\overline{p}\ \overline{u})+g\overline{w}\ \overline{\rho}&=\nabla\cdot(\overline{p^*}\ \overline{u})+g\overline{w}\ \overline{\rho^*}\end{aligned}\tag{A.13}$$

$$\begin{aligned}\left(\frac{\partial k_m}{\partial t}+\overline{\mathbf{u}}\cdot\nabla\right)k_m+\nabla\cdot\left(\rho_\circ\overline{\mathbf{u_H}}\cdot\overline{\mathbf{u}'\mathbf{u}'_{\mathbf{H}}}+\overline{p}\ \overline{\mathbf{u}}\right)=\rho_\circ\overline{\mathbf{u}'_{\mathbf{H}}\mathbf{u}'}:\nabla\overline{\mathbf{u_H}}\\+\rho_\circ\frac{\partial}{\partial z}\left(\overline{\tau_x}\ \overline{u}+\overline{\tau_y}\ \overline{v}\right)-g\overline{w}\ \overline{\rho}-\rho_\circ A_z\left(\frac{\partial\overline{u}}{\partial z}\right)^2-\rho_\circ A_z\left(\frac{\partial\overline{v}}{\partial z}\right)^2\end{aligned}$$

$$\begin{aligned}\left(\frac{\partial k_m}{\partial t}+\overline{\mathbf{u}}\cdot\nabla\right)k_m+\nabla\cdot\left(\rho_\circ\overline{\mathbf{u_H}}\cdot\overline{\mathbf{u}'\mathbf{u}'_{\mathbf{H}}}+\overline{p}\ \overline{\mathbf{u}}\right)=\rho_\circ\overline{\mathbf{u}'_{\mathbf{H}}\mathbf{u}'}:\nabla\overline{\mathbf{u_H}}\\+\rho_\circ\frac{\partial}{\partial z}\left(\overline{\tau_x}\ \overline{u}+\overline{\tau_y}\ \overline{v}\right)-g\overline{w}\ \overline{\rho}-\epsilon(k_m)\end{aligned}\tag{A.14}$$

Using equation (A.14) and (A.13), the equation for mean kinetic energy becomes:

$$\left(\frac{\partial k_m}{\partial t} + \overline{\mathbf{u}} \cdot \nabla\right) k_m + \nabla \cdot \left(\rho_\circ \overline{\mathbf{u_H}} \cdot \overline{\mathbf{u}'\mathbf{u}'_\mathbf{H}} + \overline{p^*}\ \overline{\mathbf{u}}\right) = \rho_\circ \overline{\mathbf{u}'_\mathbf{H}\mathbf{u}'} : \nabla \overline{\mathbf{u_H}} - g\overline{w}\ \overline{\rho^*}$$
$$+ \rho_\circ \frac{\partial}{\partial z}\left(\overline{\tau_x}\ \overline{u} + \overline{\tau_y}\ \overline{v}\right) - \epsilon(k_m) \quad \text{(A.15)}$$

where $k_m = \frac{\rho_\circ}{2}\left(\overline{v}^2 + \overline{u}^2\right)$, $\epsilon(k_m) = \rho_\circ A_z \left(\frac{\partial \overline{u}}{\partial z}\right)^2 + \rho_\circ A_z \left(\frac{\partial \overline{v}}{\partial z}\right)^2$

A.2 AVAILABLE POTENTIAL ENERGY

$$\begin{aligned} \rho\,(x,y,z,t) &= \rho\,(\theta, S, \rho_\circ g z) \\ \frac{\mathrm{d}\rho}{\mathrm{d}t} &= \left(\frac{\partial \rho}{\partial \theta}\right)_{S,z} \frac{\mathrm{d}\theta}{\mathrm{d}t} + \left(\frac{\partial \rho}{\partial S}\right)_{\theta,z} \frac{\mathrm{d}S}{\mathrm{d}t} + \left(\frac{\partial \rho}{\partial z}\right)_{S,\theta} \frac{\mathrm{d}z}{\mathrm{d}t} \end{aligned}$$

The temporal variations of the thermal expansion coefficient and the haline contraction coefficient are neglected.

$$\begin{aligned} \left(\frac{\partial \rho}{\partial \theta}\right)_{S,z} \approx \left(\frac{\partial \overline{\rho}}{\partial \theta}\right)_{S,z} &\equiv \alpha_\circ\,(\lambda, \varphi, z) \\ \left(\frac{\partial \rho}{\partial S}\right)_{\theta,z} \approx \left(\frac{\partial \overline{\rho}}{\partial S}\right)_{\theta,z} &\equiv \beta_\circ\,(\lambda, \varphi, z) \end{aligned}$$

$$\begin{aligned} \frac{\mathrm{d}\theta}{\mathrm{d}t} &= \frac{\partial J}{\partial z}, J = \frac{1}{\rho_s c} H, c = 4000 J/kg/K \\ \frac{\mathrm{d}S}{\mathrm{d}t} &= \frac{\partial G}{\partial z},\quad G = -\overline{S_1}(\mathcal{E} - P) \end{aligned}$$

$$\frac{\mathrm{d}\rho}{\mathrm{d}t} = \alpha_\circ \frac{\partial J}{\partial z} + \beta_\circ \frac{\partial G}{\partial z} + w \left(\frac{\partial \rho}{\partial z}\right)_{S,\theta} \quad \text{(A.16)}$$

Putting equation (A.16) & (A.12) together:

$$\frac{\partial}{\partial t}\left(\overline{\rho^*} + \rho'\right) + \mathbf{u} \cdot \nabla \left(\overline{\rho^*} + \rho' + \langle \overline{\rho} \rangle\right) = \alpha_\circ \frac{\partial J}{\partial z} + \beta_\circ \frac{\partial G}{\partial z} + w \left(\frac{\partial \rho^*}{\partial z}\right)_{S,\theta}$$
$$+ w \left(\frac{\partial \langle \overline{\rho} \rangle}{\partial z}\right)_{S,\theta}$$

$$\begin{aligned}\frac{\partial}{\partial t}\left(\overline{\rho^*}+\rho'\right)+\mathbf{u}\cdot\nabla\left(\overline{\rho^*}+\rho'\right)+w\frac{\partial\langle\overline{\rho}\rangle}{\partial z}-w\left(\frac{\partial\langle\overline{\rho}\rangle}{\partial z}\right)_{S,\theta} &= \alpha_\circ\frac{\partial J}{\partial z}+\beta_\circ\frac{\partial G}{\partial z}\\ &\quad +w\left(\frac{\partial\rho^*}{\partial z}\right)_{S,\theta}\end{aligned}$$

The last term on the right is neglected i.e. compressibility difference between in-situ density and the background state. This makes the in-situ density identical to potential density i.e we only need potential density for the calculation

$$\frac{\partial}{\partial t}\left(\overline{\rho^*}+\rho'\right) + \mathbf{u} \cdot \nabla\left(\overline{\rho^*}+\rho'\right) + w\left[\frac{\partial\langle\overline{\rho}\rangle}{\partial z}-\left(\frac{\partial\langle\overline{\rho}\rangle}{\partial z}\right)_{S,\theta}\right] = \alpha_\circ\frac{\partial J}{\partial z} + \beta_\circ\frac{\partial G}{\partial z}$$

$\frac{\partial\langle\overline{\rho}\rangle}{\partial z}-\left(\frac{\partial\langle\overline{\rho}\rangle}{\partial z}\right)_{S,\theta}\approx\frac{\partial\langle\overline{\varrho}\rangle}{\partial z}=n_\circ(z)$. Where ϱ is the potential density.

$$\frac{\partial}{\partial t}\left(\overline{\rho^*}+\rho'\right) + \mathbf{u} \cdot \nabla\left(\overline{\rho^*}+\rho'\right) + n_\circ w = \alpha_\circ\frac{\partial J}{\partial z} + \beta_\circ\frac{\partial G}{\partial z} \qquad \text{(A.17)}$$

a.2.1 Eddy available potential energy

Decompose variables in equation (A.17) into a time average, over-bar, and fluctuating part, prime. Then multiply by $(-\frac{g}{n_\circ}\rho')$ and finally average the entire equation

$$\begin{aligned}&\overline{-\frac{g}{n_\circ}\rho'\frac{\partial}{\partial t}\left(\overline{\rho^*}+\rho'\right)}-\overline{\frac{g}{n_\circ}\rho'\left(\overline{\mathbf{u}}+\mathbf{u}'\right)\cdot\nabla\left(\overline{\rho^*}+\rho'\right)}-\overline{g\rho'\left(\overline{w}+w'\right)}\\ &\qquad = -\overline{\alpha_\circ\frac{g}{n_\circ}\rho'\frac{\partial}{\partial z}\left(\overline{J}+J'\right)}-\overline{\beta_\circ\frac{g}{n_\circ}\rho'\frac{\partial}{\partial z}\left(\overline{G}+G'\right)}\end{aligned}$$

$$\begin{aligned}&\frac{\partial}{\partial t}\left(-\frac{g}{(2n_\circ)}\overline{\rho\prime^2}\right)+\nabla\cdot\left(-\overline{\mathbf{u}\frac{g}{(2n_\circ)}\rho\prime^2}\right)-\overline{\frac{g}{(2n_\circ)}\rho\prime^2\cdot\frac{w}{n_\circ}\frac{\partial n_\circ}{\partial z}}-\frac{g}{n_\circ}\overline{\rho'\mathbf{u}'}\cdot\nabla\overline{\rho^*}\\ &\qquad -g\overline{\rho\prime w'}=-\overline{\alpha_\circ\frac{g}{n_\circ}\rho'\frac{\partial J'}{\partial z}}-\overline{\beta_\circ\frac{g}{n_\circ}\rho'\frac{\partial G'}{\partial z}}\end{aligned}$$

$$\begin{aligned}\left(\frac{\partial}{\partial t}+\overline{\mathbf{u}}\cdot\nabla\right)p_e-\frac{g}{n_\circ}\overline{\rho'\mathbf{u}'}\cdot\nabla\overline{\rho^*}-g\overline{\rho'w'} &= \alpha_\circ\frac{g}{n_\circ}\overline{J'\frac{\partial\rho'}{\partial z}}+\beta_\circ\frac{g}{n_\circ}\overline{G'\frac{\partial\rho'}{\partial z}}\\ &\quad -\alpha_\circ\frac{g}{n_\circ}\frac{\partial\overline{J'\rho'}}{\partial z}-\beta_\circ\frac{g}{n_\circ}\frac{\partial\overline{G'\rho'}}{\partial z}+R(p_e)\end{aligned}$$

Where $p_e = -\frac{g}{(2n_\circ)}\overline{\rho\prime^2}$, $R(p_e) = \overline{\frac{g}{(2n_\circ)}\rho\prime^2 \cdot \frac{w}{n_\circ}\frac{\partial n_\circ}{\partial z}}$ and $\epsilon(p_e) = -\alpha_\circ \frac{g}{n_\circ}\overline{J'\frac{\partial \rho'}{\partial z}} - \beta_\circ \frac{g}{n_\circ}\overline{G'\frac{\partial \rho'}{\partial z}}$

$$\left(\frac{\partial}{\partial t} + \overline{\mathbf{u}} \cdot \nabla\right) p_e = \frac{g}{n_\circ}\overline{\rho'\mathbf{u}'} \cdot \nabla\overline{\rho^*} + g\overline{\rho' w'} - \alpha_\circ \frac{g}{n_\circ}\frac{\partial \overline{J'\rho'}}{\partial z} - \beta_\circ \frac{g}{n_\circ}\frac{\partial \overline{G'\rho'}}{\partial z} - \epsilon(p_e) + R(p_e) \quad \text{(A.18)}$$

a.2.2 Mean available potential energy

Decompose variables in equation (A.17) into a time average, over-bar, and fluctuating part, prime. Then multiply by $(-\frac{g}{n_\circ}\overline{\rho^*})$ and finally average the entire equation

$$\overline{-\frac{g}{n_\circ}\overline{\rho^*}\frac{\partial}{\partial t}\left(\overline{\rho^*} + \rho'\right)} - \overline{\frac{g}{n_\circ}\overline{\rho^*}\left(\overline{\mathbf{u}} + \mathbf{u}'\right) \cdot \nabla\left(\overline{\rho^*} + \rho'\right)} - \overline{g\overline{\rho^*}\left(\overline{w} + w'\right)} = \overline{-\alpha_\circ \frac{g}{n_\circ}\overline{\rho^*}\frac{\partial}{\partial z}\left(\overline{J} + J'\right)} - \overline{\beta_\circ \frac{g}{n_\circ}\overline{\rho^*}\frac{\partial}{\partial z}\left(\overline{G} + G'\right)}$$

$$\left(\frac{\partial}{\partial t} + \overline{\mathbf{u}} \cdot \nabla\right) p_m + \nabla \cdot \left(-\frac{g}{n_\circ}\overline{\rho^*}\ \overline{\mathbf{u}'\rho'}\right) + p_m \cdot \frac{\overline{w}}{n_\circ}\frac{\partial n_\circ}{\partial z} + \frac{g}{n_\circ}\overline{\mathbf{u}'\textbf{æ}'} \cdot \nabla\overline{\rho^*} - g\overline{\rho^*}\,\overline{w} + g\overline{\rho^*}\,\overline{\rho' w'}\frac{\partial}{\partial z}\left(\frac{1}{n_\circ}\right) = -\alpha_\circ \frac{g}{n_\circ}\overline{\rho^*}\frac{\partial \overline{J}}{\partial z} - \beta_\circ \frac{g}{n_\circ}\overline{\rho^*}\frac{\partial \overline{G}}{\partial z}$$

$$\left(\frac{\partial}{\partial t} + \overline{\mathbf{u}} \cdot \nabla\right) p_m + \nabla \cdot \left(-\frac{g}{n_\circ}\overline{\rho^*}\ \overline{\mathbf{u}'\rho'}\right) = -p_m \cdot \frac{\overline{w}}{n_\circ}\frac{\partial n_\circ}{\partial z} - \frac{g}{n_\circ}\overline{\mathbf{u}'\textbf{æ}'} \cdot \nabla\overline{\rho^*} + g\overline{\rho^*}\,\overline{w} - \alpha_\circ \frac{g}{n_\circ}\frac{\partial \overline{J}\,\overline{\rho^*}}{\partial z} + \alpha_\circ \frac{g}{n_\circ}\overline{J}\frac{\partial \overline{\rho^*}}{\partial z} - \beta_\circ \frac{g}{n_\circ}\frac{\partial \overline{G}\,\overline{\rho^*}}{\partial z} + \beta_\circ \overline{G}\frac{g}{n_\circ}\frac{\partial \overline{\rho^*}}{\partial z} - g\overline{\rho^*}\,\overline{\rho' w'}\frac{\partial}{\partial z}\left(\frac{1}{n_\circ}\right)$$

Where $p_m = -\frac{g}{(2n_\circ)}\overline{\rho^*}^2$, $R(p_m) = -g\overline{\rho^*}\,\overline{\rho' w'}\frac{\partial}{\partial z}\left(\frac{1}{n_\circ}\right) - p_m \cdot \frac{\overline{w}}{n_\circ}\frac{\partial n_\circ}{\partial z}$ and $\epsilon(p_m) = -\beta_\circ \overline{G}\frac{g}{n_\circ}\frac{\partial \overline{\rho^*}}{\partial z} - \alpha_\circ \frac{g}{n_\circ}\overline{J}\frac{\partial \overline{\rho^*}}{\partial z}$

$$\left(\frac{\partial}{\partial t} + \overline{\mathbf{u}} \cdot \nabla\right) p_m + \nabla \cdot \left(-\frac{g}{n_\circ}\overline{\rho^*}\ \overline{\mathbf{u}'\rho'}\right) = -\frac{g}{n_\circ}\overline{\mathbf{u}'\textbf{æ}'} \cdot \nabla\overline{\rho^*} + g\overline{\rho^*}\,\overline{w} - \alpha_\circ \frac{g}{n_\circ}\frac{\partial \overline{J}\,\overline{\rho^*}}{\partial z} - \beta_\circ \frac{g}{n_\circ}\frac{\partial \overline{G}\,\overline{\rho^*}}{\partial z} - \epsilon(p_m) + R(p_m) \quad \text{(A.19)}$$

$$\frac{g}{n_\circ}\overline{\mathbf{u}'\rho'} \quad \cdot \quad \nabla\overline{\rho^*} \quad = \quad \frac{g}{n_\circ}\overline{\mathbf{u}'_{\mathbf{H}}\rho'} \quad \cdot \quad \nabla_{\mathbf{H}}\overline{\rho^*} \quad + \quad \frac{g}{n_\circ}\overline{w'\rho'}\frac{\partial}{\partial z}\overline{\rho^*} \tag{A.20}$$

The last term of equation (A.20), $R(p_e)$ and $R(p_m)$ aren't involved in quasi-geostrophic eddy dynamics and therefore neglected (von Storch et al., 2012; Chen et al., 2014; Olbers et al., 2012).

Mean available potential energy

$$\left(\frac{\partial}{\partial t} + \overline{\mathbf{u}}\cdot\nabla\right)p_m + \nabla\cdot\left(-\frac{g}{n_\circ}\overline{\rho^*}\;\overline{\mathbf{u}'\rho'}\right) = -\frac{g}{n_\circ}\overline{\mathbf{u}'_{\mathbf{H}}\textbf{æ}'}\cdot\nabla_{\mathbf{H}}\overline{\rho^*} + g\overline{\rho^*}\,\overline{w} - \alpha_\circ\frac{g}{n_\circ}\frac{\partial\overline{J}\,\overline{\rho^*}}{\partial z}$$
$$- \beta_\circ\frac{g}{n_\circ}\frac{\partial\overline{G}\,\overline{\rho^*}}{\partial z} - \epsilon(p_m)$$

Eddy available potential energy

$$\left(\frac{\partial}{\partial t} + \overline{\mathbf{u}}\cdot\nabla\right)p_e = \frac{g}{n_\circ}\overline{\mathbf{u}'_{\mathbf{H}}\textbf{æ}'}\cdot\nabla_{\mathbf{H}}\overline{\rho^*} + g\overline{\rho'w'} - \alpha_\circ\frac{g}{n_\circ}\frac{\partial\overline{J'\rho'}}{\partial z} - \beta_\circ\frac{g}{n_\circ}\frac{\partial\overline{G'\rho'}}{\partial z}$$
$$- \epsilon(p_e)$$

A.3 LORENZ ENERGY CYCLE

Reservoir terms

$$P_m = -\int_V \frac{g}{(2n_\circ)}\overline{\rho^*}^2\,\mathrm{d}V$$
$$P_e = -\int_V \frac{g}{(2n_\circ)}\overline{\rho\prime^2}\,\mathrm{d}V$$
$$K_m = \int_V \frac{\rho_\circ}{2}\left(\overline{u}^2 + \overline{v}^2\right)\mathrm{d}V$$
$$K_e = \int_V \frac{\rho_\circ}{2}\left(\overline{u\prime^2} + \overline{v\prime^2}\right)\mathrm{d}V$$

Generation terms

$$
\begin{aligned}
G(P_m) &= -\int_S \alpha_\circ \frac{g}{n_\circ} \overline{J}\,\overline{\rho^*}\ \,\mathrm{d}S - \int_S \beta_\circ \frac{g}{n_\circ} \overline{G}\,\overline{\rho^*}\ \,\mathrm{d}S \\
G(P_e) &= -\int_S \alpha_\circ \frac{g}{n_\circ} \overline{J'\rho'}\ \,\mathrm{d}S - \int_S \beta_\circ \frac{g}{n_\circ} \overline{G'\rho'}\ \,\mathrm{d}S \\
G(K_m) &= \int_S \rho_\circ \left(\overline{\tau_x}\ \overline{u} + \overline{\tau_y}\ \overline{v}\right)\ \,\mathrm{d}S \\
G(K_e) &= \int_S \rho_\circ \left(\overline{\tau_x' u'} + \overline{\tau_y' v'}\right)\ \,\mathrm{d}S
\end{aligned}
$$

Conversion terms

$$
\begin{aligned}
C(P_m, P_e) &= -\int_V \frac{g}{n_\circ} \overline{\mathbf{u'_H}\rho'} \cdot \nabla_{\mathbf{H}} \overline{\rho^*}\ \,\mathrm{d}V \\
C(K_e, K_m) &= \int_V \rho_\circ \left(\overline{\mathbf{u'_H}\mathbf{u'}} : \nabla \overline{\mathbf{u_H}}\right)\ \,\mathrm{d}V \\
C(P_m, K_m) &= -\int_V g\overline{\rho^*}\,\overline{w}\ \,\mathrm{d}V \\
C(P_e, K_e) &= -\int_V g\overline{\rho' w'}\ \,\mathrm{d}V
\end{aligned}
$$

In steady state:

$$
\begin{aligned}
\frac{\partial P_m}{\partial t} &= C(P_e, P_m) - C(P_m, K_m) + G(P_m) - D(P_m) = 0 \\
\frac{\partial P_e}{\partial t} &= -C(P_e, P_m) - C(P_e, K_e) + G(P_e) - D(P_e) = 0 \\
\frac{\partial K_m}{\partial t} &= C(K_e, K_m) + C(P_m, K_m) + G(K_m) - D(K_m) = 0 \\
\frac{\partial K_e}{\partial t} &= -C(K_e, K_m) + C(P_e, K_e) + G(K_e) - D(K_e) = 0
\end{aligned}
$$

BIBLIOGRAPHY

Aiki, Hidenori, Xiaoming Zhai, and Richard J Greatbatch (2016). “Energetics of the global ocean: The role of mesoscale eddies.” In: *Indo-Pacific climate variability and predictability*, pp. 109–134.

Augier, Pierre and Erik Lindborg (2013). “A new formulation of the spectral energy budget of the atmosphere, with application to two high-resolution general circulation models.” In: *Journal of the atmospheric sciences* 70.7, pp. 2293–2308.

Bishop, Stuart P, R Justin Small, and Frank O Bryan (2020). “The global sink of available potential energy by mesoscale air-sea interaction.” In: *Journal of Advances in Modeling Earth Systems* 12.10, e2020MS002118.

Blanke, Bruno and Pascale Delecluse (1993). “Variability of the tropical Atlantic Ocean simulated by a general circulation model with two different mixed-layer physics.” In: *Journal of Physical Oceanography* 23.7, pp. 1363–1388.

Bleck, Rainer (1985). “On the conversion between mean and eddy components of potential and kinetic energy in isentropic and isopycnic coordinates.” In: *Dynamics of atmospheres and oceans* 9.1, pp. 17–37.

Boer, George J and S Lambert (2008). “The energy cycle in atmospheric models.” In: *Climate dynamics* 30, pp. 371–390.

Bryden, Harry L (1982). “Sources of eddy energy in the Gulf Stream recirculation region.” In.

Buzzicotti, Michele, Benjamin A Storer, Stephen M Griffies, and Hussein Aluie (2022). “A coarse-grained decomposition of surface geostrophic kinetic energy in the global ocean.” In: *Authorea Preprints*.

Capó, Esther, Alejandro Orfila, Evan Mason, and Simón Ruiz (2019). “Energy conversion routes in the Western Mediterranean Sea estimated from eddy–mean flow interactions.” In: *Journal of Physical Oceanography* 49.1, pp. 247–267.

Chen, Ru, Glenn R Flierl, and Carl Wunsch (2014). “A description of local and nonlocal eddy–mean flow interaction in a global eddy-permitting state estimate.” In: *Journal of Physical Oceanography* 44.9, pp. 2336–2352.

Chereskin, TK and D Roemmich (1991). “A comparison of measured and wind-derived Ekman transport at 11 N in the Atlantic Ocean.” In: *Journal of Physical Oceanography* 21.6, pp. 869–878.

Cowan, Duncan and Gordon Cooper (2005). “The Shuttle Radar Topography Mission? a new source of near-global digital elevation data.” In: *Exploration Geophysics* 36.4, pp. 334–340.

Eden, Carsten, Lars Czeschel, and Dirk Olbers (2014). “Toward energetically consistent ocean models.” In: *Journal of Physical Oceanography* 44.12, pp. 3160–3184.

Eden, Carsten and Richard J Greatbatch (2008). “Towards a mesoscale eddy closure.” In: *Ocean Modelling* 20.3, pp. 223–239.

Farneti, Riccardo, Alessandro Stiz, and John B Ssebandeke (2022). “Improvements and persistent biases in the southeast tropical Atlantic in CMIP models.” In: *npj Climate and Atmospheric Science* 5.1, pp. 1–11.

Feddersen, Falk, EL Gallagher, RT Guza, and Steve Elgar (2003). "The drag coefficient, bottom roughness, and wave-breaking in the nearshore." In: *Coastal Engineering* 48.3, pp. 189–195.

Ferrari, Raffaele and Carl Wunsch (2009). "Ocean circulation kinetic energy: Reservoirs, sources, and sinks." In: *Annual Review of Fluid Mechanics* 41.

Gaspar, Philippe, Yves Grégoris, and Jean-Michel Lefevre (1990a). "A simple eddy kinetic energy model for simulations of the oceanic vertical mixing: Tests at station Papa and long-term upper ocean study site." In: *Journal of Geophysical Research: Oceans* 95.C9, pp. 16179–16193.

Gaspar, Philippe, Yves Grégoris, and Jean-Michel Lefevre (1990b). "A simple eddy kinetic energy model for simulations of the oceanic vertical mixing: Tests at station Papa and long-term upper ocean study site." In: *Journal of Geophysical Research: Oceans* 95.C9, pp. 16179–16193. DOI: `https://doi.org/10.1029/JC095iC09p16179`. eprint: `https://agupubs.onlinelibrary.wiley.com/doi/pdf/10.1029/JC095iC09p16179`. URL: `https://agupubs.onlinelibrary.wiley.com/doi/abs/10.1029/JC095iC09p16179`.

Gent, Peter R and James C Mcwilliams (1990). "Isopycnal mixing in ocean circulation models." In: *Journal of Physical Oceanography* 20.1, pp. 150–155.

Harrison, DE and AR Robinson (1978). "Energy analysis of open regions of turbulent flows—Mean eddy energetics of a numerical ocean circulation experiment." In: *Dynamics of Atmospheres and Oceans* 2.2, pp. 185–211.

Hersbach, Hans, Bill Bell, Paul Berrisford, Shoji Hirahara, András Horányi, Joaquín Muñoz-Sabater, Julien Nicolas, Carole Peubey, Raluca Radu, Dinand Schepers, et al. (2020). "The ERA5 global reanalysis." In: *Quarterly Journal of the Royal Meteorological Society* 146.730, pp. 1999–2049.

Holland, William R (1978). "The role of mesoscale eddies in the general circulation of the ocean—Numerical experiments using a wind-driven quasi-geostrophic model." In: *Journal of Physical Oceanography* 8.3, pp. 363–392.

Ivey, GN and J Imberger (1991). "On the nature of turbulence in a stratified fluid. Part I: The energetics of mixing." In: *Journal of Physical Oceanography* 21.5, pp. 650–658.

Jamet, Quentin, Stephanie Leroux, William K Dewar, Thierry Penduff, Julien Le Sommer, Jean-marc Molines, and Jonathan Gula (2022). "Non-Local Eddy-Mean Kinetic Energy Transfers in Submesoscale-Permitting Ensemble Simulations." In: *Journal of Advances in Modeling Earth Systems* 14.10.

Jayne, Steven R and Jochem Marotzke (2002). "The oceanic eddy heat transport." In: *Journal of Physical Oceanography* 32.12, pp. 3328–3345.

Jungclaus, J.H., N. Fischer, H. Haak, K. Lohmann, J. Marotzke, D. Matei, U. Mikolajewicz, D. Notz, and J.S. Storch (2013). "Characteristics of the ocean simulations in the Max Planck Institute Ocean Model (MPIOM) the ocean compo- nent of the MPI-Earth system model." In: *J. Adv. Model. Earth Syst.* 5, pp. 422–446. DOI: `doi:10.1002/jame.20023`.

Jungclaus, Johann H, Stephan J Lorenz, Hauke Schmidt, Victor Brovkin, Nils Brüggemann, Fatemeh Chegini, Traute Crüger, Philipp De-Vrese, Veronika Gayler, Marco A Giorgetta, et al. (2022). "The ICON earth system model version 1.0." In: *Journal of Advances in Modeling Earth Systems* 14.4, e2021MS002813.

Kalnay, E., M. Kanamitsu, R. Kistler, W. Collins, D. Deaven, L. Gandin, et al. (1996). "The NCEP/NCAR 40-Year Reanalysis Project." In: *Bulletin of the American Meteorological Society* 77.3, pp. 437 –472.

Kang, Dujuan and Enrique N Curchitser (2015). “Energetics of eddy–mean flow interactions in the Gulf Stream region.” In: *Journal of Physical Oceanography* 45.4, pp. 1103–1120.

Kim, YH. and MK. Kim (2013a). “Examination of the global lorenz energy cycle using MERRA and NCEP-reanalysis 2.” In: *Clim Dyn* 40, pp. 1499–1513. URL: `https://doi.org/10.1007/s00382-012-1358-4`.

Kim, Yeon-Hee and Maeng-Ki Kim (2013b). “Examination of the global lorenz energy cycle using MERRA and NCEP-reanalysis 2.” In: *Climate Dynamics* 40.5-6, pp. 1499–1513.

Korn, P., N. Brüggemann, J. H. Jungclaus, S. J. Lorenz, O. Gutjahr, H. Haak, et al. (2022). “ICON-O: The Ocean Component of the ICON Earth System Model—Global Simulation Characteristics and Local Telescoping Capability.” In: *Journal of Advances in Modeling Earth Systems* 14.10. e2021MS002952 2021MS002952, e2021MS002952.

Korn, Peter (2017). “Formulation of an unstructured grid model for global ocean dynamics.” In: *Journal of Computational Physics* 339, pp. 525–552.

Li, Liming, Andrew P Ingersoll, Xun Jiang, Daniel Feldman, and Yuk L Yung (2007). “Lorenz energy cycle of the global atmosphere based on reanalysis datasets.” In: *Geophysical Research Letters* 34.16.

Loose, Nora, Scott Bachman, Ian Grooms, and Malte Jansen (2023). “Diagnosing scale-dependent energy cycles in a high-resolution isopycnal ocean model.” In: *Journal of Physical Oceanography* 53.1, pp. 157–176.

Lorenz, E.N. (1955). “Available potential energy and the maintenance of the general circulation.” In: *Tellus* 7, pp. 157–167. URL: `h`.

Lorenz, E.N. (1967). *The nature and theory of the general circulation of the atmosphere.* WMO- No. 218. WMO, p. 161.

von Storch, Jin-Song (2019). “Energetics of the Climate System.” In: *Oxford Research Encyclopedia of Climate Science.*

von Storch, Jin-Song, Carsten Eden, Irina Fast, Helmuth Haak, Daniel Hernández-Deckers, Ernst Maier-Reimer, Jochem Marotzke, and Detlef Stammer (2012). “An estimate of the Lorenz energy cycle for the world ocean based on the STORM/NCEP simulation.” In: *Journal of physical oceanography* 42.12, pp. 2185–2205.

Manabe, Syukuro (1971). *General circulation of the atmosphere.*

Margules, Max (1905). “On the energy of storms.” In: *Smithson. Misc. Collect* 51, pp. 533–595.

Marques, C., A. Rocha, J. Corte-Real, J. Castanheira, J. Ferreira, and P. Melo-Goncalves (2009). “Global atmospheric energetics from NCEP-reanalysis 2 and ECMWF-ERA40 reanalysis.” In: *international Journal of Climatology* 29, pp. 159–174.

Marshall, David P and Alistair J Adcroft (2010). “Parameterization of ocean eddies: Potential vorticity mixing, energetics and Arnold’s first stability theorem.” In: *Ocean Modelling* 32.3-4, pp. 188–204.

Marsland, Simon J, Helmuth Haak, Johann H Jungclaus, Mojib Latif, and Frank Röske (2003). “The Max-Planck-Institute global ocean/sea ice model with orthogonal curvilinear coordinates.” In: *Ocean modelling* 5.2, pp. 91–127.

Matsuta, Takuro and Yukio Masumoto (2021). “Modified view of energy budget diagram and its application to the Kuroshio Extension region.” In: *Journal of Physical Oceanography* 51.4, pp. 1163–1175.

Matsuta, Takuro and Yukio Masumoto (2023). “Energetics of the Antarctic Circumpolar Current. Part I: The Lorenz energy cycle and the vertical energy redistribution.” In: *Journal of Physical Oceanography* 53.6, pp. 1467–1484.

McWilliams, James C, William R Holland, and Julianna HS Chow (1978). “A description of numerical Antarctic Circumpolar Currents.” In: *Dynamics of Atmospheres and Oceans* 2.3, pp. 213–291.

Mohammadi-Aragh, Mahdi, Knut Klingbeil, Nils Brüggemann, Carsten Eden, and Hans Burchard (Oct. 2015). “The impact of advection schemes on restratifiction due to lateral shear and baroclinic instabilities.” In: *Ocean Modelling* 94, pp. 112–127. URL: `http://www.sciencedirect.com/science/article/pii/S1463500315001419`.

Murakami, Shigenori (2011). “Atmospheric local energetics and energy interactions between mean and eddy fields. Part I: Theory.” In: *Journal of the Atmospheric Sciences* 68.4, pp. 760–768.

Olbers, Dirk, Jürgen Willebrand, and Carsten Eden (2012). *Ocean dynamics.* Springer Science & Business Media.

Oort, A. (1964). “On estimates of the atmospheric energy cycle.” In: *Monthly Weather Review* 11, pp. 483–493.

Oort, Abraham H, Laurence A Anderson, and José P Peixoto (1994). “Estimates of the energy cycle of the oceans.” In: *Journal of Geophysical Research: Oceans* 99.C4, pp. 7665–7688.

Pacanowski, R. C. and S. G. H. Philander (1981). “Parameterization of vertical mixing in numerical models of tropical oceans.” In: *J. Phys. Oceanogr.* 11, pp. 1443–1451.

Peixóto, José P and Abraham H Oort (1984). “Physics of climate.” In: *Reviews of Modern Physics* 56.3, p. 365.

Read, Peter L, Fachreddin Tabataba-Vakili, Yixiong Wang, Pierre Augier, Erik Lindborg, Alexandru Valeanu, and Roland MB Young (2018). “Comparative terrestrial atmospheric circulation regimes in simplified global circulation models. Part II: Energy budgets and spectral transfers.” In: *Quarterly Journal of the Royal Meteorological Society* 144.717, pp. 2558–2576.

Rimac, Antonija, Jin Song von Storch, and Carsten Eden (2016). “The total energy flux leaving the ocean’s mixed layer.” In: *Journal of Physical Oceanography* 46, pp. 1885–1900.

Rimac, Antonija, Jin-Song von Storch, Carsten Eden, and Helmuth Haak (2013). “The influence of high-resolution wind stress field on the power input to near-inertial motions in the ocean.” In: *Geophysical Research Letters* 40.18, pp. 4882–4886.

Röske, Frank (2006). “A global heat and freshwater forcing dataset for ocean models.” In: *Ocean Modelling* 11.3-4, pp. 235–297.

Sandström, Johan Wilhelm (1908). *Dynamische versuche mit meerwasser.*

Ssebandeke, John, Jin-Song von Storch, and Nils Brüggemann (2023). “Sensitivity of the Lorenz energy cycle of the global ocean.” In: *Ocean Dynamics*, pp. 1–16.

Staniforth, Andrew and John Thuburn (2012). “Horizontal grids for global weather and climate prediction models: a review.” In: *Quarterly Journal of the Royal Meteorological Society* 138.662, pp. 1–26.

Trossman, David S, Brian K Arbic, David N Straub, James G Richman, Eric P Chassignet, Alan J Wallcraft, and Xiaobiao Xu (2017). “The role of rough topography in mediating impacts of bottom drag in eddying ocean circulation models.” In: *Journal of physical oceanography* 47.8, pp. 1941–1959.

Van Mieghem, Jacques (1973). “Atmospheric energetics.” In: *Atmospheric energetics.*

Wiin-Nielsen, Aksel C and Tsing-Chang Chen (1993). “Fundamentals of atmospheric energetics.” In: *(No Title)*.

Winters, K. B., P.N. Lombard, J.J. Riley, and E.A. D’Asaro (1995). “Available potential energy and mixing in densitystratified fluids.” In: *Journal of Fluid Mechanics* 289, pp. 115–228.

Witter, Donna L and Dudley B Chelton (1998). “Eddy–mean flow interaction in zonal oceanic jet flow along zonal ridge topography.” In: *Journal of physical oceanography* 28.10, pp. 2019–2039.

Wu, Yang, Zhaomin Wang, and Chengyan Liu (2017). “On the response of the Lorenz energy cycle for the Southern Ocean to intensified westerlies.” In: *Journal of Geophysical Research: Oceans* 122.3, pp. 2465–2493.

Yang, Zhibin, Xiaoming Zhai, David P Marshall, and Guihua Wang (2021). “An idealized model study of eddy energetics in the western boundary “Graveyard”.” In: *Journal of Physical Oceanography* 51.4, pp. 1265–1282.

Zängl, Günther, Daniel Reinert, Pilar Rípodas, and Michael Baldauf (2015). “The ICON (ICOsahedral Non-hydrostatic) modelling framework of DWD and MPI-M: Description of the non-hydrostatic dynamical core.” In: *Quarterly Journal of the Royal Meteorological Society* 141.687, pp. 563–579.

Zhai, Xiaoming, Helen L Johnson, and David P Marshall (2010). “Significant sink of ocean-eddy energy near western boundaries.” In: *Nature Geoscience* 3.9, pp. 608–612.

Zhai, Xiaoming, Helen L Johnson, David P Marshall, and Carl Wunsch (2012). “On the wind power input to the ocean general circulation.” In: *Journal of Physical Oceanography* 42.8, pp. 1357–1365.

Zuo, Hao, Magdalena Alonso Balmaseda, Steffen Tietsche, Kristian Mogensen, and Michael Mayer (2019). “The ECMWF operational ensemble reanalysis–analysis system for ocean and sea ice: a description of the system and assessment.” In: *Ocean science* 15.3, pp. 779–808.

EIDESSTATTLICHE VERSICHERUNG

Hiermit erkläre ich an Eides statt, dass ich die vorliegende Dissertationsschrift selbst verfasst und keine anderen als die angegebenen Quellen und Hilfsmittel benutzt habe.

I hereby declare upon oath that I have written the present dissertation independently and have not used further resources and aids than those stated.

Hamburg, 2024

John Bosco Ssebandeke

Hinweis / Reference

Die gesamten Veröffentlichungen in der Publikationsreihe des MPI-M
„Berichte zur Erdsystemforschung / Reports on Earth System Science“,
ISSN 1614-1199

sind über die Internetseiten des Max-Planck-Instituts für Meteorologie erhältlich:
https://mpimet.mpg.de/forschung/publikationen

All the publications in the series of the MPI -M
„Berichte zur Erdsystemforschung / Reports on Earth System Science“,
ISSN 1614-1199

are available on the website of the Max Planck Institute for Meteorology:
https://mpimet.mpg.de/en/research/publications